The Rechargeable Lithium/ Air Battery And The Application of Mesoporous Fe_2O_3 In Conventional Lithium Battery

Jianli Bao

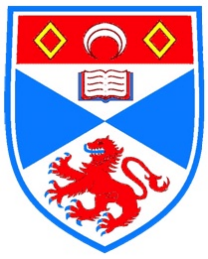

School of Chemistry

University of St. Andrews

Submitted in partial fulfilment of the requirements
for the degree of Doctor of Philosophy
in the field of Chemistry.

March 2009

Declaration

I, Jianli Bao, hereby certify that this thesis, which is approximately 30,000 words in length, has been written by me, that it is the record of work carried out by me and that it has not been submitted in any previous application for a higher degree.

I was admitted as a research student in April 2005 and as a candidate for the degree of Doctor of Philosophy in April 2006; the higher study for which this is a record was carried out in the University of St. Andrews between 2005 and 2009.

Date:

Signature of candidate:

Certification

I hereby certify that the candidate has fulfilled the conditions of the Resolution and Regulations appropriate for the degree of Doctor of Philosophy in the University of St Andrews and that the candidate is qualified to submit this thesis in application for that degree.

Date:

Signature of supervisor:

Library Declaration

In submitting this thesis to the University of St Andrews we understand that we are giving permission for it to be made available for use in accordance with the regulations of the University Library for the time being in force, subject to any copyright vested in the work not being affected thereby. We also understand that the title and the abstract will be published, and that a copy of the work may be made and supplied to any bona fide library or research worker, that my thesis will be electronically accessible for personal or research use unless exempt by award of an embargo as requested below, and that the library has the right to migrate my thesis into new electronic forms as required to ensure continued access to the thesis. We have obtained any third-party copyright permissions that may be required in order to allow such access and migration, or have requested the appropriate embargo below.

The following is an agreed request by candidate and supervisor regarding the electronic publication of this thesis:

Embargo on both all printed copy and electronic copy for the same fixed period of two years on the following ground: publication would be commercially damaging to the researcher, or to the supervisor, or the University; publication would preclude future publication.

Date:

Signature of candidate:

Signature of supervisor:

Dedicated to My Dearest Father

Acknowledgements

I would like to thank my supervisor, Prof. Peter Bruce, for his invaluable ideas and guidance throughout my Ph.D years, providing me with the opportunity to work in a research environment at the cutting edge of technology.

I would also like to express my appreciation to all the people who help me on many things: Dr. Aurélie Debart for discussing and advise on Li/ air project, Dr. Feng Jiao for discussing and advise on the synthesis of materials, Dr. Allan Paterson for discussing and advise on the electrochemisty, Mrs. Sylvia Williamson for measuring nitrogen adsorption and chemical analysis, and other people in the Bruce group in St. Andrews, both past and present, including Dr. Yuri Andreev , Dr. Rob Armstrong, Dr. Takeshi Ogasawara, Dr. Graham Armstrong, Dr. Zhangquan Peng, Dr. Stefan Freunberger, Dr. Laurence Hardwick, Dr. Chuhong Zhang, Mr. Yu Ren, Mr. David Ainsworth, Mr. Chris Lyness, Miss Valentina Gentili, Mr. Kris Maranski and Mr. Vincent Giordani. I am also grateful to the EaStCHEM for funding.

Also, I would like to thank my friends, Dr. Zhuojia Lin, Mrs. Yajuan Fu, Dr. Shanwen Tao and Dr. Yang Li who have made my time at St Andrews so enjoyable.

Finally, special thanks must also go to my parents, my brother, my sister-in-law and my niece, especially my husband, Meng Yu, for their understanding, support and love, without whom I could not have completed this thesis. I would like to dedicate this work to my be loved father, who just left us, may he rest in heaven.

Abstract

By replacing the intercalation electrode with a porous electrode and allowing lithium to react directly with O_2 from the air, the new rechargeable Li/O_2 battery system was studied. The porous cathode is comprised of carbon, catalyst and binder. The effect of every component was investigated.

The catalyst was believed to play an important role in the performance of the electrode. A number of potential materials have been examined as the catalyst for the O_2 electrode. It suggests that the nature of the catalyst is a key factor controlling the performance of the O_2 electrode. Several catalysts based on first row transition metal oxides each with three different morphologies, bulk, nanoparticulate and mesoporous were studied. The influence of the morphology on the discharge and charge voltage, discharge capacity and cyclability were examined. Among all the catalysts studied, α-MnO_2 nanowires was found to be the best candidate. The reversible capacities of 3000 $mAhg^{-1}$ (normalised by the mass of carbon) or 505 $mAhg^{-1}$ (based on the total mass of cathode + O_2) was obtained.

Some of other factors, such as type of carbon, type of binder, type of electrolyte, the construction of cathode and the modification of the catalyst were also investigated, even just in the early stage. Capacity fading during cycling is the main problem in all the cases. A number of experiments were carried out to understand and attempt to avoid the fading problem.

After successful synthesis of mesoporous α-Fe_2O_3 with unique properties (by Jiao et al.), the application of these materials in conventional Li battery was studied. Mesoporous α-Fe_2O_3 with ordered walls, mesoporous α-Fe_2O_3 with disordered walls and Fe_2O_3 nanoparticles were examined. It

was also applied to examine the different factors that influence the rate of conversion electrodes, i.e., Li^+ and e^- transport to and within the particles, as well as the rate of the two-phase reaction, demonstrating that for this conversion reaction electron transport to and within the particles is paramount.

Table of Contents

Chapter 1

Introduction

Harmful effects from the continued use of fossil fuels such as pollution and greenhouse gases associated with global warming become one of the most serious concerns in the history. Therefore, energy storage becomes one of the most important challenges in the new century. Wind, wave and solar power are important sources of renewable energy. Furthermore, electrochemical energy storage is more important due to their significant advantages, such as high energy density and long life. Fuel cells and energy storage supercapacitors have been studied and developed by many researchers. Different kinds of rechargeable batteries have been developed. Lead-acid, nickel-cadmium and nickel-metal hydride batteries have been used for many decades. Some kinds of advanced batteries, such as Na/S and ZEBRA battery, can be used at high temperature. Rechargeable lithium batteries have revolutionised portable electronics (mobile phones, laptops, digital cameras, etc). The high energy density which is mostly due to the high working voltage ($3.5 \sim 5$ V, $1.5 \sim 2$ V) and the design flexibility make Li batteries receive most attention at both fundamental and applied levels.

1.1 Energy Storage and General Batteries

1.1.1 Energy Storage

With the continuous increase of the world population, a sharp increase in energy consumption started after the Second World War. At the same time there was growing concern worldwide for the environment. It is now generally accepted that human activities, mainly burning of fossil fuels, are the main contributors to the global climate change.

Most of our available energy is obtained indirectly from chemical energy via mechanical energy and considerable amounts of work heat. Nowadays, transformation to electrical energy seems to be more useful, as many modern instruments depend on electricity as their energy source. In general, the electric power is generated by one of the following technologies/ energy sources.[1]: steam plants, gas turbines, combined cycle, nuclear reactors, hydrogenerators, wind power, solar energy and geothermal energy.

The problem is that energy demand is growing but conventional energy sources are limited and not located everywhere. Energy flow from a primary source is not constant, energy demand is not constant either. So there needs to be a mediator between the source of energy and its consumer. This mediator is energy storage which, in one way or another, plays a role in all natural and man-made processes. Energy storage is an essential part of any physical process and an essential enabling technology in the management of energy.

Electrochemical energy storage is the most traditional of all energy storage devices for power systems, it can be classified into three categories: primary batteries, secondary batteries and fuel cells. The common feature of these devices is primarily that stored chemical energy is converted to electrical energy. Primary and secondary batteries utilise the chemical components built into them, whereas fuel cells serve mainly as the reactor, in which the fuel and oxidant are supplied from outside and reaction products removed to the ambiance. Unlike secondary batteries, primary batteries

cannot be recharged when the built-in active chemicals have been used, and therefore cannot strictly be considered as genuine energy storage devices.

1.1.2 Basic Principles of Electrochemical Energy Storage and Conversion

Electrochemical cells convert chemical energy (the Gibbs free energy for the cell reaction) into electrical energy and vice versa. This conversion takes place at the interface between the active electrode mass and the electrolyte by means of an electrochemical redox reaction.[2]

Faraday's Law

The amount of electrical charge transferred in an electrochemical reaction: $Ox + ze^- \rightleftharpoons Red$ is given by Faraday's law:

$$Q = zF\frac{m}{M}$$

where m is the mass of the substance undergoing electrochemical reaction, M is the molar mass of the substance, F is the Faraday constant, 96487 coulombs per equivalent, or 26.8 Ah/ equiv., and z is the number of equivalents per mole of reactant (or electrons per molecule).

From the Faraday's law, the mass of a given substance required for the transfer of a given amount of charge is proportional to the equivalent mass. Apparently, it's desirable that the mass of reactants required be minimised by selecting electrode reactants of low equivalent mass.

Cell Potential

When two phases, e.g. an electrode and an electrolyte, are brought into contact, an electrochemical double layer across which a potential difference exists forms at the interface. The potential difference between two electrodes in the same electrolyte (each with its electrochemical double layer) may

be calculated from the thermodynamic and kinetic data for the electrode reactions. The equilibrium potential difference, ΔE, between two electrodes is given as follows:

$$\Delta E = -\Delta G/nF$$

where ΔG is the Gibbs free energy change for the overall cell reaction, and n is the number of equivalents involved in the reaction. Thus, the reversible potential for any cell can be calculated, providing that thermodynamic data for the cell reaction are available.

Specific Capacity

Electrode materials with high specific charge and high potential differences between the anode and cathode are needed for the batteries in order to achieve high specific energies ($Whkg^{-1}$) or high energy densities (WhL^{-1}).

Specific Energy

The weight of the battery is an important consideration in many applications. The usual objective is to minimise the weight and volume of the battery for a given amount of energy stored (W_e). The theoretical maximum specific energy W_e^{th} ($Whkg^{-1}$) can be calculated by follows:

$$W_e^{th} = \frac{\Delta G}{\sum_i n_i M_i}$$

where n_i is the number of moles of reactant i involved in the reaction, and M_i is the molar mass of reactant i. Usually, the practical specific energy of any battery is considerably lower than the theoretical value.

Energy Density

For certain applications of the batteries, e.g. implantable medical devices, the molar volume of the reactant is required to be as small as possible. Thus a high energy density will be obtained. To calculate the energy density, the

molar mass of the reactant (M_i) need to be replaced by the molar volume of the reactant (V_i) in the equation above.

Rate and Kinetics

The rate at which a cell can be discharged or charged is an important parameter and is governed primarily by the rate of transportation of the mobile ions during the reaction. Electroneutrality requires that the rate of diffusion of ions and charge compensating electrons be equal. It is thus the combined diffusion of mobile positive ions and electrons down a concentration gradient that is important.

1.1.3 Secondary Batteries

Rechargeable electrochemical batteries have a long history of application in electrical power systems. The battery market used to be dominated by the lead-acid battery invented by Plante in 1859. It is the oldest chemical storage device. The battery consists of alternate pairs of plates one lead and the other lead coated with lead dioxide, immersed in a dilute solution of sulphuric acid which serves as an electrolyte.[3–5] Because of the irreversible physical changes in the electrodes, failure occurs between several hundreds and 2000 cycles. The overall reaction is given as follows:

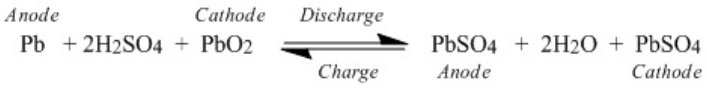

The main drawbacks of these batteries are comparatively low energy density, long charge time and the need for careful maintenance. By using carbon fibre in the positive electrode system, the weight was reduced, thus the power capability of lead-acid cells was increased. After the application of alloy negative electrodes, based on Pb/Ca, H_2 evolution and water loss reduces, thus the requirement for maintenance minimises. It has been the popular choice as a power source both for traction and stationary purposes.

Both Jungner and Edison contributed significantly to the development of the nickel-cadmium battery. The overall cell reaction is:

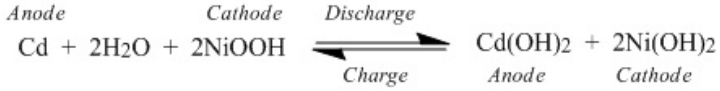

Standard Ni-Cd cells use an aqueous chemical impregnation process for the fabrication of electrodes. It has been used for storing electrical energy in spacecraft since the beginning of space exploration. A memory effect became one of the biggest drawbacks, though the mechanism is not fully understood yet. It also has a fairly high rate of self-discharge at high temperature. And cadmium is an awful poison that can contaminate the environment. The unpopularity of cadmium has encouraged the development of alternate nickel-based batteries, e.g. nickel-metal hydride batteries.

Nickel-metal hydride batteries using hydrogen storage alloys as the negative electrode material have been drawing increasing attention due to their higher specific energy and energy density, improved high rate capability, and high tolerance to overdischarge. The main difference between the Ni-MH batteries and the Ni-Cd batteries is that the active material in the negative plate is hydrogen absorbed in a metal alloy. The overall cell reaction is:

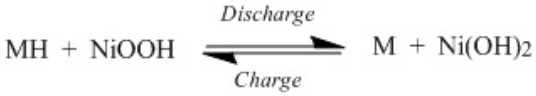

A very common problem with hydrogen storage materials is severe volume expansion during the charge-discharge process giving rise to cracking and pulverization of the alloy making it amenable to oxidation. The performance of the Ni-MH batteries has been improved since 1991 through a combination of approaches such as high density negative electrodes, thinner separators, upgraded positive electrodes and improved packaging efficiencies.

By utilizing the molten electrolyte system, extremely high energy density can be obtained by the high temperature batteries. The sodium-nickel chloride ($Na/NiCl_2$ (ZEBRA)) battery and the sodium-sulphur (Na-S)

Table 1.1: Status of several secondary batteries

System	Cell voltage, V	Theoretical specific energy, $Whkg^{-1}$	Specific energy, $Whkg^{-1}$	Specific power, Wkg^{-1}	Cycle life, NO. of cycles	Operation temperature, °C
Aqueous						
Lead-acid	2.1	175	20-85	50-400	> 700	ambient
Nickel-zinc	1.74	326	55-80	200-300	> 500	ambient
Nickel-iron	1.37	120	> 50	> 100	> 1000	ambient
Nickel-cadmium	1.2	200	$30 \sim 60$	600	> 1000	ambient
Nickel-metal hydride	1.2	200	$60 \sim 75$	160	$500 \sim 600$	ambient
High-temperature sodium-nickel chloride (ZEBRA)	2.58	787	90	$90 \sim 155$	600	300-400
sodium-sulphur	2.08	758	180	160	$50 \sim 200$	300-400
Non-aqueous Lithium-ion (e.g. $C/LiCoO_2$)	3.6	570	~ 150	> 200	~ 3000	ambient

battery are two of the most advanced high temperature battery concepts. They can meet the requirement of the commercial development, are the candidates for the zero emission vehicles. They both use a Na-conducting beta-alumina ceramic as the electrolyte which is able to conduct sodium ions with molten Na. Excellent performances were obtained over 3000 cycles for ZEBRA battery and over 1000-2000 cycles for Na-S battery. The operating temperature range is normally 300-400 °C . However, there are still some issues under development, such as the stability, cycle life and the safety concerns.

Table 1.1 lists the status of some important rechargeable batteries that are commercially available or in various states of development.[2–5] Rechargeable lithium batteries, of course, would attract special interests among the secondary batteries. New battery concepts, such as lithium-organic, lithium-air, magnesium-sulphur and proton batteries are under investigated and have a lot of potential to attract special interests in the future.[6]

1.2 Rechargeable Lithium Batteries

After the introduction of the earliest lithium batteries utilizing a lithium metal anode, Sony produced the first commercially successful rechargeable lithium ion battery in 1990 and is generally referred to as a rocking chair, swing or LION cell.[7] A lithium-ion battery consists of a lithium-ion intercalation negative electrode (generally graphite), and a lithium-ion intercalation positive electrode (generally the lithium metal oxide, e.g. $LiCoO_2$), these being separated by a lithium-ion conducting electrolyte, for example a solution of $LiPF_6$ in ethylene carbonate-diethylcarbonate.[8] The electric energy can be deposited and released through the cycles of intercalation and deintercalation of lithium-ion between the two electrodes. This kind of battery system has some distinct advantages compared with the conventional rechargeable batteries:

a. a high discharging potential (generally at about 3.6 V), which is three

times that of the Ni-Cd cells;

b. high specific energy (approximately 120-150 $Whkg^{-1}$) which is two to three times those of usual Ni-Cd batteries;[9]

c. long cycle life (can be more than 1000 cycles);

d. no-memory effect;

e. less pollution;

and so on. So this type of lithium-ion cell is found in most of today's high-performance portable electronic devices, such as mobile telephones, laptops, digital cameras. Nowadays, they are also used in spaceflight craft and communication equipment for the military purposes. Along with the development of their application, the battery industry increases rapidly. It is believed the application of the lithium battery will grow faster and wider in the future, for example in medical devices, hybrid electric vehicle (HEV) and electric vehicle (EV).

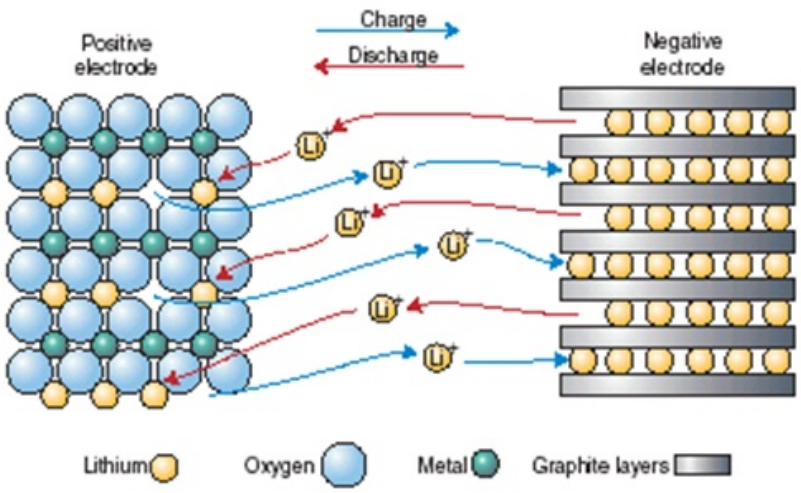

Figure 1.1: Schematic representation of a rechargeable lithium-ion battery.

A schematic representation of a rechargeable lithium-ion battery is shown in Figure 1.1. During charging process, lithium-ion moves into the electrolyte from the cathode, at the same time the lithium-ion in electrolyte moves

and intercalates into the anode. The reverse reaction happens during the discharging process. The reactions on both electrodes are:

$$\begin{aligned}
\text{Cathode}: \quad & LiMO_2 && \longrightarrow && Li_{1-x}MO_2 + xLi^+ + xe^- \\
\text{Anode}: \quad & nC_6 + xLi^+ + xe^- && \longrightarrow && Li_xC_6 \\
\text{Summary}: \quad & LiMO_2 + nC_6 && \Longleftrightarrow && Li_{1-x}MO_2 + Li_xC_6 \\
& (M = Co, Ni, Mn) &&&&
\end{aligned}$$

1.2.1 Cathode Material

For Li-ion batteries the cathode as-prepared material contains the Li^+ ions and these ions can be taken out and re accommodated again, these batteries are constructed in the discharge state. The cathode material should be able to accommodate large quantities of lithium per formula unit, sustain high rates of lithium intercalation and de-intercalation, have low Fermi level, low formula and molar weight, be stable in contact with the electrolyte, better be low in cost and be environmentally friendly.

A series of layered $LiMO_2$ (M for Ni or Co) electrode materials were proposed by Goodenough in the 1980s and $LiCoO_2$ is still the most widely used cathode material in commercial cells.[10] Figure 1.2 shows the structure of this material, the crystal structure consists of a lithium layer between two transition metal oxide layers, from which lithium can be removed and reinserted without destroying the structure. By oxidizing the cobalt from 3+ to 4+, a theoretical capacity of ~ 274 $mAhg^{-1}$ should be obtained, in fact, only half of the lithium can be removed and reinserted reversibly from this layered structure and thus only ~ 130 $mAhg^{-1}$ capacity was achieved in a real cell. Layered $LiCoO_2$ cycles with very good capacity retention (capacity fade at ~ 0.1 % per cycle).[10] However, other layered compounds with non-toxic and cheap elements are desirable to replace it. $LiNiO_2$ has the same structure as $LiCoO_2$ and is cheaper. The open voltage of $LiNiO_2$ cathode is slightly lower and the available capacity is ~ 140 $mAhg^{-1}$. Further removal of Li from the structure results in a reduction of the cycleability and causes exothermic decomposition at elevated temperatures.[11;12]

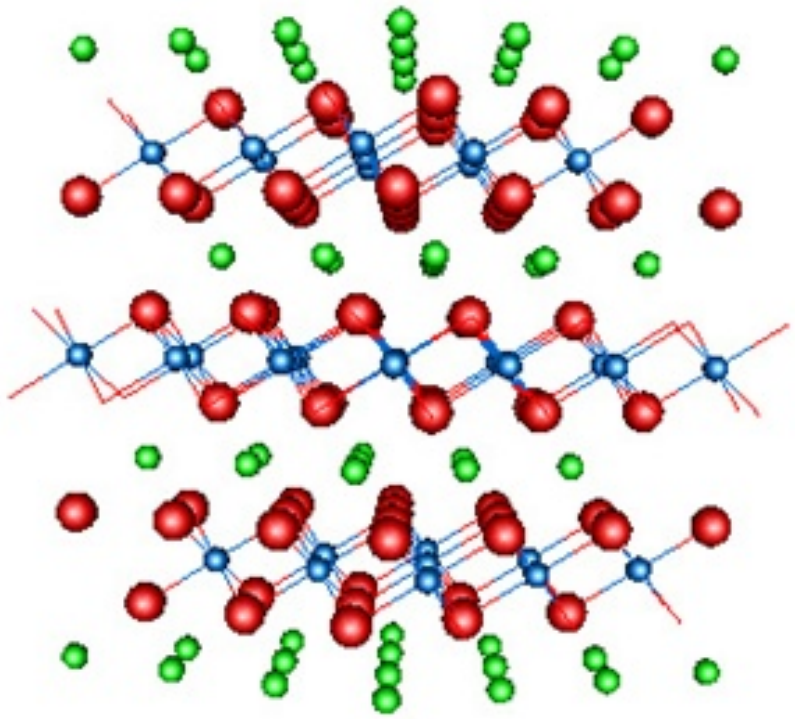

Figure 1.2: Crystal structure of layered $LiCoO_2$. Green, blue, and red balls represent lithium, cobalt, and oxygen atoms, respectively.

Manganese is approximately 1 % the cost of cobalt and significantly more environmentally benign than either cobalt or nickel. Bruce and co-workers first reported the layered $LiMnO_2$ synthesised through a Li^+ ion-exchange process with $NaMnO_2$.[13] Although the layered $LiMnO_2$ delivers a higher first charge capacity ($\sim$ 270 $mAhg^{-1}$) than that of $LiCoO_2$, it suffered a continuous structure change and converted to spinel. Although layered $LiMnO_2$ suffered a safety problem (O loss from layered material on heating), layered materials based on $LiMnO_2$, specially $Li(Ni_{0.5}Mn_{0.5})O_2$ and $Li(Ni_{1/3}Co_{1/3}Mn_{1/3})O_2$ are receiving a great amount of attention.[14;15] $Li(Ni_{0.5}Mn_{0.5})O_2$ has a high theoretical capacity ($\sim$ 280 $mAhg^{-1}$) but only delivers $\sim$ 180 $mAhg^{-1}$ on the first cycle. And the rate capacity is poor. The $Li(Ni_{1/3}Co_{1/3}Mn_{1/3})O_2$ phase contains cobalt which reduces the Ni/Li exchange and increases electronic conductivity. Recent results by Bruce's group showed that such a material may be synthesised which delivers above

200 $mAhg^{-1}$ at 1 C and 175 $mAhg^{-1}$ at 10 C.[16]

Besides the well-known layered structures, materials with the spinel structure have also been studied, e.g. low temperature $LiCoO_2$, $LiMn_2O_4$, and $LiFe_5O_8$.[17–19] $LiMn_2O_4$ is one of the most important spinel materials because manganese is cheap and low toxic. α-MnO_2 is formed after charging the material to remove one lithium from the structure, more than one lithium may be inserted in the structure when discharge the material to $\sim$ 3 V. Oxyanions based cathode materials were also introduced by Goodenough,[20] of which the most promising one is $LiFePO_4$. This material is safe, cheap and has a high voltage ($\sim$ 3.5 V) versus lithium. LISICON materials, such as Li_2FeSiO_4, are one of the new oxyanion materials, which can deliver $\sim$ 165 $mAhg^{-1}$ capacity on the first cycle. But like $LiFePO_4$, the electronic conductivity is low and hence rate performance is poor.[21]

1.2.2 Anode Material

Although lithium is the most electropositive (-3.04 V versus standard hydrogen electrode) and the lightest (equivalent weight M=6.94 $g{\cdot}mol^{-1}$, and specific gravity ρ=0.53 $g \cdot cm^{-3}$) metal, which leads to the high theoretical capacity (3860 $mAhg^{-1}$), due to the growth of dendritic lithium during each charge, which can lead to explosion hazards, it is not used.[9] The promising anode materials can be divided into these types: carbon anode materials, alloys materials, tin oxides, vanadium oxides, and the transition metal oxides.

Graphite is the most widely used anode material in commercial Li-ion batteries because it's low cost, non-toxic, good conductivity and a sufficiently low electrochemical potential to obtain a good cell potential ($\sim$ 3 V). It has a layered structure with hexagonal carbon sheets parallel each other in an ABAB... stacking along c-axis (Figure 1.3), which exhibits a reversible discharge capacity of $\sim$ 300 $mAhg^{-1}$ and a discharge plateau below 0.25 V.[22] However, other candidates were also investigated due to the limitation of low gravimetric capacity as low as 372 $mAhg^{-1}$ (based on LiC_6) and low volumetric capacity (1000 $mAh \cdot cc^{-1}$) of carbon. Li/Sn alloys have

very high theoretical capacity ($\sim$ 1000 $mAhg^{-1}$, based on lithiated phase $Li_{17}Sn_4$) and large theoretical volumetric capacity ($\sim$ 7000 $mAh \cdot cc^{-1}$).[23;24] Unfortunately, the accommodation of large amounts of lithium in the metal alloys or tin oxides is accompanied by volume changes in the host materials as well as phase transitions, which can lead to cracking and crumbling of the electrodes and a marked loss of capacity. People tried many new methods to limit the side effects on the electrode integrity. And the active/ inactive nanocomposite concept represents one attractive route.

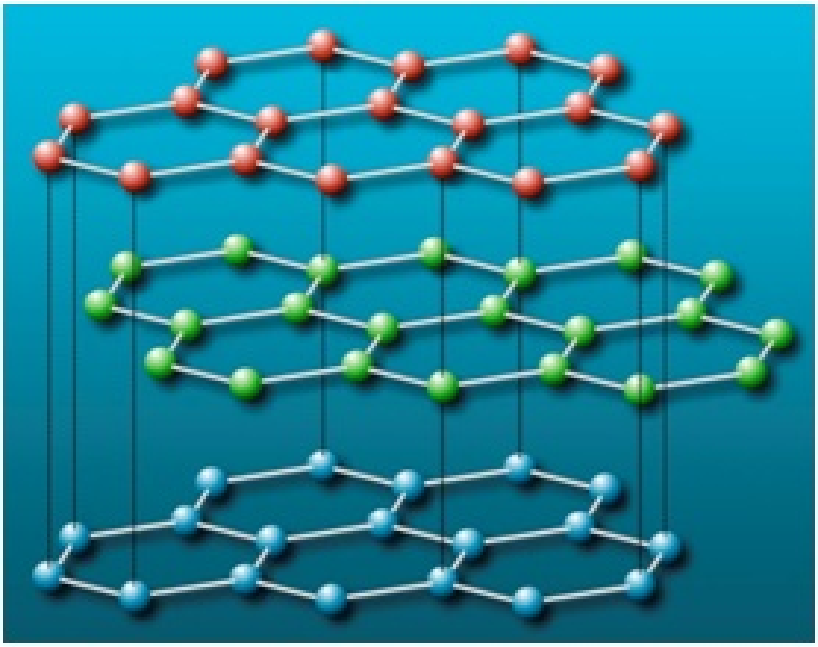

Figure 1.3: Schematic diagram of graphite structure.

Among all these materials, the nanostructured transition metal oxides have attracted considerable interest. Tarascon and his co-workers reinvestigated the reactivity of lithium with transition metal oxides and that the process could be reversible.[25] The electrochemical reaction of Li with CoO, CuO, NiO, Co_3O_4 and MnO was shown to lead to composite materials consisting of nanometer-scale metallic clusters dispersed in an amorphous Li_2O matrix. Among them, Co_3O_4 showed the highest discharge capacity ($\sim$ 800 $mAhg^{-1}$) and an excellent capacity retention (nearly no fading after 50 cycles). Due to the nanocomposite nature of these electrodes, the reactions,

termed 'conversion reactions' (see Figure 1.4), are reversible, providing large capacities that can be maintained for hundreds of cycles although there is irreversibility in the first cycle.[26–28]

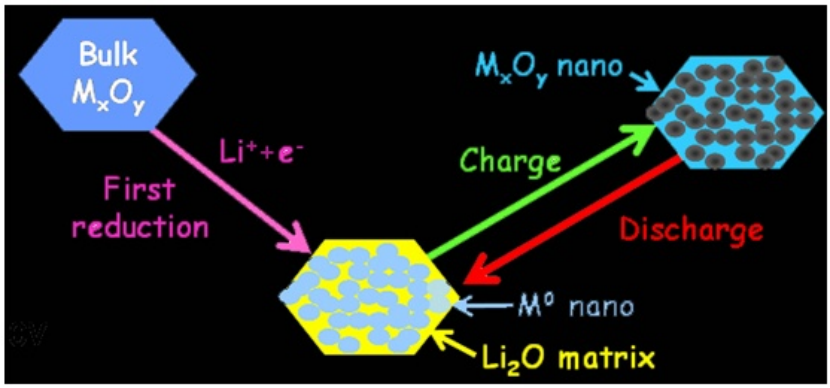

Figure 1.4: Schematic diagram of conversion reaction.

In the conventional Li-ion batteries, the electrode materials have quite low surface area and long path for ions and electrons to diffuse within the particles due to their large particle size. This limits their rate performance. Therefore, materials with high surface area and short lithium diffusion path are required for future applications, e.g. power tools and hybrid electric vehicles. Since 1991, after the discovery of the carbon nanotube, many inorganic nanomaterials have been studied. The cycling performance of the Li-ion batteries has been improved by applying the nanomaterials as the electrodes.[29;30]

1.2.3 Electrolyte

The main requirement for the electrolyte in the Li-ion batteries is to have a wide electrochemical stability window. The aqueous electrolytes were then ruled out. It is also required to have high mobility for lithium ions, good chemical and thermal stability, non-harmful environmental effect and no side-reactions with the electrodes.[31] The electrolyte in most common use is composed of lithium salts dissolved in an organic solvent. The electrolyte used in the Li-ion cells in this study is 1M $LiPF_6$ in 1:1 v/v ethylene

carbonate/ dimethyl carbonate (LP30 from Merck).

The soluble lithium salts act as charge carriers during the electrochemical process. Therefore good solubility and charge separation of the anion and cation are needed to obtain high conductivity. It could be achieved by choosing bulky anions with low negative charge density. The most commonly used salts are $LiClO_4$, $LiAsF_6$, $LiPF_6$, $LiBF_4$, $LiCF_3SO_3$ and $LiN(SO_2CF_3)$.

The organic solvents which have high working voltage, high lithium conductivity and a broad electrochemical stability window are mainly carbonates and esters. Carbonates are the most common choice because of their superior cycling behavior. Propylene carbonate (PC) has been used in Li-ion batteries for years and the problem it brought, e.g. co-intercalation of the solvent causing exfoliation of graphite electrodes, also has been studied. Ethylene carbonate (EC) is solid at room temperature, so it is mixed with other solvents albeit with ones with lower conductivity to produce a liquid working electrolyte. Typically, mixtures of EC with dimethyl carbonate (DMC) and diethyl carbonate (DEC) as well as PC are used.

1.3 Li/ Air Battery

A significant increase in the energy density of rechargeable lithium batteries is required to meet the future demands of consumer electronics, implantable medical devices and clean energy storage. The positive electrode represents a major obstacle to progress. $LiCoO_2$ is restricted to a reversible capacity of around 140 $mAhg^{-1}$, corresponding to approximately 0.5 Li/Co. Most of the research effort on cathode materials is devoted to the discovery and optimization of new lithium intercalation electrodes to replace $LiCoO_2$. However, such efforts are likely to lead only to a 2-fold increase in the energy density of the cathode, i.e. to 1 Li/Tm (transition metal). Therefore, it is essential to explore alternative strategies that can offer a route to a step change in charge storage significantly greater than can be delivered by intercalation electrodes.

Metal/ air batteries have been studied for more than a century.[4] The first Zn/ air battery was designed in 1878. This system has very high specific energy and high energy density, which is determined by the capacity of the anode and the storage technique for the reaction products. Other advantages include stable discharging potential, long storage life, environmentally friendly and low cost (depending on the metal in use) et al. O_2 from air, which is the cathodic reactant, does not have to be stored in special containers, thus significantly reducing the total mass of the battery and leading to the extremely high specific capacity. There are also some disadvantages lie in the system, e.g. sensitive to the environment, limited operating temperature range, limited specific power output, H_2 formation from the anode corrosion, and the carbonation of the alkaline electrolyte solution. A number of metals including Zn, Al, Fe, Mg and Ca have been studied as the anode in the metal/ air cells. Table 1.2 shows some of the properties of these metal/ air batteries. The systems under developing are utilizing the neutral or alkaline aqueous electrolyte solution. When discharge, the reaction in the system can be described as $4M + nO_2 + 2nH_2O \rightarrow 4M(OH)_n$, where M refers to the metal anode and n is determined by the valence change of the metal oxidation.

Zn/ air and Al/ air batteries are the most well known air batteries in aqueous electrolyte. Zinc is relatively stable in the alkaline aqueous solution, and it's the most reactive metal which can be electrodeposited from the aqueous electrolyte solution. It could provide the long life and high energy batteries for the portable devices, such as computer, communicating device and even the EVs. It has been developed to different types of portable or large scale batteries commercially and been applied in portable stereo, portable camera and marine navigation buoy etc. They can provide up to 400 $Whkg^{-1}$ specific energy and 1000 WhL^{-1} energy density in the primary batteries and up to 180 $Whkg^{-1}$specific energy and 160 WhL^{-1}energy density in the rechargeable Zn/ air batteries. But the problems remaining in the system such as dendrite formation, nonuniform Zn dissolution and deposition, limited solubility of the reaction products and the poor performance of the

Table 1.2: Characteristics of Metal/ Air Cells. [4]

Metal anode	Electrochemical equivalent of metal, Ahg^{-1}	Theoretical cell voltage,* V	Valence change	Theoretical specific energy (of metal), $kWh \cdot kg^{-1}$	Practical operating voltage, V
Li	3.86	3.4	1	13.0	2.4
Ca	1.34	3.4	2	4.6	2.0
Mg	2.20	3.1	2	6.8	1.2-1.4
Al	2.98	2.7	3	8.1	1.1-1.4
Zn	0.82	1.6	2	1.3	1.0-1.2
Fe	0.96	1.3	2	1.2	1.0

*Cell voltage with oxygen cathode.

air cathodes slows down the commercially developing of the rechargeable Zn/ air.

Aluminum is the third abundant element in the earth's crust, cheap and easy to handle. As an Al/ air battery anode, it has high theoretical capacity, high voltage and high specific energy. However it is not suitable for the rechargeable Al/ air batteries with an aqueous electrolyte because of the high charging potential at where the water is preferentially electrolysed. Therefore the effort has been directed to reserve and mechanically rechargeable (the Al anode was replaced after each discharge) designs.

Iron/ air batteries also has been studied and applied on motive power for many decades. It has good energy density,easily obtained materials and low self-discharge. On the other hand, the low efficiency, hydrogen evolution on charge, poor low-temperature performance and low cell voltage are the obstacles to the further development. Unlike zinc, the iron electrodes do not suffer a severe redistribution of active materials or gross shape change upon prolonged electrical cycling.

Ca/ air and Mg/ air batteries have been studied, but cost and problems like anode polarization or instability, parasitic corrosion, nonuniform dissolution, safety, and practical handling have so far inhibited the development of commercial products. However, the metal/ air batteries mentioned so far are aqueous systems, the O_2 reduction product is hydroxide, the theoretical and operating cell potentials are low (under 2 V), along with the moderate molecular masses of the anodic reactants, the specific energies ($Whkg^{-1}$) are generally low.

By replacing Zn or Al with Li, the high potential of the Li anode and the low molecular mass of Li offer significant advantages, see Figure 1.5. Researchers at Lockheed first introduced the concept of a Li/ air battery. They proposed the use of an aqueous alkaline solution for the electrolyte solution. But the concept was then abandoned in the 1980s because of the low efficiency relating to the reaction of Li with water and the major safety concerns relating to the excess H_2 formation. Abraham and Jiang

proposed to replace the aqueous electrolyte with a nonaqueous polymer electrolyte in 1996. A Li^+ conductive organic polymer electrolyte membrane was sandwiched by a thin Li metal foil anode and a thin carbon composite electrode on which oxygen is reduced during discharge. The overall cell reaction during discharge appears to be $2Li + O_2 \longrightarrow Li_2O_2$.[32;33] Read et al.[34–37], Dobley et al.[38] and Kuboki et al.[39] then further studied this by employing liquid aprotic organic solvents for the electrolyte solution.

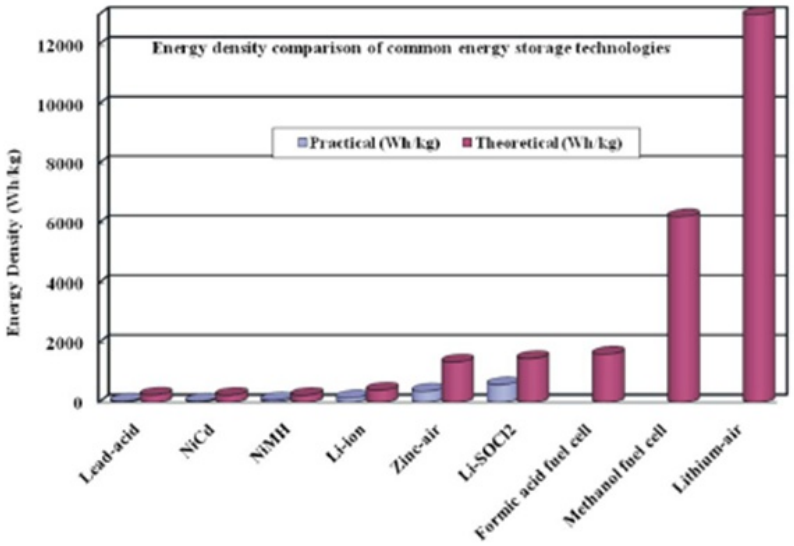

Figure 1.5: Energy density comparison of common energy storage/ conversion technologies.[40]

The Li/ air cells are basically composed of a metallic Li anode and an air (O_2) cathode. The cathode provides an interface where O_2 from air is dissolved in an electrolyte solution and catalytically reduced on the active components of the cathode,which is carbon with or without a catalyst to enhance the rate of O_2 reduction. Read and co-workers claim that the rate limitation for O_2 reduction is related to O_2 solubility and diffusion in the electrolyte solution.[35;41] They also claimed that by using an organic-based[34–39] or ionic liquid-based electrolyte solution[39], the overall (mixed) cell reactions in the Li/ air cell are:

$$2Li + \frac{1}{2}O_2 \longrightarrow Li_2O$$

$$2Li + O_2 \longrightarrow Li_2O_2$$

Read et al. compared the pore volume (mL) to mass (g) of Super P electrodes using PVdF binder (4.6 mLg^{-1}) to the one of the electrodes using Teflon binder (1.9 mLg^{-1}) and found out that the larger pore volume structure of the cathodes improves the discharge capacity by improving the transport of oxygen into the interior of the electrode.[42] They also determined Bunsen and Ostwald coefficients for oxygen in a number of pure and mixed organic solvents[35;41] and found a trend in increase of specific capacity as the solubility of oxygen increases and the viscosity decreases, thus concluded that oxygen diffusion through the electrolyte and electrolyte viscosity are key factors in determining cathode capacity. Both the products Li_2O and Li_2O_2 are not soluble in organic electrolyte solutions, they will fill in the pores of the porous cathode and block the further O_2 intake and thus abruptly ends cell life.

By using a new technology based on a water-stable, Li^+-conducting solid-state (LiGC) plate or "membrane", Read and co-workers succeeded in developing an aqueous-based Li/ air cell and avoiding the parasitic and dangerous reaction between metallic lithium and water. In the aqueous solution, the discharge products are generally highly soluble, so the aqueous-based systems represents an alternative approach for long operational life. The key of the new technology is the solid-state Li^+-conducting ceramic material which has conductivities of 10^{-4} to 10^{-3} S/cm at ambient temperatures, excellent chemical resistance towards organic and aqueous electrolyte solutions, and high mechanical stability.[42;43]

Dobley et al.[38] studied the cathode performance using a Mn-based catalyst. Manganese is a well known oxygen catalyst and may aid in breaking the O_2 bond. Dobley concluded that porosity and oxygen diffusion are key factors in determining cathode performance. Kuboli et al.[39] employed a hydrophobic ionic liquid and lithium salt in the cell to prevent parasitic corrosion of the lithium anode due to moisture contamination. Quite high specific capacities (2430 $mAhg^{-1}$ at 0.1 $mA \cdot (cm)^{-2}$) were achieved. Kuboli concluded that carbon mesopore volume is the key factor in determining

cathode capacity. So far, people have studied the primary discharge and agree that cathode performance is the limiting factor in a Li/ air cell.

Bruce and co-workers introduced the rechargeable Li/O_2 system, the reversible oxygen electrode is shown schematically in Figure 1.6. In this system, the positive intercalation electrode is replaced with a porous carbon electrode containing a catalyst[32;34;35;39;44]. On discharge, the Li^+ ions (electrolyte) and e^- (external circuit) combine with O_2 (air) to form Li_2O_2 within the pores of the porous carbon electrode.

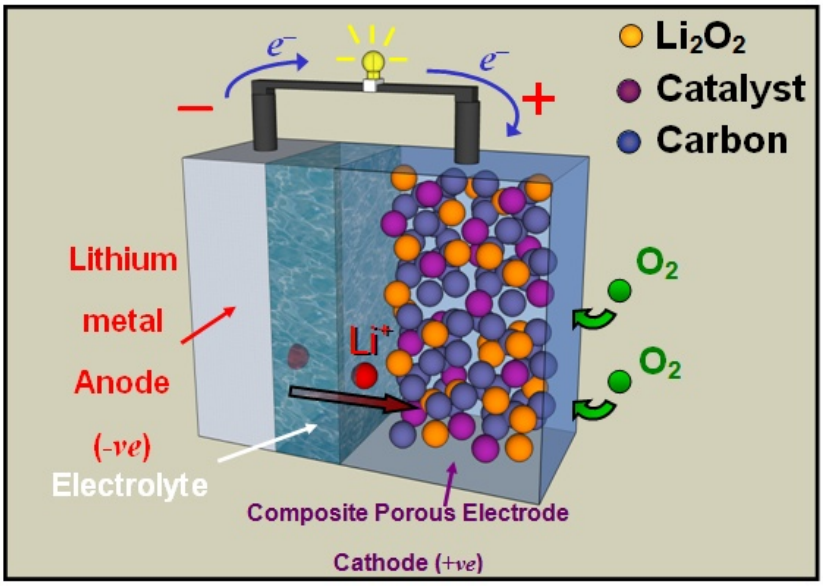

Figure 1.6: Schematic representation of a rechargeable Li/O_2 battery.

Using in situ mass spectrometry and other techniques, Bruce and co-workers have demonstrated that the reversible electrochemical reaction $2Li^+ + 2e^- + O_2 \leftrightarrow Li_2O_2$ happened in the nonaqueous lithium battery with an O_2 cathode.[44] In Figure 1.7 significant O_2 evolution was observed above 4.5 V from the cell with Li_2O_2 on charging, on contrast, the similar cell without Li_2O_2 gave no such oxygen evolution. It suggested that rechargeability of the Li/O_2 cell involves decomposition of Li_2O_2 back to Li and O_2 .[44] It not only demonstrated the reversibility of the formation of Li_2O_2 but also offered the possibility for the successful operation of a future rechargeable Li/O_2 battery. With the presence of electrolytic manganese dioxide (EMD) as the catalyst in

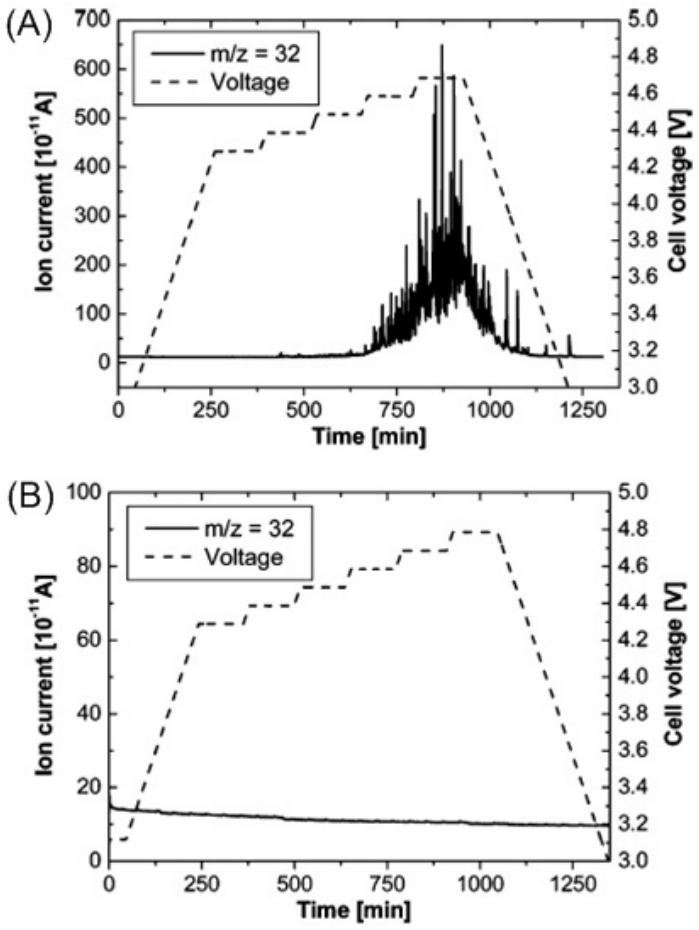

Figure 1.7: Variation of ion current corresponding to O_2 evolution as a function of time. The voltage was increased by 100 mV every 120 min. Electrode (A) with Li_2O_2 and (B) without Li_2O_2 .[44].

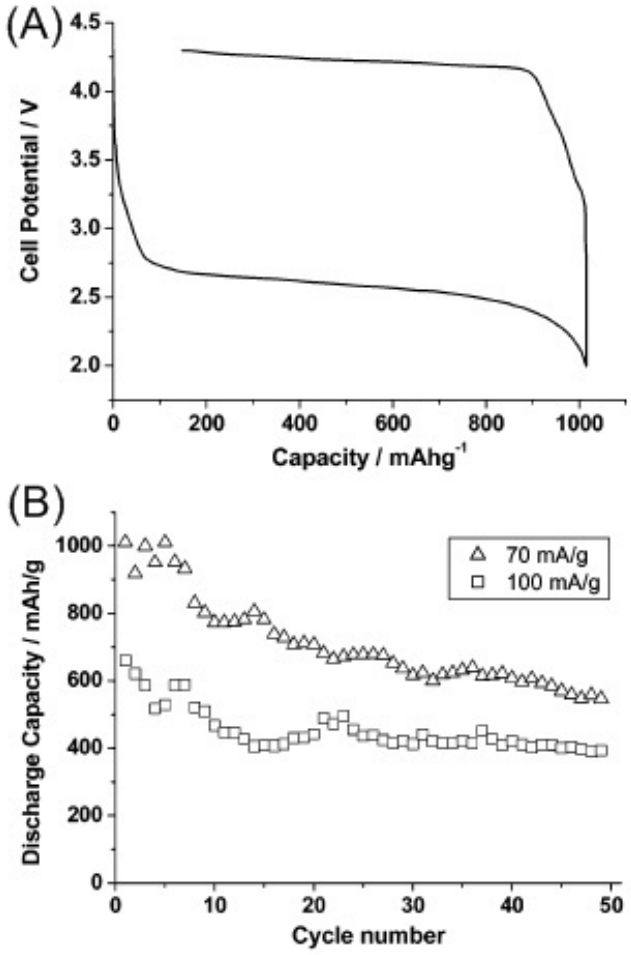

Figure 1.8: (A) Variation of potential on discharge then charge corresponding to the third cycle of the cell at a rate of 50 mAg^{-1}. Capacities are expressed per gram of carbon in the electrode. (B) Variation of discharge capacity with cycle number for an O_2 cathode.[44]

the O_2cathode, it was demonstrated, for the first time, that the cycling can be sustained for many cycles, see Figure 1.8.[32;34;35;44–46] Previous investigations have generally focused on its use as a primary battery. Bruce's work has demonstrated in the presence of a suitable catalyst the Li_2O_2 formed on discharge could be decomposed back to Li + O_2 on charging and that the cell could be cycled[44;47;48]. Evidently the catalyst plays an important role in the performance of the electrode.

As mentioned above, air breathing cathodes have been with us for a number of years in aqueous based batteries such as Zn/ air and Al/ air[4;49;50]. However in the Li/O_2 case here the electrolyte is non aqueous and the chemistry/ electrochemistry is quite different. As solid Li_2O_2 forms and fills the pores of the O_2 cathode, polarization increases, the cycling performance will definitely be affected when the pores are blocked by the solid Li_2O_2 . Besides, the charging potential is significantly higher than that on discharge. This also could potentially bring the problem such as the decomposition of electrolyte.

1.4 Aims

As mentioned above, materials on the nanoscale with large surface area could show better electrochemical properties in the rechargeable lithium batteries. Work on the reactivity of macroscopic versus nanoscale haematite (α-Fe_2O_3) particles with lithium further proved that.[8;26] Bruce's group reported the synthesis and properties of ordered and disordered mesoporous iron oxides prepared using a hard template.[51;52] These materials have even higher surface area than the nanoparticulate material does while the bulk particles are micrometer-sized. It would be interesting to study the electrochemical properties of these mesoporous materials in the rechargeable lithium batteries and compare the properties and structure changes to the ones of the nanoparticulate material.

By replacing the intercalation electrode with a porous electrode and

allowing lithium to react directly with O_2 from the air, higher capacities are possible approaching 1170 $\sim$ 1800 $mAhg^{-1}$, based on the formation of Li_2O_2 or Li_2O (practical capacities will of course be somewhat less due to the presence of carbon in the electrode). Earlier studies on the rechargeable Li/O_2 cell focused on electrolytic manganese dioxide (EMD) as catalyst in the oxygen electrode.[44] Although it provides higher capacities than intercalation electrodes, much fundamental work is required to understand and optimise the performance of the O_2 electrode for lithium batteries before it can be considered further for technological application. The nature of the catalyst plays a key role. It is important to identify good catalysts for the electrode reaction before focusing on other tasks, such as reducing the catalyst loading and optimizing porosity, binder, and electrolyte. However, there is much to be done to investigate the new system. Many factors could influence the performance, such as type of carbon, type of catalyst, morphology of the catalyst, type of electrolyte, O_2 solubility and diffusion in the electrolyte, and protection against air. Some of the factors will be discussed in this work.

References

[1] de Swaan Arons, J., van der Kooi, H., and Sankaranarayanan, K. *Efficiency and Sustainability in the Energy and Chemical Industries.* Marcel Dekker Ltd., (2004).

[2] Haas, O. and Cairns, E. J. *Annu. Rep. Prog. Chem. Sect. C* **95**, 163 (1999).

[3] Ter-Gazarian, A. *Energy Storage For Power Systems.* Peter Peregrinus Ltd., (1994).

[4] Linden, D. and Reddy, T. B. *Handbook of Batteries.* McGraw-Hill, New York, 3 edition, (2002).

[5] Bergveld, H. J., Kruijt, W. S., and Notten, P. H. L. *Battery Management Systems-Design by Modelling.* Kluwer Academic, (2002).

[6] Armand, M. and Tarascon, J. M. *Nature* **451**(7), 652 (2008).

[7] Nagaura, T. *International Battery Seminar* (3) Deerfield Florida (1990).

[8] Arico, A. S., Bruce, P., Scrosati, B., Tarascon, J. M., and Schalkwijk, W. V. *Nature Materials* **4**, 366 (2005).

[9] Tarascon, J. M. and Armand, M. *Nature* **414**, 359 (2001).

[10] Mizushima, K., Jones, P. C., Wiseman, P. J., and Goodenough, J. B. *Mater. Res. Bull.* **15**, 783 (1980).

[11] Dahn, J. R., von Sacken, U., Juzkow, M. W., and Al-Janaby, H. *J. Electrochem. Soc.* **8**, 2207 (1991).

[12] Rougier, A., Gravereau, P., and Delmas, C. *J. Electrochem. Soc.* **4**, 1168 (1996).

[13] Armstrong, A. R. and Bruce, P. G. *Nature* **381**, 499 (1996).

[14] Ohzuku, T. and Makimura, Y. *Chemistry Letters* , 744 (2001).

[15] Ohzuku, T. and Makimura, Y. *Chemistry Letters* , 642 (2001).

[16] Shaju, K. M. and Bruce, P. G. *J. Power Sources* **174**(2), 1201 (2007).

[17] Thackeray, M. M., David, W. I. F., and Goodenough, J. B. *Mater. Res. Bull.* **17**, 785 (1982).

[18] Thackeray, M. M., David, W. I. F., Bruce, P. G., and Goodenough, J. B. *Mater. Res. Bull.* **18**, 461 (1983).

[19] Thackeray, M. M., Johnson, P. J., Depicciotto, L. A., Bruce, P. G., and Goodenough, J. B. *Mater. Res. Bull.* **19**, 179 (1984).

[20] Padhi, A., Nanjundaswamy, K., and Goodenough, J. *J. Electrochem. Soc.* **144**(4), 1188 (1997).

[21] Nyten, A., Abouimrane, A., Gustafson, T., and Thomas, J. *Electrochem. Comm.* **7**, 156 (2005).

[22] Guerard, D. and Herold, A. *Carbon* **13**, 337 (1975).

[23] Weppner, W. and Huggins, R. A. *J. Electrochem. Soc.* **125**, 7 (1978).

[24] Wen, C. J. and Huggins, R. A. *J. Electrochem. Soc.* **128**, 1181 (1981).

[25] Poizot, P., Laruelle, S., Grugeon, S., Dupont, L., and Tarascon, J. M. *Nature* **407**, 496 (2000).

[26] Larcher, D., Masquelier, C., Bonnin, D., Chabre, Y., Masson, V., Leriche, J. B., and Tarascon, J. M. *J. Electrochem. Soc.* **150**, A133 (2003).

[27] Gireaud, L., Grugeon, S., Laruelle, S., Pilard, S., and Tarascon, J. M. *J. Electrochem. Soc.* **152**, A850 (2005).

[28] Arico, A. S., Bruce, P., Scrosati, B., Tarascon, J. M., and Schalkwijk, W. V. *Nat. Mater* **4**, 366 (2005).

[29] Bruce, P. G., Scrosati, B., and Tarascon, J. M. *Angew. Chem. Int. Ed.* **47**(16), 2930 (2008).

[30] Bruce, P. G. *Solid State Sciences* **7**(12), 1456 (2005).

[31] Vincent, C. and Scrosati, B. *Modern Batteries.* Elsevier Science & Technology, (1997).

[32] Abraham, K. M. and Jiang, Z. *J. Electrochem. Soc.* **143**, 1 (1996).

[33] Abraham, K. M. and Jiang, Z. *U.S. Patent 5* **510**(209) April 23 (1996).

[34] Read, J. *J. Electrochem. Soc.* **149**, A1190 (2002).

[35] Read, J., Mutolo, K., Ervin, M., Behl, W., Wolfenstein, J., Drieger, A., and Foster, D. *J. Electrochem. Soc.* **150**, A1351 (2003).

[36] Read, J. and Pitt, A. *Proc. 41st Power Sources Conference* , 64 June 14-17 (2004).

[37] Read, J. *Proc. 9th Electrochemical Power Sources R&D Symposium* , 64 June 27-30, Myrtle Beach, SC (2005).

[38] Dobley, A., DiCarlo, J., and Abraham, K. M. *Proc. 41st Power Sources Conference* , 61 June 14-17 (2004).

[39] Kuboki, T., Okuyama, T., Ohsaki, T., and Takami, N. *J. Power Source* **146**, 766 (2005).

[40] Beattie, S. D., Manolescu, D. M., and Blair, S. L. *J. Electrochem. Soc.* **156**(1), A44 (2009).

[41] Read, J. *J. Electrochem. Soc.* **153**, A96 (2006).

[42] Kowalczk, I., Read, J., and Salomon, M. *Pure Appl. Chem.* **79**(5), 851 (2007).

[43] Fu, J. *U.S. Patent 6* **485**(622) November 26 (2002).

[44] Ogasawara, T., Débart, A., Holzapfel, M., Novak, P., and Bruce, P. G. *J. Am. Chem. Soc.* **128**, 1390 (2006).

[45] Dobley, A., Rodriguez, R., and Abraham, K. M. *Presented at the 206th Meeting of the Electrochemical Society, Honolulu, HI* , Abstract 496 October 4-8 (2004).

[46] Dobley, A., Morein, C., and Abraham, K. M. *Presented at the 208th Meeting of the Electrochemical Society, Los Angeles, CA* , Abstract 823 October 17 (2005).

[47] Débart, A., Bao, J. L., Armstrong, G., and Bruce, P. G. *J. Power Sources* **174**, 1177 (2007).

[48] Débart, A., Paterson, A. J., Bao, J. L., and Bruce, P. G. *Angew. Chem. Int. Ed.* **47**, 4521 (2008).

[49] Forman, H. J. and Fridovic, I. *Science* **175**(4019), 339 (1972).

[50] Zaromb, S. *J. Electrochem. Soc.* **109**, 1125 (1962).

[51] Jiao, F. and Bruce, P. G. *Angew.Chem.Int.Ed.* **43**, 5958 (2004).

[52] Jiao, F., Harrison, A., Jumas, J. C., Chadwick, A. V., Kockelmann, W., and Bruce, P. G. *J.AM.CHEM.SOC.* **128**, 5468 (2006).

Chapter 2

Routine Experiments and Characterization Techniques

2.1 Routine Experimental Details

2.1.1 Synthesis of the Mesoporous Template (KIT-6)

The preparation of mesoporous silica KIT-6 has been reported by Ryoo and co-workers.[1] A typical synthesis procedure is as follows: 2 g of the block copolymer Poly(ethylene glycol)-poly(propylene glycol)-poly(ethylene glycol) P123 (average $M_n \sim 5800$, Aldrich) was mixed with 72.5 mL of water and 3.35 mL of concentrated HCl (37 wt %, Fisher) in a beaker. The mixture was stirred at 35 °C until a homogeneous solution was obtained. 2 g of n-butanol (99.4+ %, Aldrich) was added and this mixture was stirred for 1 h before 4.3 g of tetraethyl orthosilicate (TEOS, 98 %, Aldrich) was added. After stirring at 35 °C for 24 h, the mixture was transferred into autoclaves which were sealed and maintained at 100 °C for another 24 h. The resulting mixture was filtered and dried at 60 °C , followed by mixing with 200-300 mL of ethanol and 10-20 mL of concentrated HCl (37 wt %, Fisher) in an 800 mL beaker. After stirring at room temperature for 1-2 h, it was filtered and washed with water and ethanol several times. The final sample was dried at 60 °C and

calcined at 500 °C for 3 h under air to remove the polymer template.

2.1.2 Synthesis of Mesoporous CuO/ NiO/ Co_3O_4/ Fe_2O_3/ Mn_3O_4

The preparation method of mesoporous CuO was developed by Ren et al.[2]. A typical synthesis procedure is as follows: 2.0 g of $Cu(NO)_3 \cdot 3H_2O$ was dissolved in 2.0 g of distilled water. This solution was infiltrated into 1.0 g of KIT-6. After drying in an oven at 100 °C for 1 h, the copper precursor/ silica composite was treated with aqueous ammonia solution vapor at room temperature for 1 h and dried at 100 °C for 1 h. The process of infiltration/ neutralization/ drying was repeated twice more with aqueous solutions of 1.5 g (in the second infiltration) and 1.0 g copper nitrate (in the third infiltration) to prepare the copper precursor/ silica composite. The copper precursor/ silica nanocomposite was calcined at 300 °C for 6 h to obtain the CuO/ silica nanostructure. The silica template was then removed from the CuO/ silica composite by treating several times with hot 0.2 M NaOH aqueous solution and washed three times with distilled water and with absolute ethanol twice. Finally the mesoporous CuO was obtained by drying at 60 °C for 2 h.

The preparations of the other mesoporous metal oxides have been reported by Jiao et al.

A typical synthesis of mesoporous NiO is as follows[3]: 1 g of $Ni(NO_3)_2 \cdot 6H_2O$ (98 %, Aldrich) was dissolved in 20 mL of ethanol, followed by addition of 2 g of mesoporous silica KIT-6. After stirring at room temperature until all the solution had been absorbed, the sample was heated slowly to 300 °C and calcined at that temperature for 3 h. The infiltration procedure was repeated, followed by calcined at 500 °C for 3 h. The resulting sample was treated twice with a 2 M NaOH aqueous solution in water to remove the silica template, followed by washing with water several times, and then drying at 60 °C .

A typical synthesis of mesoporous Co_3O_4 is as follows[4]: 1 g of $Co(NO_3)_2 \cdot$

$6H_2O$ (98 %, Aldrich) was dissolved in 20 mL of ethanol, followed by addition of 2 g of KIT-6. After stirring at room temperature until all solution had been absorbed, the sample was heated slowly to 300 °C and calcined at that temperature for 3 h. The impregnation procedure was repeated, followed by calcined at 500 °C for 3 h. The resulting sample was twice treated with a 10 % HF solution in water to remove the silica template, followed by washing with water and ethanol several times, and then drying at 60 °C .

In a typical synthesis of mesoporous α-Fe_2O_3 ,[5;6] 1 g of $Fe(NO_3)_2 \cdot 9H_2O$ (98 % Aldrich) was dissolved in 20 ml of ethanol followed by addition of 1 g of mesoporous silica KIT-6 (3D pore structure). After stirring the mixture at room temperature until a nearly dry powder had been obtained, the sample was heated slowly to 300 °C and calcined at that temperature for 3h. The impregnation procedure was repeated, followed by calcination at 500 °C for 3h, resulting in mesoporous α-Fe_2O_3 with disordered walls. For the synthesis of mesoporous α-Fe_2O_3 with ordered walls, 1.5 g of $Fe(NO_3)_2 \cdot 9H_2O$ (98 % Aldrich) was used. After stirred at room temperature until a fine and completely dry powder was formed, the sample was heated slowly to 600 °C and kept at that temperature for 6h. The resulting samples were treated three times with hot 2 M NaOH, to remove the silica template, centrifuged, washed several times with water and ethanol then dried at 60 °C in air.

A typical synthesis of mesoporous Mn_2O_3 is as follows[7]: 30 g of $Mn(NO_3)_2 \cdot 6H_2O$ (98 %, Aldrich) was dissolved in $\sim$20 mL of water to form a saturated $Mn(NO_3)_2$ solution. 5 g of mesoporous KIT-6 were dispersed in 200 mL of dried n-hexane. After stirring at room temperature for 3 h, 5 mL of the saturated $Mn(NO_3)_2$ solution was added slowly with stirring. The mixture was stirred overnight, filtered and dried at room temperature until a completely dried powder was obtained. The sample was heated slowly to 600 °C , calcined at that temperature for 3 h and the resulting material treated twice with a hot aqueous solution of 2 M NaOH, to remove the silica template, followed by washing with water several times, and then drying at 60 °C .

A typical synthesis of mesoporous Mn_3O_4 is as follows[7]: mesoporous

Mn_2O_3 was heated slowly to 280 °C and kept at that temperature for 3h under a 5 % H_2 -95 % Ar atmosphere.

2.1.3 Synthesis of Nanoparticulate CuO/ Fe_2O_3/ Co_3O_4/ Mn_3O_4

A convenient method to synthesis CuO nanoparticles has been reported by Deng et al.[8]. A typical synthesis is as follows: 100 ml of copper acetate ($Cu(OAc)_2$, > 99.8 %, ANALAR) alcoholic solution (0.05 M) were placed into a Teflon liner stainless steel autoclave of 120 ml capacity. The autoclave was then located in an oven at temperature of 110 °C and kept at that temperature for 20 h. After the reaction, the autoclave was cooled to room temperature naturally. The product was recovered by centrifugation, then washed twice in distilled water and three times in ethanol, and then dried at 60 °C .

Nanoparticulate α-Fe_2O_3 ($\sim$ 25 nm) was synthesised using a procedure reported by Tarascon et al.[9;10] In a typical synthesis, 3.2 g of $Fe(NO_3)_2 \cdot 9H_2O$ (> 98 %, Aldrich) was progressively dissolved in a 300 ml aqueous solution of HNO_3 (2×10^{-3} M). The resulting solution was heated in a glass flask with magnetic stirring and refluxed at its boiling point for 24 h. After cooling to room temperature, the reddish-brown suspension was centrifuged and washed with distilled water several times, then dried overnight at 50 °C .

Nanoparticulate Co_3O_4 was synthesised using a procedure reported by Tarascon et al.[11]. In a typical synthesis, 11 g of NaOH (> 98 %, Fisher) was dissolved in 400 mL of deionised water in a three-necked flask and heated until boiling under reflux and constant stirring. 8.15 g of $Na_2S_2O_8$ (Fisons) was then dissolved into the solution when the boiling was reached. Then 25 mL of a 0.69 M $Co(NO_3)_2 \cdot 6H_2O$ solution (5 g, 17.2 mmol, 98 %, Sigma-Aldrich) was added dropwise to the previous one, and a black precipitate instantaneously formed. The resulting suspension was aged at 105 °C for 1h, cooled to room temperature, and left to settle overnight. The precipitate was separated by centrifugation at 3000 rpm for 5 min, washed three times with

a 2 M HCl ($\sim$36 %, Fisher) solution to remove byproducts, washed twice with water to eliminate residual chlorine and dried at 50 °C overnight. The as-prepared product was then heated under air (2 °C /min) at 300 °C and maintained at this temperature for 1 h.

Nanoparticulate $Mn_3O_4$was synthesised following a procedure reported by Tang et al.[12]. In a typical synthesis, hydrogen peroxide (2 mL, 30 %, Fisher) was added to an aqueous solution of manganese nitrate (12 mL, 0.3 molL^{-1}, $>$ 97 %, Sigma-Aldrich) whilst stirring to form a homogeneous solution, then ammonia (5 mL, 0.5 molL^{-1}) was added to the mixture dropwise. Upon the addition of ammonia, the precipitation of Mn^{2+} by ammonia to $Mn(OH)_2$ and the oxidization of $Mn(OH)_2$ by H_2O_2 were achieved immediately accompanied by the decomposition of H_2O_2. The resulting suspension was transferred into a 23 mL Teflon-lined autoclave. The autoclave was then located in an oven at temperature of 130 °C and kept at that temperature for 12 h. The resulting product was collected, washed several times with distilled water and absolute ethanol, centrifuged, and dried under vacuum at 70 °C for 3 h.

2.2 Characterization Techniques

2.2.1 Powder X-ray Diffraction Technique

This technique is used to identify phase, determine unit cell, size and shape as well as establish complete crystal structure. After Max von Laue first suggested that X-rays may be diffracted when passed through a crystal in 1912, W. L. Bragg noticed the similarity of diffraction to optical reflection and deduced an uncomplicated equation treating diffraction as "reflection" from planes in the crystal lattice (Figure 2.1). The *Bragg's law* relates the d-spacing between planes to the X-ray wavelength and diffraction angle. $2d\sin\theta = n\lambda$ (where d is the distance between adjacent planes of atoms, θ is the angle of incident X-ray beam, n is the order of the diffracted beam, λ is the wavelength of the X-ray beam). Following this law, if we know λ and we can measure θ, we can calculate the d-spacings.

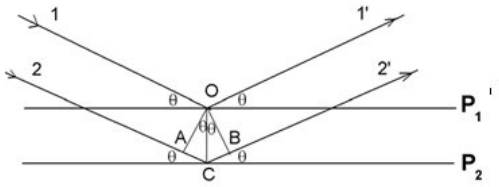

Figure 2.1: X-ray diffraction. P1 and P2 indicate lattice plane 1 and plane 2. O and C are the contact points between incident and reflected X-rays.

Powder X-ray diffraction (PXRD) has a wide range of applications in geology, material science, environmental science, chemistry, and the pharmaceutical industry. The sample studied is by definition a powder. It consists of many crystallites with different (random) orientations. The incident X-ray beam will be reflected by each set of planes at a characteristic 2θ where defined by Bragg's law. This goes to the typical powder diffraction pattern. The width of the peaks are related to the size and strain of the particle. By measuring the peak positions the size and shape of the unit cell can be determined and by analyzing the peak intensities the crystal structure (domain coordinate) may be discovered. This is achieved by Rietveld Refinement, in which a known structure is refined to display the best fit to the diffraction pattern.

X-rays may be generated by synchronic radiation or by bombarding a metal target e.g. Cu or Fe with electrons. The latter is used in the Stoe STADI/ P powder diffractometer employed in this work. The diffractometer operates in transmission mode and with a small angle position sensitive detector. For air-sensitive samples, the samples were sealed between two pieces of Mylar film by using vacuum grease or in quartz or glass capillary sealing by non corrosive silicone rubber. All assembling work was carried out in an Ar filled glove box for the air-sensitive samples.

2.2.2 Scanning Electron Microscopy Technique

Scanning electron microscopy (SEM) was pioneered by Manfred von Ardenne in 1937. The instrument was further developed by Charles Oatley and

first commercialised by Cambridge Instruments. The electron beam, which typically has an energy ranging from a few hundred eV to 100 keV, may be thermionically emitted from a tungsten or lanthanum hexaboride (LaB_6) and accelerated towards an anode or emitted via a field emission (FE). SEM can create various images by focusing a high energy beam of electrons onto the surface of a sample and detecting signals from the interaction of the incident electrons with the sample's surface. When the primary electron beam interacts with the sample, the electrons lose energy by repeated scattering and absorption within a teardrop-shaped volume of the specimen known as the interaction volume, which extends from less than 100 nm to around 5 μm into the surface. The energy exchanges between the electron beam and the sample results in the emission of electrons and electromagnetic radiation, the former can be detected to produce an image and the latter can provide elemental analysis. SEM studies the texture, topography and surface features of powders. An ultrathin coating of electrically-conducting material (usually gold or graphite) is needed for nonconductive samples to avoid the charging effects while no special preparation is needed for the conductive samples.

Figure 2.2: Photograph of a JEOL JSM-5600 scanning electron microscope.

For the work in this thesis, samples were examined using a JEOL JSM-5600 scanning electron microscope with a resolution of up to 3.5 nm (Figure 2.2).

2.2.3 Transmission Electron Microscopy Technique

The first practical transmission electron microscope was built at the University of Toronto in 1938. The short wavelength associated with an electron beam is the key to the ability of TEM to image with very high resolution. Electrons generated from a filament (usually tungsten) are accelerated and focused by electrostatic and electromagnetic lenses onto the sample. The beam interacts variously with the sample due to differences in density or chemistry. The beam that is transmitted through the sample contains information about these differences, and this information in the beam of electrons is used to form an image of the sample. Today electron energies are typically 200-400 KeV.

TEM is widely used in both material science/ metallurgy and biological sciences. The samples are of course non-volatile and have to be appropriately thin to be observed. High resolution TEM is commonly used in structural characterisation of nano-scale materials as it can provide structural information down to ~ 0.2 nm spatial resolution. In most inorganic crystalline materials, including ceramics, semiconductors and metals, the position of groups of atoms can be resolved. Possible applications include the investigation of defects, interfaces and grain boundaries. TEM can be used to simultaneously acquire high resolution images (where a digital CCD camera is often used for image capture) and selected area diffraction patterns from the same crystallite.

For the work in this thesis, studies were carried out by using a JEOL JEM-2011 (Figure 2.3). This TEM uses a LaB_6 filament as the electron source and the accelerating voltage is 200 keV. TEM and HRTEM images were both recorded by a Gatan CCD camera in a digital format. The selected area electron diffraction (SAED) patterns were recorded on traditional films followed by developing in a dark room and transforming into a digital form by scanning. The camera length for recording SAED patterns was set to 80 cm and the exposing time was varied depending on the brightness of the diffraction spots.

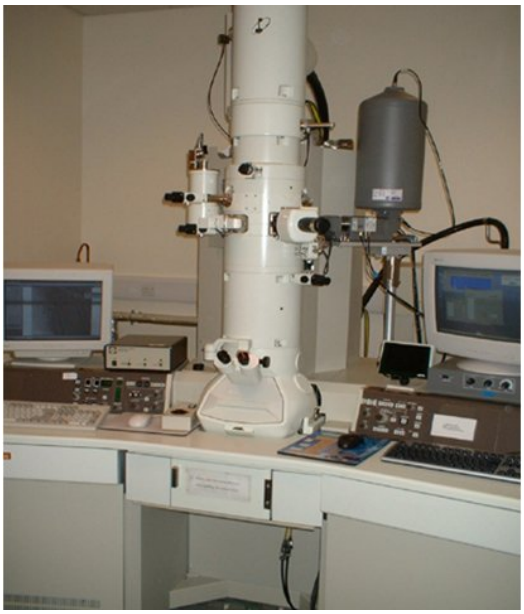

Figure 2.3: Photograph of a JEOL JEM 2011 transmission electron microscope.

2.2.4 N_2 Adsorption-desorption Technique

N_2 adsorption measurements can be used to determine the accessible surface area of materials that can take up the gas. The Langmuir and Brunauer, Emmett and Teller (BET) method has been widely used to analyse the data and estimate the surface area. The BET method was first introduced in 1938. This method extended the Langmuir theory from monolayer molecular adsorption to multilayer adsorption. The BET equation can be expressed by the following function:

$$\frac{1}{v[(P_0/P)-1]} = \frac{1}{v_m c}(\frac{P}{P_0}) + \frac{1}{v_m}$$

In the function, P is the equilibrium pressure of nitrogen, P_0 is the saturation pressure of nitrogen at the adsorption temperature, v is the quantity of adsorbed nitrogen in the solid, c is the BET constant and m is the quantity of adsorbed nitrogen via a monolayer mechanism. Because the linear relationship in this function only exists in the relative pressure (P/P_0) range from 0.05 to 0.35, the data for calculation of the surface area by the BET method were measured in this pressure range.

Measurement may be based on weight or volume. For the work in this thesis, Nitrogen adsorption-desorption measurements were carried out gravimetrically using a Hiden IGA porosimeter. The typical sample weight used in the measurement was 10-20 mg. The sample was normally outgassed at the rate of 20 mbar/ min to a high vacuum condition ($\sim 10^{-5}$ mbar) at a temperature of 120 °C for 2 h. Then the N_2 adsorption-desorption measurements were carried out under liquid nitrogen temperature.

2.2.5 Fourier Transform Infrared Spectroscopy

The infrared portion of the electromagnetic spectrum is divided into three regions: the near-, mid- and far- infrared. The mid-infrared, approximately 4000-400 cm^{-1} (30-1.4 μm) may be used to study the fundamental vibrations and associated rotational-vibrational structure. Infrared spectroscopy shows that molecules have specific frequencies at which they rotate or vibrate corresponding to discrete energy levels. In order for a vibrational mode in a molecule to be IR active, it must be associated with changes in the permanent dipole. The infrared spectrum of a sample is collected by passing a beam of infrared light through the sample. Examination of the transmitted light reveals how much energy was absorbed at each wavelength. Fourier Transform Infrared (FTIR) was used to determine the identity of unknown substances either organic or inorganic. It can be applied to the analysis of solids, liquids, and gasses. By matching the spectrum against reference materials or spectra, it can provide a proof of identity including the generic information about the types of functional group within a compound.

Studies were carried out on Perkin Elmer Spectrum GX FT-IR system at a resolution of 4 cm^{-1} and with a collection capacity of 8 scans. The instrument permits mid infrared measurements in the range 400–4000 cm^{-1}. A reference spectrum was recorded prior to each experiment to correct for background effects all the spectra recorded. Liquid samples were sandwiched between two plates of a high purity salt (potassium bromide), while the solid samples were ground with specially purified and finely divided potassium

bromide (to remove scattering effects from large crystals), then pressed in a die to form a translucent pellet through which the beam of the spectrometer can pass.

2.2.6 Nuclear Magnetic Resonance Spectroscopy Technique

Nuclear magnetic resonance was first described and measured in molecular beams by Isidor Rabi in 1938. Felix Bloch and Edward Mills Purcell refined the technique for use on liquids and solids in 1946. NMR studies magnetic nuclei by aligning them with an applied constant magnetic field and perturbing this alignment using an alternating magnetic field, those fields being orthogonal. The resulting response to the perturbing magnetic field is the phenomenon that is exploited in NMR spectroscopy and magnetic resonance imaging, which use very powerful applied magnetic fields in order to achieve high resolution spectra.

NMR spectroscopy is one of the principal techniques used to obtain physical, chemical, electronic and structural information about molecules due to the chemical shift and Zeeman effect on the resonant frequencies of the nuclei. It is a powerful technique that can provide detailed information on the topology, dynamics and three-dimensional structure of molecules in solution and the solid state.

For the work in this thesis, studies were carried out on Bruker Avance 300. Solid or liquid samples were dissolved in D_2O or chloroform in an NMR tube. The H-1, C-13, Li-7, P-31 and F-19 NMR have been used in this work.

2.2.7 TGA-MS

A powder sample is placed on a thermobalance and is subjected to heating by a pre-programmed temperature/ time profile or by a rate-controlled mode. Weight loss versus temperature is recorded and the gasses emitted

are delivered to and analysed by a mass spectrometer. The combination of thermogravimetric analysis (TGA) and mass spectrometry (MS) means that the weight losses can be associated with the evidence of particular spectra. Samples may be examined in different atmospheres.

For the work in this thesis, a Netzch STA 449C TGA-MS was employed and the measurements were made in an argon atmosphere. Because the system is sealed, specific heat capacity can also be measured versus temperature.

2.2.8 Electrochemistry

Electrochemical measurements are used extensively to investigate the properties of mesoporous metal oxides and the Li/O_2 cell.

Construction of the Porous Electrode

For the porous electrode in a Li/O_2 cell, a mixture of carbon, catalyst, Kynar2801, and propylene carbonate (PC) (weight ratios of $11:19:15:55$) was prepared as a slurry in acetone and spread onto glass using a Doctor Blade technique. After solvent evaporation at room temperature, the cast film was peeled off from the glass and cut into discs with the diameter of 13 mm.

Construction of the Composite Electrode

For the working composite electrode in coin cell, a mixture comprising 80 % active material, 10 % Super S carbon, and 10 % Kynar Flex 2801 (a copolymer based on polyvinylidene fluoride (PVDF)) was prepared as slurry in n-methylpyrrolidone (NMP) and spread onto aluminum (or copper) foil using a Doctor Blade technique. After solvent evaporation at 50 °C , the foil is cut into discs with the diameter of 13 mm and dried in a vacuum oven at 80 °C overnight.

Cell Construction

The electrochemical cells consist of the active cathode composite, the electrolyte soaked into a separator and a Li anode. These components are assembled in an argon filled glove box, with O_2 and H_2O levels < 0.1 ppm.

Coin type cells were used to study the electrochemical properties of mesoporous metal oxides. It is a convenient means of making many cells quickly and inexpensively. The coin cell kits were supplied by the National 46 Research Council, Canada (NRC) (25 mm in diameter by 2.5 mm in height) (Figure 2.4).

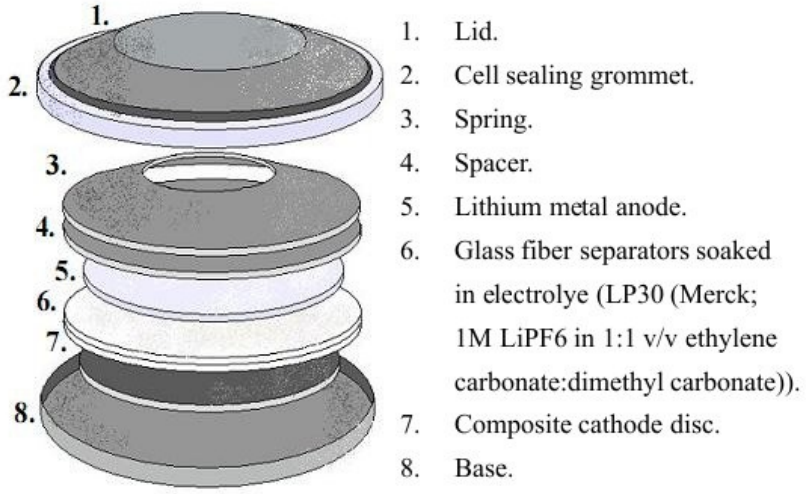

Figure 2.4: Exploded view of coin cell

Modified Swagelok cells were used for the Li/O_2 studies. Based on the construction of the normal Swagelok cell (Figure 2.5), a tube is used on the composite cathode side instead of the plunger so that the system can be exposed to O_2 atmosphere. The porous cathode is placed on an Al grid to allow exchange of O_2 from the surrounding atmosphere.

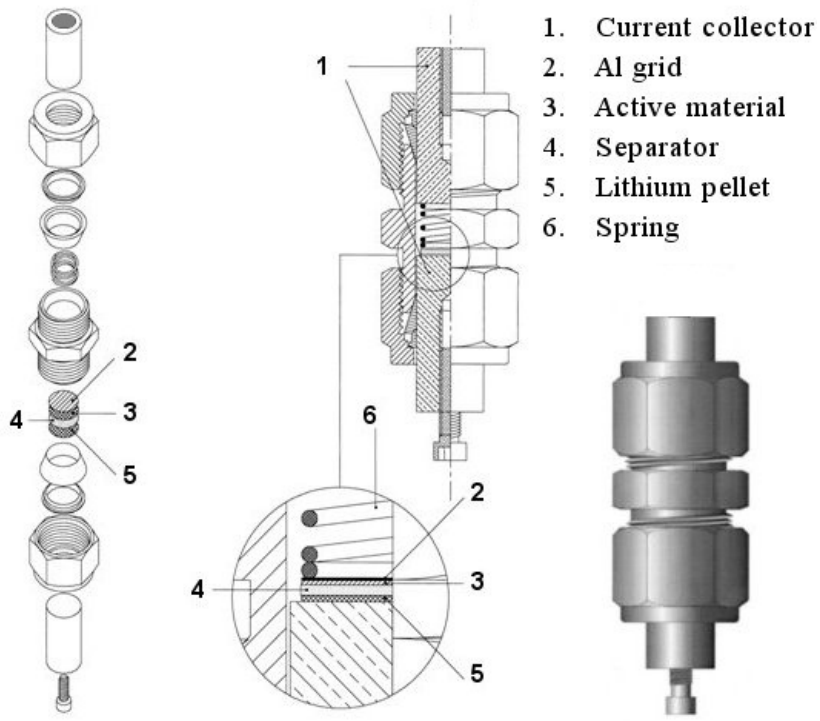

Figure 2.5: Diagram of Swagelok Cell.

Electrochemical Measurements

Galvanostatic cycling is the main electrochemical technique used during the course of this thesis. Experiments were performed on either a Macpile II Multichannel Cycler (Biologic, France) or a Maccor Series 4000 Battery Test System (Maccor Systems Inc., USA). During galvanostatic cycling a constant current (I) is applied to the cell and the potential is recorded as a function of time (t). The total amount of charge passed per unit mass of electrode material, i.e. the specific capacity C, during complete discharge (or charge) is given by: $C = I \cdot t/m$. In O_2 cells the convention is to normalise using the mass of carbon whereas with intercalation or conversion reactions the mass of the active phase is used. Neither is the total mass. This will be discussed in chapter 5. The data collected from galvanostatic measurements are often displayed as cell voltage (E) vs. specific capacity (C). The cyclability of the

material is presented as the total charge or discharge capacity as a function of cycle number. The cycling rate is given as C/N, where N is the time in hours for a full reaction of one mobile ion. (the so called C rate).

Potentiostatic cycling involves a constant potential being applied to the cell and the current being monitored. Cyclic voltammetry is a type of potentiodynamic electrochemical measurement. It can provide the initial characterization of a redox-active system. It also can provide the information about the rate of electron transfer between the electrode and the analyte, and the stability of the analyte in the electrolysed oxidation states. Experiments were performed on Macpile II Multichannel Cycler (Biologic, France).

A couple of useful electroanalytical approaches, known as potentiostatic and galvanostatic intermittent titration techniques (PITT and GITT, respectively) have been developed by Weppner and Huggins.[13;14] These techniques involve the displacement of the composition of an electrode system from equilibrium or steady state by the imposition of a step in either potential or current, and the measurements of the other (dependent) variable as a function of time. They can be used to characterise the diffusion kinetics of guest ions in ion-insertion electrodes. GITT combines transient and steady-state electrochemical measurements. It can be employed to determine a number of important kinetic and thermodynamic quantities in mixed conductors. PITT can avoid the side reactions such as the nucleation of new phases if the voltages are controlled within the stability range of the single phase. However, the ohmic voltage drop in the bulk electrolyte varying with time cannot be readily eliminated from the imposed voltage difference. For the work in this thesis, PITT and GITT were performed on Macpile II Multichannel Cycler (Biologic, France) to study the diffusion coefficients for Li ions insertion into the working cathodes.

All tests were carried out at 30 °C in an oven. For the characterization of electrode materials after cycling by other techniques, such as PXRD and TEM analysis, the working electrode was recovered from the cell followed by washing with dimethyl carbonate (DMC) several times and drying under vacuum without exposure to air.

References

[1] Kleitz, F., Choi, S. H., and Ryoo, R. *Chemical Communications* , 2136 (2003).

[2] Ren, Y. and Bruce, P. G. *in preparation* .

[3] Jiao, F., Hill, A. H., Harrison, A., Berko, A., Chadwick, A. V., and Bruce, P. G. *J.Am.Chem.Soc.* (2008).

[4] Shaju, K. M., Jiao, F., Débart, A., and Bruce, P. G. *Phys.Chem.Chem.Phys.* **9**, 1837 (2007).

[5] Jiao, F. and Bruce, P. G. *Angew.Chem.Int.Ed.* **43**, 5958 (2004).

[6] Jiao, F., Harrison, A., Jumas, J. C., Chadwick, A. V., Kockelmann, W., and Bruce, P. G. *J.AM.CHEM.SOC.* **128**, 5468 (2006).

[7] Jiao, F., Harrison, A., Hill, A. H., and Bruce, P. G. *Adv.Mater.* **19**, 4063 (2007).

[8] Hong, Z. S., Cao, Y., and Deng, J. F. *Materials Letters* **52**, 34 (2002).

[9] Larcher, D., Bonnin, D., Cortes, R., Rivals, I., Personnaz, L., and Tarascon, J. M. *J.Electrochem.Soc.* **150**, A1643 (2003).

[10] Larcher, D., Masquelier, C., Bonnin, D., Chabre, Y., Masson, V., Leriche, J. B., and Tarascon, J. M. *J.Electrochem.Soc.* **150**, A133 (2003).

[11] Binotto, G., Larcher, D., Prakash, A. S., Urbina, R. H., Hegde, M. S., and Tarascon, J. M. *Chem. Mater.* **19**, 3032 (2007).

[12] Wang, G. L., Tang, B., Zhuo, L. H., Ge, J. C., and Xue, M. *Eur. J. Inorg. Chem.* , 2313 (2006).

[13] Weppner, W. and Huggins, R. A. *J. Electrochem. Soc.: SOLID-STATE SCIENCE AND TECHNOLOGY* **124**(10), 1569 (1977).

[14] Wen, C. J., Boukamp, B. A., Huggins, R. A., and Weppner, W. *J. Electrochem. Soc.: SOLID-STATE SCIENCE AND TECHNOLOGY* **126**(12), 2258 (1979).

Chapter 3

Effects of Different Catalysts on the Electrochemical Performance of Rechargeable Li/O_2 Batteries

As discussed in Chapter 1, a new approach dispensing with the positive intercalation electrode and reacting lithium directly with O_2 from the air at a porous electrode has been established.[1] The use of an O_2 cathode can lead potentially to energy densities 5-10 times greater than at present. From previous work, it is known that catalysts can play an important role in facilitating the electrochemistry of O_2 in non-aqueous media, therefore it is interesting to explore the extent to which they can facilitate the oxygen electrode reaction in a lithium cell. A number of potential materials have been examined as the catalyst for the O_2electrode. Such investigations served to demonstrate that the nature of the catalyst is a key factor controlling the performance of the O_2 electrode.[2] It should be noted that the specific capacities are normalised with respect to the mass of carbon in the electrode, as is usual for porous electrodes, this point will be discussed in chapter 5.

3.1 Different Metal Oxides as Catalyst

3.1.1 EMD as the Catalyst

In the non-aqueous environment within the lithium cell, evidence to date indicates that the principal product of O_2 reduction is Li_2O_2 . The $2Li + O_2 \longleftrightarrow Li_2O_2$ reaction can take place even in the absence of a catalyst, as demonstrated in Figure 3.1, where a Li/O_2 cell in which the O_2 porous electrode consists of only carbon and Kynar as binder, has been discharged then charged. Discharging occurs at a potential of around 2.6 V with subsequent charging occurring at around 4.8 V, and then the subsequent decomposition of the electrolyte.

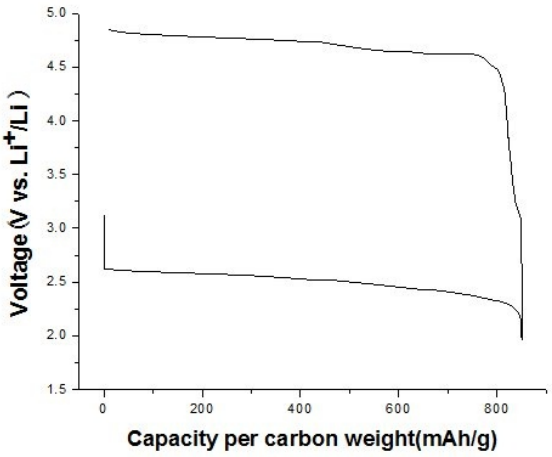

Figure 3.1: Variation of voltage on discharge then charge for the porous electrode, Super P : Kynar, mol ratio 97 : 3, at a rate of 70 mAg^{-1} .

Taking an identical cell and charging it, without prior discharge, under the same conditions gives rise to a higher voltage plateau, 5.1 V, corresponding to electrolyte oxidation and indicating that the 4.8 V plateau is associated with Li_2O_2 decomposition. This was confirmed by powder X-ray diffraction data collected as a cell constructed in the discharged state, i.e. containing Li_2O_2 , before and after charging, which clearly indicated the disappearance of Li_2O_2 on passing a sufficient charge to decompose all the lithium peroxide (Figure 3.2). Although it is possible to discharge then charge the Li/O_2 cell

in the absence of a catalyst, the use of a catalyst significantly facilitates the process, as demonstrated in Figure 3.3A where 19 wt % of electrolytic manganese dioxide (EMD), has been incorporated into the porous electrode. This has little effect on the discharge potential but shifts the charging potential to a significantly lower voltage, 4.3 compared with 4.8 V. The retention of capacity on cycling is also significantly better with a catalyst as demonstrated in Figure 3.3B, where the discharge capacity versus cycle number with and without the EMD catalyst were compared.

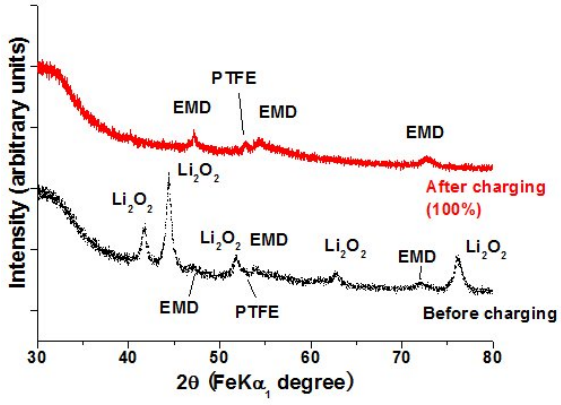

Figure 3.2: Powder X-ray diffraction data for a Li_2O_2 : Super P : EMD : PTFE electrode before charging and after passage of sufficient charge to decompose all the Li_2O_2 .

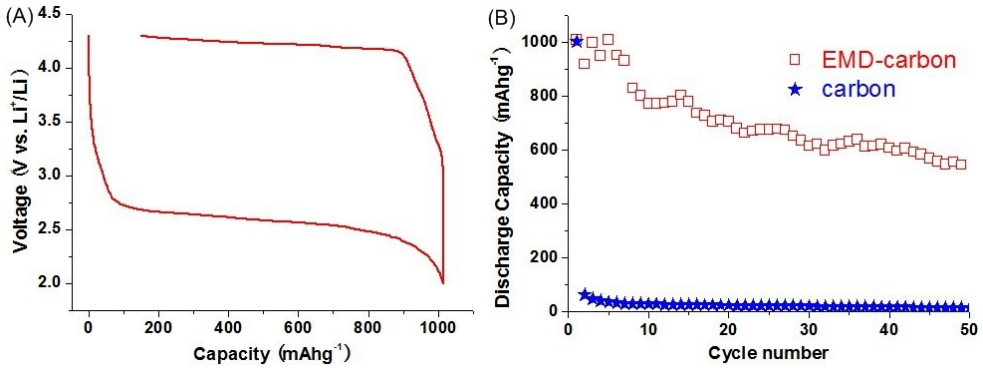

Figure 3.3: (A) Variation of voltage on discharge then charge corresponding to the 3rd cycle for the porous electrode, Super S : EMD : Kynar, at a rate of 70 mAg^{-1}. (B) Variation of discharge capacity with cycle number for an O_2 cathode with (red square) and without EMD (blue star) as catalyst at a rate of 70 $mAhg^{-1}$.

These results serve to illustrate the significant role of the catalyst on the

electrochemistry of the O_2 electrode in a Li/O_2 cell. Although in general, the catalyst in oxygen reduction is responsible for assisting the cleavage of the di-oxygen bond, the fact that EMD enhances the discharge and significantly the charge capacities and voltage of an electrode reaction involving the formation of Li_2O_2 (i.e. no di-oxygen bond cleavage) means that, at least for the non-aqueous case, the catalyst assists with the reduction of O_2 to ${O_2}^{2-}$ and its subsequent oxidation. It is anticipated that the oxygen on the surface of the oxide catalyst may participate in the electrode reaction. However, the mechanism is as yet unclear. Further work is underway to investigate the role of the catalyst in aiding the electrochemical reaction.

3.1.2 Other Transition Metal Oxide as the Catalyst

A number of other catalysts have been explored. Many materials have been investigated as electrocatalysts for O_2 electrochemistry in aqueous media over the last 200 years.[3–7] It is not expected to examine all of these. Instead, the best oxygen electrocatalyst for aqueous media, Pt, a fuel-cell cathode, $La_{0.8}Sr_{0.2}MnO_3$, the simple binary oxides of Fe, Co, Ni and Cu, as well as a ternary oxide combining two of the most promising binary oxides, i.e. $CoFe_2O_4$, have been explored. In all cases, the electrode construction was identical, including the ratios of carbon : catalyst : Kynar (weight ratios: 11 : 19 : 15).

The influence of different catalysts on the gross electrochemical performance of the porous O_2 electrode is shown in Table 3.1; where the discharge voltage and discharge capacities for cycles 1, 5 and 10 (capacities are expressed per gram of carbon in the electrode) are reported. It is clear that the discharge voltage is affected very little by changing the catalyst whereas the discharge capacity and its retention on cycling changes dramatically depending on the catalyst used.

Considering first platinum, it exhibits one of the lowest discharge capacities and this capacity drops rapidly on cycling. The variation of voltage on discharge and charge for the O_2 electrode with Pt is shown in Figure 3.4.

Table 3.1: Discharge voltage and discharge capacities of cycles 1,5, and 10

Catalyst	Discharge Voltage (V)	Capacity of Cycle 1 ($mAhg^{-1}$)	Capacity of Cycle 5 ($mAhg^{-1}$)	Capacity of Cycle 10 ($mAhg^{-1}$)	Capacity Retention per cycle (%)
Pt	2.55	470	60	60	1.28
$La_{0.8}Sr_{0.2}MnO_3$	2.6	750	75	40	0.53
Fe_2O_3	2.6	2700	500	75	0.28
Fe_2O_3 carbon loaded	2.6	2500	280	75	0.3
NiO	2.6	1600	900	600	3.75
Fe_3O_4	2.6	1200	1200	800	6.67
Co_3O_4	2.6	2000	1900	1300	6.5
CuO	2.6	900	900	600	6.67
$CoFe_2O_4$	2.6	1200	900	800	6.67

It is clear that the reduction of capacity occurs mainly on charging, i.e. the charge/ discharge efficiency is less than 100 %, this is true for all the catalysts used, although to different extents. Considering the performance of the fuel-cell cathode $La_{0.8}Sr_{0.2}MnO_3$, Table 3.1, although its first discharge capacity is higher than Pt, capacity fading is again significant. In summary, neither of the two classic oxygen electrodes exhibit good performance, with low discharge capacities on the first cycle and rapid capacity fading.

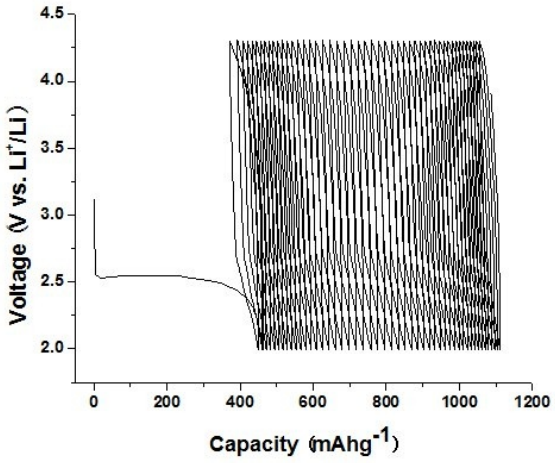

Figure 3.4: Variation of voltage on discharge then charge for the porous electrode, Super P : Pt : Kynar, at a rate of 70 mAg^{-1} .

Fe_2O_3 exhibits the highest first discharge capacity but this decreases rapidly on cycling, Table 3.1. The other well-known form of iron oxide is the inverse spinel Fe_3O_4 . Table 3.1 reports the basic electrochemical properties of the O_2 electrode containing this catalyst. Although the first discharge capacity of Fe_3O_4 is lower than that of Fe_2O_3 , the capacity retention on cycling is far superior for the spinel.

Given the good capacity retention of Fe_3O_4 , it presents the variation of voltage on discharge and charge for this catalyst in Figure 3.5. There is a clear step in the charge potential, which is not understood at this stage. The discharge and charge potentials move to values approximately 100-200 mV higher on cycling, the discharge voltages are again around 2.6 V with the charging voltages being around 4.25 V.

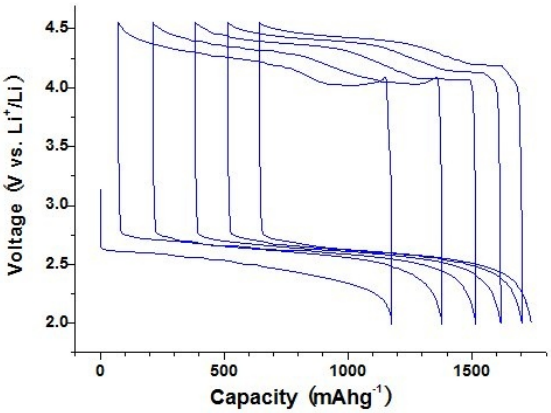

Figure 3.5: Variation of voltage on discharge then charge for the porous electrode, Super P : Fe_3O_4 : Kynar, as catalyst at a rate of 70 mAg^{-1} .

Considering catalysts based on other transition metal oxides, Co_3O_4 was examined. Table 3.1 indicates that this catalyst gives the best combination between a high first discharge capacity, around 2000 $mAhg^{-1}$ and capacity retention on cycling. Given the promising performance of the cobalt oxide material, its electrochemistry is presented in more detail in Figure 3.6. As observed for Fe_3O_4 , both the discharge and charge potentials increase by 100-200 mV on cycling. Whereas the average discharge potential is the same as other catalysts, the Co_3O_4 material gives the lowest charge potential with a value of around 4 V. The variation of charging potential with different

catalysts and with none, ranging from 4 V to 4.8 V contrasts with the invariance of the discharge voltage suggesting that the mechanism of the charging process depends on the nature of the catalyst.

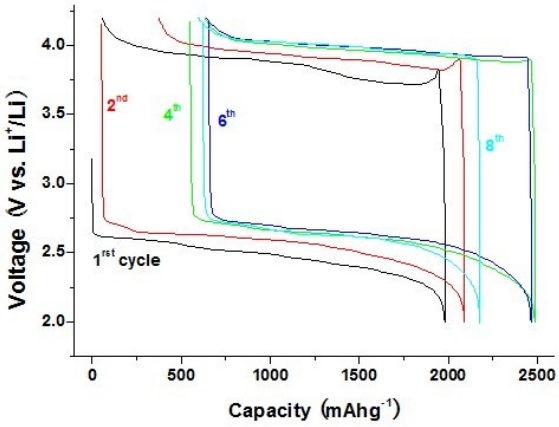

Figure 3.6: Variation of voltage on discharge then charge for the porous electrode, Super P : Co_3O_4 : Kynar, at a rate of 70 mAg^{-1} .

The performance of NiO is shown in Table 3.1. Although the initial discharge capacity is relatively high, 1600 $mAhg^{-1}$, this decreases substantially on cycling, indicating that this is not an attractive catalyst. In contrast, CuO, although it gives a lower initial capacity, shows good capacity retention on cycling. The variation of voltage on discharge and charge for CuO is shown in Figure 3.7A In this case, the charging voltage is around 4.3 V.

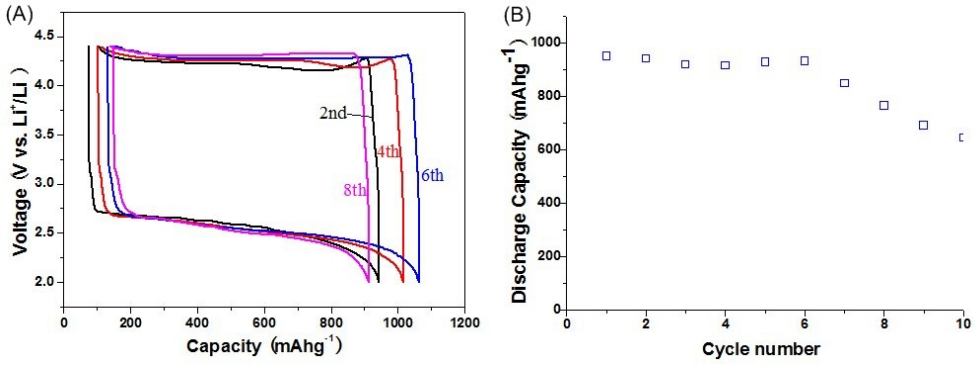

Figure 3.7: (A) Variation of voltage on discharge then charge for the porous electrode, Super P : CuO : Kynar, at a rate of 70 mAg^{-1} . (B) Variation of discharge capacity with cycle number for the same cell.

Many ternary transition metal oxides could be investigated. It has been chosen to examine one that combines the two transition metal ions from two of the most promising binary catalysts, namely Fe_3O_4 and Co_3O_4 , and with the same spinel structure, $CoFe_2O_4$. The performance is summarised in Table 3.1 and shown in more detail in Figure 3.8. This catalyst exhibits good capacity retention, with a capacity of 1200 $mAhg^{-1}$ on the first cycle dropping to only 800 $mAhg^{-1}$ after 10 cycles. The discharge and charge voltages are 2.6 and 4.3 V, respectively (Figure 3.8A).

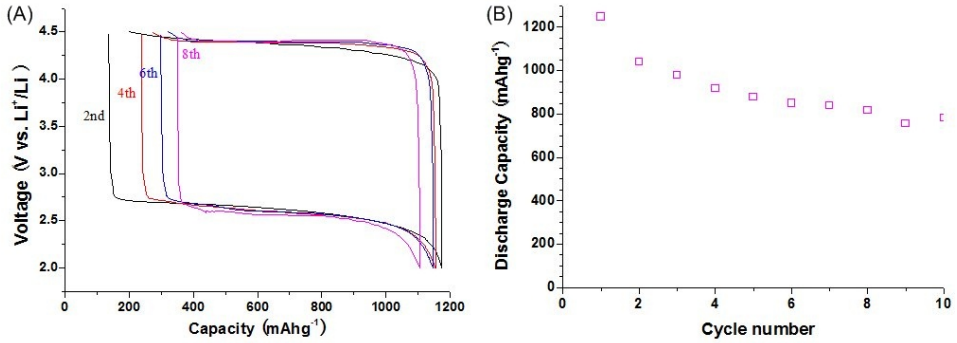

Figure 3.8: (A) Variation of voltage on discharge then charge for the porous electrode, Super P : $CoFe_2O_4$: Kynar, at a rate of 70 mAg^{-1} . (B) Variation of discharge capacity with cycle number for the same cell.

In summary, the screening process has indicated that two of the conventional oxygen electrocatalysts, platinum and the mixed metal perovskite $La_{0.8}Sr_{0.2}MnO_3$, do not perform well, something that is also true for Fe_2O_3 . Of the catalysts studied, Fe_3O_4 , CuO and $CoFe_2O_4$ give the best capacity retention. Co_3O_4 gives the best compromise between the discharge capacity and the retention on cycling.

3.1.3 Other Magnganese Oxides as the Catalyst

Earlier studies of the rechargeable Li/O_2 cell focused on EMD (electrolytic manganese dioxide) as the catalyst in the oxygen electrode.[1] MnO_x compounds were known to be good oxygen reduction catalysts.[8–10] It led us to the study of other manganese oxide compounds. Here the performances of

different manganese oxide compounds as the catalysts in an O_2 electrode, such as α-MnO_2 , β-MnO_2 , γ-MnO_2 , λ-MnO_2 , Mn_2O_3 and Mn_3O_4 are compared.[11]

Bulk $Mn_2O_3$and Mn_3O_4were obtained from Aldrich, and bulk β-MnO_2 from Strem. All other MnO_2 catalysts−bulk and nanowire α-MnO_2 , nanowire β-MnO_2 , bulk γ-MnO_2 , and bulk λ-MnO_2 −were prepared according to literature procedures.[12–16] Powder X-ray diffraction data were collected for all the catalysts (see Figure 3.9) confirming their identity.

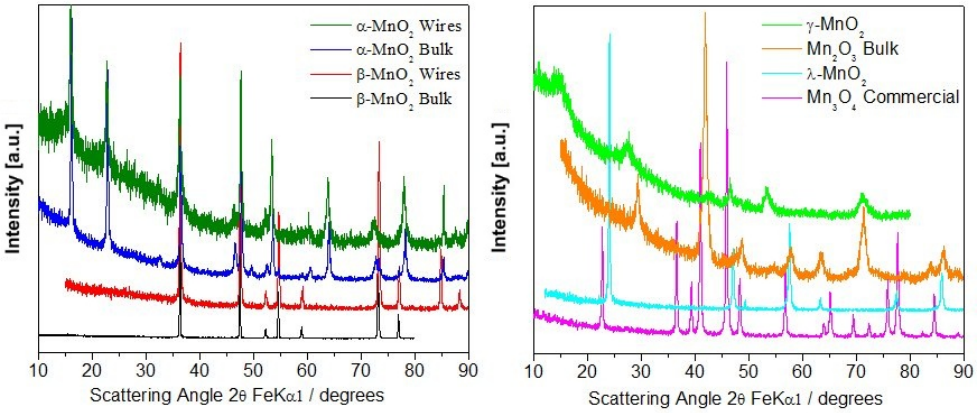

Figure 3.9: PXRD of manganese oxides catalysts; α-MnO_2 in bulk and nanowire form, β-MnO_2 in bulk and nanowire form, γ-MnO_2 , λ-MnO_2 , Mn_2O_3 and Mn_3O_4 .

The performances of the electrodes containing different manganese oxide catalysts are shown in Figure 3.10. The electrodes were constructed in an identical fashion to those containing EMD and with the same proportion of carbon, catalyst and binder. It is found that the other MnO_2 polymorphs, β, γ and λ, either exhibit lower capacities or capacities that fade very rapidly on cycling, their overall performance is markedly inferior to that of α-MnO_2 nanowires. The performances of Mn_2O_3 and the spinel Mn_3O_4 are also inferior to that of α-MnO_2 nanowires. This is also the case for non-manganese catalysts studied previously.[2]

Given the catalytic role of the manganese oxides, it is interesting to examine the effect of changing the surface area on the performance. An indication of this may be obtained by comparing the performance of α and

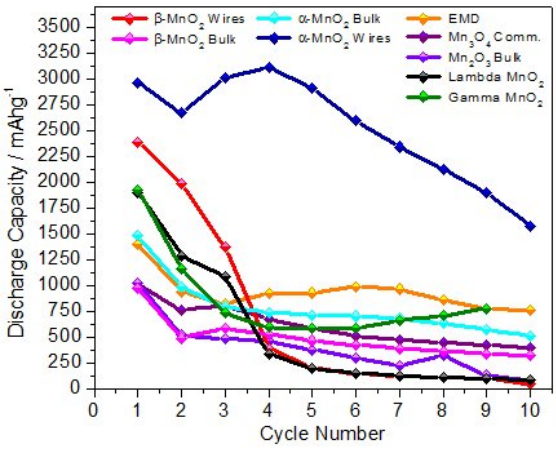

Figure 3.10: Variation of discharge capacity with cycle number for several porous electrodes containing manganese oxides as catalysts: α-MnO_2 in bulk and nanowire form, β-MnO_2 in bulk and nanowire form, γ-MnO_2 , λ-MnO_2 ,Mn_2O_3 , and Mn_3O_4 . EMD is included herein for comparison but was reported previously.[1] Cycling was carried out at a rate of 70 mAg^{-1} in 1 atm of O_2 . Capacities are per gram of carbon in the electrode. Lower cutoff potential 2 V.

β MnO_2 catalysts prepared in bulk and nanowire form, Figure 3.10. The morphologies are shown in Figure 3.11. The α-MnO_2 nanowires are typically 30-40 nm in diameter and can be up to several 100 nm long (BET surface area 22 m^2g^{-1}). The corresponding bulk material also has an elongated morphology, although the aspect ratio is not as high as the nanowires, for the bulk material typical dimensions are around 60-80 nm in diameter and 200-400 nm long (BET surface area 8 m^2g^{-1}). From Figure 3.10 it is evident that the nanowires exhibit a much higher capacity than the bulk material. This improvement is also observed when comparing nanowire (BET surface area 12 m^2g^{-1}) and bulk (BET surface area 1 m^2g^{-1}) β-MnO_2 . Here the elongated nature of the structure is not preserved in the bulk material, suggesting that the enhanced performance of the nanomaterials is due largely to surface area rather than the morphology per se. However, it is also important to note that the surface area of the α and β-MnO_2 nanowires differ by less than a factor of 2, yet the overall performance of the former on cycling is far superior to the latter, confirming that the nature of the catalyst is very important, not just the surface area.

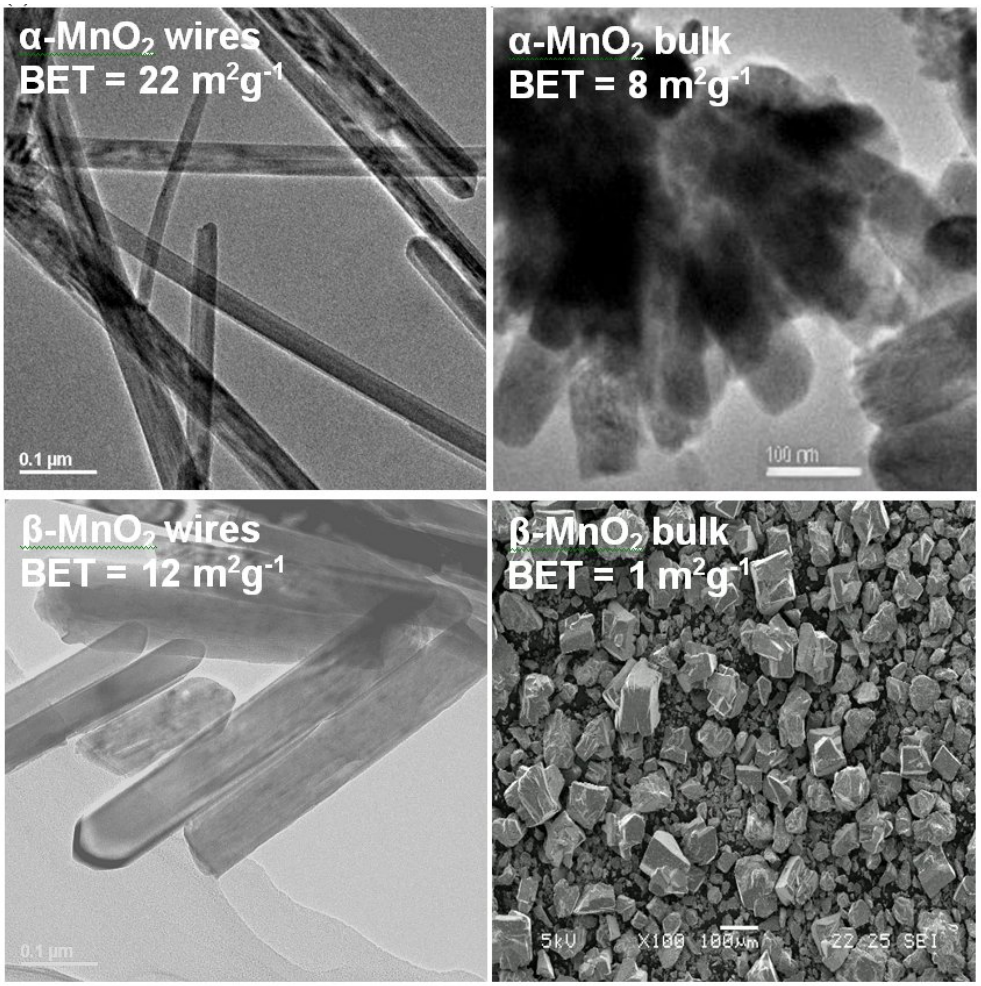

Figure 3.11: TEM/ SEM images of bulk and nanowire forms of α and β MnO_2 polymorphs showing their morphologies and surface areas.

3.2 α-MnO_2 Nanowires As the Catalyst

It turns out that α-MnO_2 nanowires is the most promising catalyst material among all the materials been studied.[11] The variation of capacity with cycle number for a porous electrode containing α-MnO_2 nanowires as the catalyst is presented in Figure 3.10, from which the superior behaviour of the α-MnO_2 catalyst is evident. The initial discharge capacity is 3000 $mAhg^{-1}$, it then drops slightly, rises again to 3100 $mAhg^{-1}$ on cycle 4 before declining steadily thereafter. This may be contrasted with previous reports for EMD,

the capacity of which falls below 1000 $mAhg^{-1}$ after 1st cycle, Figure 3.10 and Ref. [1]. The variation of potential with state of charge for several cycles of α-MnO_2 is shown in Figure 3.12. As observed previously for all other catalysts, the discharge voltage is around 2.6 V versus Li^+/Li[1,2]. Previous results have demonstrated that the charging potential varies according to the catalyst type.[2] Values ranging from 4 to 4.7 V versus Li^+/Li have been observed, with α-MnO_2 exhibiting a charging potential at the lower end of this spectrum, at around 4.0 V. This is another advantage of the α-MnO_2 nanowires since it is important to reduce the charging potential. It should also be noted that α-MnO_2 , and many of the other MnO_x compounds described here, support some Li intercalation. However, such intercalation could not explain the high capacities observed in Figure 3.10.

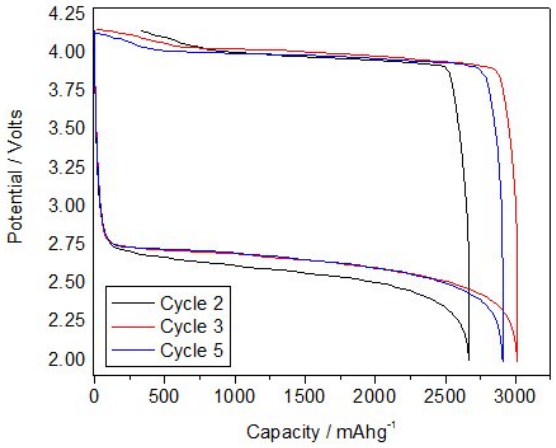

Figure 3.12: Variation of potential with state of charge for the porous electrode, containing, α-MnO_2 nanowires, reported in Figure 3.10. Cycled at a rate of 70 mAg^{-1} between 2 and 4.15 V.

The formation and decomposition of Li_2O_2 on discharge and charge were followed by examining the electrode using scanning electron microscopy, at different states of charge and discharge, Figure 3.13. In the as-prepared electrode, the nanowire morphology of the α-MnO_2 catalyst is clearly seen, as is the porosity of the electrode. Comparing the as-prepared electrode with those after partial and complete discharge, the increasing presence of white particles is associated with the formation of Li_2O_2 , as discharge proceeds.

Such particles are not observed in the as-prepared electrode. On charging, the white deposits decrease, then disappear entirely in the fully charged electrode. Careful examination of the micrographs suggest that Li_2O_2 , when present, is distributed throughout the electrode, with a significant proportion being associated directly with the α-MnO_2 nanowires, both at their tips and along their length. A cell containing α-MnO_2 nanowires as catalyst was dismantled at the end of discharge and the electrode subjected to investigation by Raman spectroscopy. The results, see Figure 3.14, confirmed that the dominant product of discharge was Li_2O_2 , as observed previously for EMD.[1]

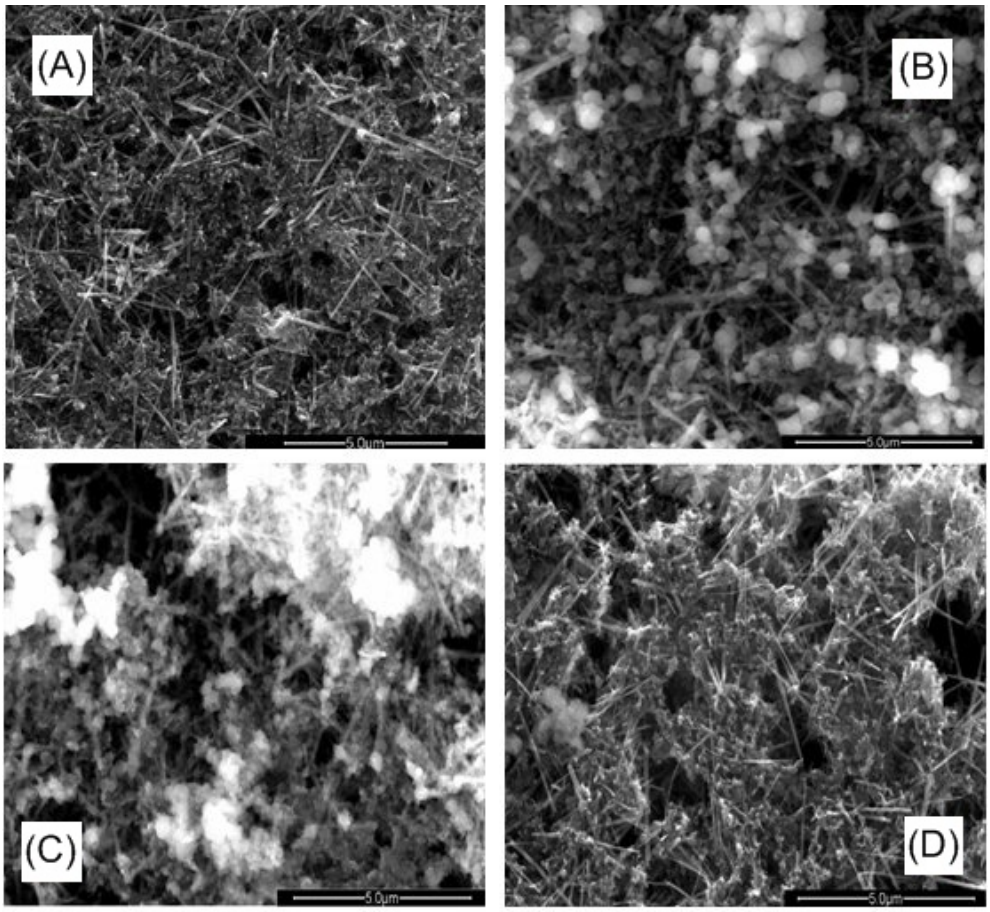

Figure 3.13: Scanning Electron Microscope images of the porous electrode containing α-MnO_2 nanowires as the catalyst at different states of charge and discharge. (A) as-prepared, (B) partially discharged (C) fully discharged and (D) fully re-charged electrode.

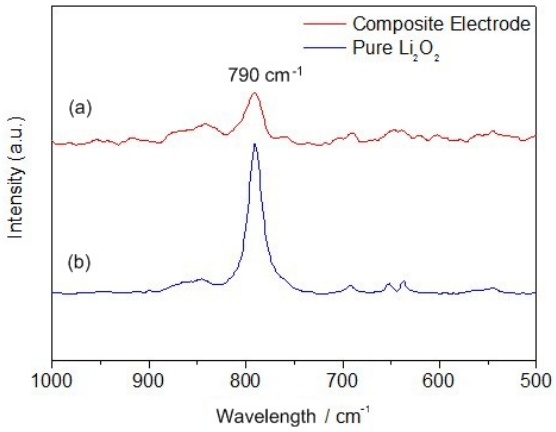

Figure 3.14: Raman spectra of (a) discharged composite electrode and (b) pure Li_2O_2 .

Although capacities in excess of 3000 $mAhg^{-1}$ can be obtained using α-MnO_2 nanowires as the catalyst, and not only on the first cycle, it is evident from Figure 3.10 that the capacities of this and all other catalysts fade. Indeed capacity fading has been a feature of all previous results on such O_2 electrodes.[1,2,17,18] This suggests that the origin of the capacity fading does not lie with the catalyst. Back to Figure 3.12, the polarization occurs at the end of discharge in all the cycles, this could be the block of the electrode. However, it is identified that if deep discharge is avoided, i.e. by limiting the discharge capacity to less than the maximum possible value (defined as where the voltage drops off significantly at the end of discharge, Figure 3.12), excellent capacity retention may be obtained. This is illustrated in Figure 3.15 where the capacity of an α-MnO_2 nanowire electrode has been limited by different degrees. Attempts to apply limits above 2400 $mAhg^{-1}$ resulted in capacity fade, in fact even at 2400 $mAhg^{-1}$ some evidence for this is noted at the end of cycling. The much improved capacity retention, when deep discharge is avoided, may reflect the fact that the formation of a large amount of Li_2O_2 in the pores results in them becoming blocked or causes expansion of the electrode resulting in a loss of contact between electrode particles during subsequent recharge. Such processes are not related to the nature of the catalyst per se and are therefore beyond the scope of the study in this chapter. However, work is ongoing to understand and hence minimise

the capacity fading (e.g. controlling the electrode porosity) without having to limit the depth of discharge.

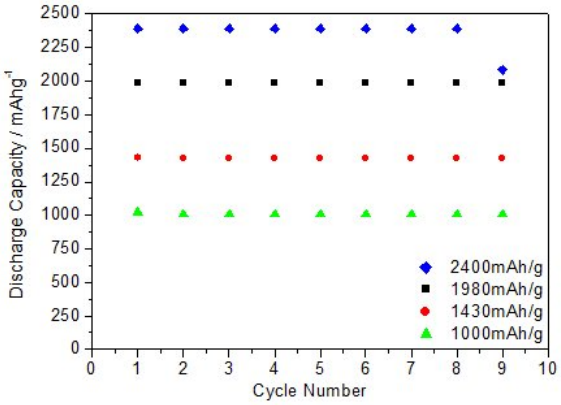

Figure 3.15: Variation of discharge capacity with cycle number for porous electrodes containing α-MnO_2 nanowires as catalyst when the state of discharge is limited to different degrees. Cycling rate of 70 mAg^{-1} . Capacities per gram of carbon in the electrode.

It is interesting to consider why α-MnO_2 performs better than other closely related manganese oxides. The crystal structure of the a polymorph is that of Hollandite and consists of 2×2 tunnels formed by edge and corner sharing MnO_6 octahedra, see Figure 3.16.[19] It is known that Li_2O can be incorporated within the tunnels, with the O^{2-} ions located at the tunnel centers and the Li^+ ions co-ordinated between these central O^{2-} ions and those forming the walls of the tunnels. The ability to accommodate both Li^+ and O^{2-} within the tunnels suggests the possibility of incorporating Li^+ and $O_2{}^{2-}$. Such incorporation is not possible in the other MnO_2 polymorphs or indeed the other MnO_x materials. Since the major role of the catalyst is to promote the reversibility of the Li_2O_2 formation, it is tempting to relate these two features and suggest that the ability of the crystal structure to incorporate Li^+ and O^{2-} , whether in the bulk or more likely near the surface of the material, is pertinent to the good performance of this catalyst. However, identifying Li_2O_2 in the near surface regions of α-MnO_2 will be a considerable challenge.

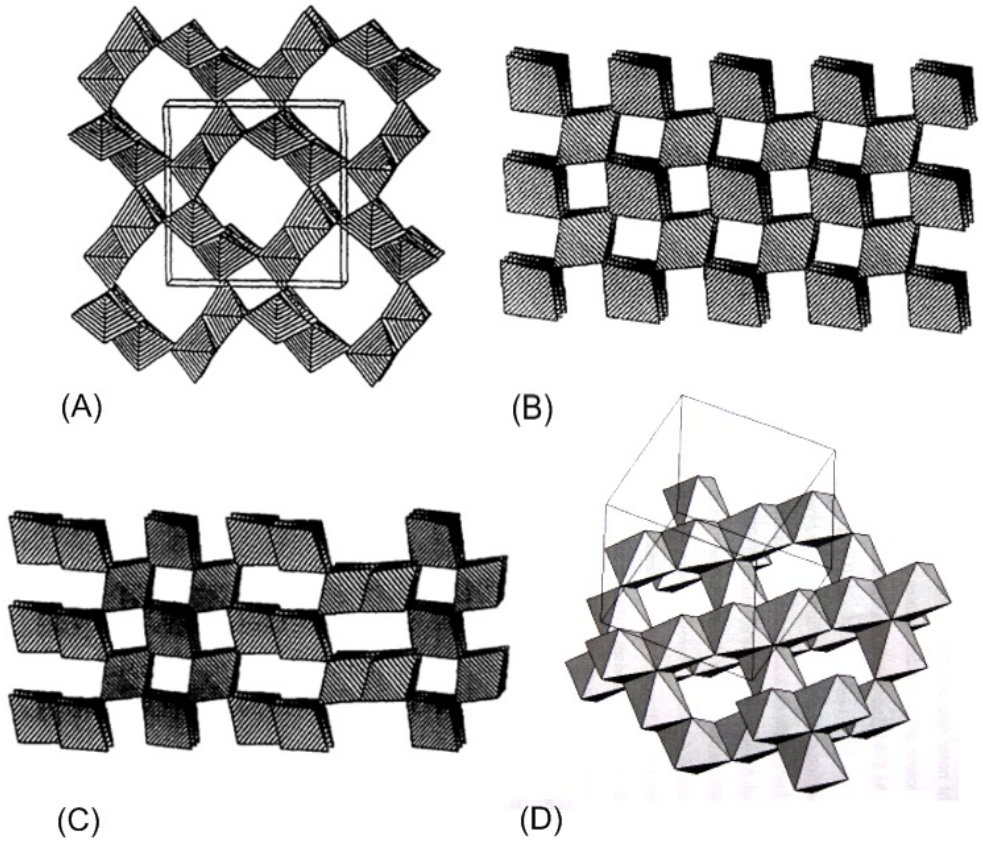

Figure 3.16: Crystal structure of MnO_2 with different polymorphs including: (A) α-MnO_2 , (B) β-MnO_2 , (C) γ-MnO_2 , (D) λ-MnO_2 .

References

[1] Ogasawara, T., Débart, A., Holzapfel, M., Novak, P., and Bruce, P. G. *J. Am. Chem. Soc.* **128**, 1390 (2006).

[2] Débart, A., Bao, J. L., Armstrong, G., and Bruce, P. G. *J. Power Sources* **174**, 1177 (2007).

[3] Mobius, H. *J. Solid State Electrochem* **1**, 2 (1997).

[4] Collman, J. P., Denisevich, P., Konai, Y., Marrocco, M., Koval, C., and Anson, F. *J. Am. Chem. Soc.* **102**, 6027 (1980).

[5] Zen, J.-M., Manoharan, R., and Goodenough, J. *J. Appl. Electrochem.* **22**, 140 (1992).

[6] Gonzalez-Cruz, R. and Solorza-Feria, O. *J. Solid State Electrochem.* **7**, 289 (2003).

[7] Fernandez, J. L., Walsh, D. A., and Bard, A. J. *J. Am. Chem. Soc.* **127**, 357 (2005).

[8] Yang, J. S. and Xu, J. J. *Electrochem. Comm.* **5**(4), 306 (2003).

[9] EI-Deab, M. S. and Ohsaka, T. *Electrochim. Acta* **52**(5), 2166 (2007).

[10] Yang, C. C., Hsu, S. T., Chien, W. C., Shih, M. C., Chiu, S. J., Lee, K. T., and Wang, C. L. *Int. J. Hydrogen Energ.* **31**(14), 2076 (2006).

[11] Débart, A., Paterson, A. J., Bao, J. L., and Bruce, P. G. *Angew. Chem. Int. Ed.* **47**, 4521 (2008).

[12] Larcher, D., Courjal, P., Urbina, R. H., GLrand, B., Blyr, A., du Pasquier, A., and Tarascon, J. M. *J. Electrochem. Soc.* **145**, 3392 (1998).

[13] Gao, Y., Wang, G., Wan, J., Zou, G., and Qian, Y. *J. Cryst. Growth* **279**, 415 (2005).

[14] Armstrong, A. R. and Bruce, P. G. *in preparation* .

[15] Patrice, R. *Universite de Picardie Jules Verne* (2001).

[16] Hunter, J. *J. Solid State Chem.* **39**, 142 (1998).

[17] Abraham, K. M. and Jiang, Z. *J. Electrochem. Soc.* **143**, 1 (1996).

[18] Read, J. *J. Electrochem. Soc.* **149**, A1190 (2002).

[19] Johnson, C. S., Dees, D. W., Manuetto, M. F., Thackeray, M. M., Vissers, D. R., Argyriou, D., Loong, C.-K., and Christensen, L. *J. Power Sources* **68**, 570 (1997).

Chapter 4

Effects of Different Particle Size and Morphology on the Electrochemical Performance of Rechargeable Li/O_2 Batteries

The introduction of Li/O_2 battery by replacing the positive intercalation electrode by the porous O_2cathode and reacting lithium directly with $O_2$from the air offers an alternative approach which has high energy density, is low cost and environmentally friendly. It was demonstrated that the nature of the catalyst is a key factor controlling the performance of the O_2 electrode. As material chemistry developed, new interesting, designable and controllable morphologies of the same material can be obtained by specific methods. Therefore it is interesting to study the effect of different particle size and morphology of the catalyst in the O_2 electrode on the electrochemical performance of a non-aqueous Li/O_2 cell.

4.1 Introduction

The positive electrode in the current generation of rechargeable lithium batteries presents one of the greatest barriers to increasing energy storage. There is known limit to theoretical capacity possible from intercalation type materials, of around 300 $mAhg^{-1}$. Therefore it is important to explore alternative approaches. By definition such approaches will be radical and will pose many interesting scientific questions as well as technological challenges. One such approach is the use of conversion reactions based on fluorides [1–3]. Another is the Li/O_2 battery, in which the positive intercalation electrode is replaced with a porous carbon electrode containing a catalyst in which Li^+ from the electrolyte and e^- from the electrode can combine reversibly with O_2 from the air [4–8]. The potential advantages are low cost (principally carbon) and high energy density.

The non aqueous Li/O_2 battery has received limited attention until recently [4–7]. Previous investigations have generally focused on its use as a primary battery. Quite recently it was demonstrated in the presence of a suitable catalyst the Li_2O_2 formed on discharge could be decomposed back to Li + O_2 on charging and that the cell could be cycled [8–10]. The use of α-MnO_2 nanowires as a catalyst has resulted in some of the highest reversible capacities reported to date, 3000 $mAhg^{-1}$ (normalised by the mass of carbon in the cathode or 505 $mAhg^{-1}$ based on the total mass of cathode + O_2 [10]. Evidently the catalyst plays an important role in the performance of the electrode.

In this chapter, several catalysts based on first row transition metal oxides each with three different morphologies, bulk, nanoparticulate and mesoporous were examined. Such first row transition metal oxides were chosen based on previous work which suggested that this class of materials proves effective catalyst for the non aqueous O_2 electrode. The influence of morphology on the discharge and charge voltage, discharge capacity and cyclability are examined.

4.2 Experimental

The bulk Mn_3O_4 was synthesised by solid state reaction (Mn_2O_3 (beta-, Strem chemicals Inc.) fired at 1200 °C for 12 h under air). The other bulk catalysts were obtained commercially (CuO: 99+ %, Sigma-Aldrich; NiO: BDH chemicals Ltd.; Co_3O_4 : powder < 10 μm , Aldrich). Nanoparticulate forms of the catalysts were obtained commercially (NiO: nanopowder, 99.8 %, Aldrich) or prepared by methods discussed in Chapter 2. Mesoporous morphologies were synthesised using the hard template route, details were discussed in Chapter 2. The catalyst materials were characterised by a variety of techniques including powder X-ray diffraction, transmission electron microscopy and N_2 adsorption-desorption. More details were discussed in Chapter 2.

The porous composite cathodes were prepared by mixing carbon, catalyst, PVDF (Kynar2801), and propylene carbonate (PC) (weight ratios of 11 : 19 : 15 : 55) as a slurry in acetone and spread onto glass using the Doctor Blade technique. The porous cathodes were incorporated into electrochemical cells along with a lithium metal counter/ reference electrode and an electrolyte consisting of $LiPF_6$ in PC. The cell was based on a swagelock design, one end of which was replaced by an aluminium mesh permitting gas exchange with the atmosphere. The cell was located within a chamber filled with one atmosphere of O_2 . Electrochemical measurements were carried out using a Macpile II Multichannel Cycler (Biologic, France).

4.3 Results and Discussion

Powder X-ray diffraction data of all the catalyst materials are presented in Figure 4.1, as well as the standard patterns. Inevitably the peaks in the powder patterns of the nanoparticulate and mesoporous solids are broadened due to the small particle size/ thin walls. However, in all cases the powder patterns are in good agreement with those anticipated for the corresponding

phases (Mn_3O_4 : JCPDS No. 24-734; Co_3O_4 : JCPDS No. 9-418; NiO: JCPDS No. 44-1159; CuO: JCPDS No. 48-1548). The mesoporous materials have all been prepared and characterised previously [11–14]. Their synthesis is carried out by a hard template route which a solution soluble precursor of the desired phase is infiltrated into the pores of a silica template, in this case KIT-6 with a 3D pore structure. Pulsination followed by dissolution of the silica template leaves a mesoporous transition metal oxide with a replica pore structure. In the case of Mn_3O_4 , the phase directly prepared within the template is Mn_2O_3 , which, following template removal, is reduced in an H_2 / Argon atmosphere to Mn_3O_4 with preservation of the mesostructure [13]. TEM measurements on the materials prepared for this work confirmed that in all cases the same 3-D pore structure separated by crystalline walls was obtained, see Figure 4.2. BET measurements confirmed previous results which showed that the pore diameters were $\sim$ 4 nm separated by walls of $\sim$ 8 nm thick [11–14]. The surface areas of all the materials reported in this work were measured by the BET method and are presented in Table 4.1.

Table 4.1: Measured BET surface area of different catalysts.

morphology / Catalyst	bulk	nanoparticulate	mesoporous
CuO	0.023 m^2g^{-1}	103.4 m^2g^{-1}	63.8 m^2g^{-1}
NiO	41.1 m^2g^{-1}	81.5 m^2g^{-1}	93 m^2g^{-1}
Co_3O_4	0.9 m^2g^{-1}	78.8 m^2g^{-1}	130.5 m^2g^{-1}
Mn_3O_4	0.2 m^2g^{-1}	35.1 m^2g^{-1}	99.7 m^2g^{-1}

The catalysts were combined with carbon and kynar to form porous electrode as described in the experimental section. All the electrodes were fabricated in the same manner. Although the weight ratios were the same in all cases, the differences in the catalysis surface areas resulted in the dominate surface area being carbon in the case of the bulk materials and the catalyst in the case of the high surface area nanoparticulate and mesoporous forms. The catalyst surface areas within the electrodes are presented in Table 4.1 for each catalyst.

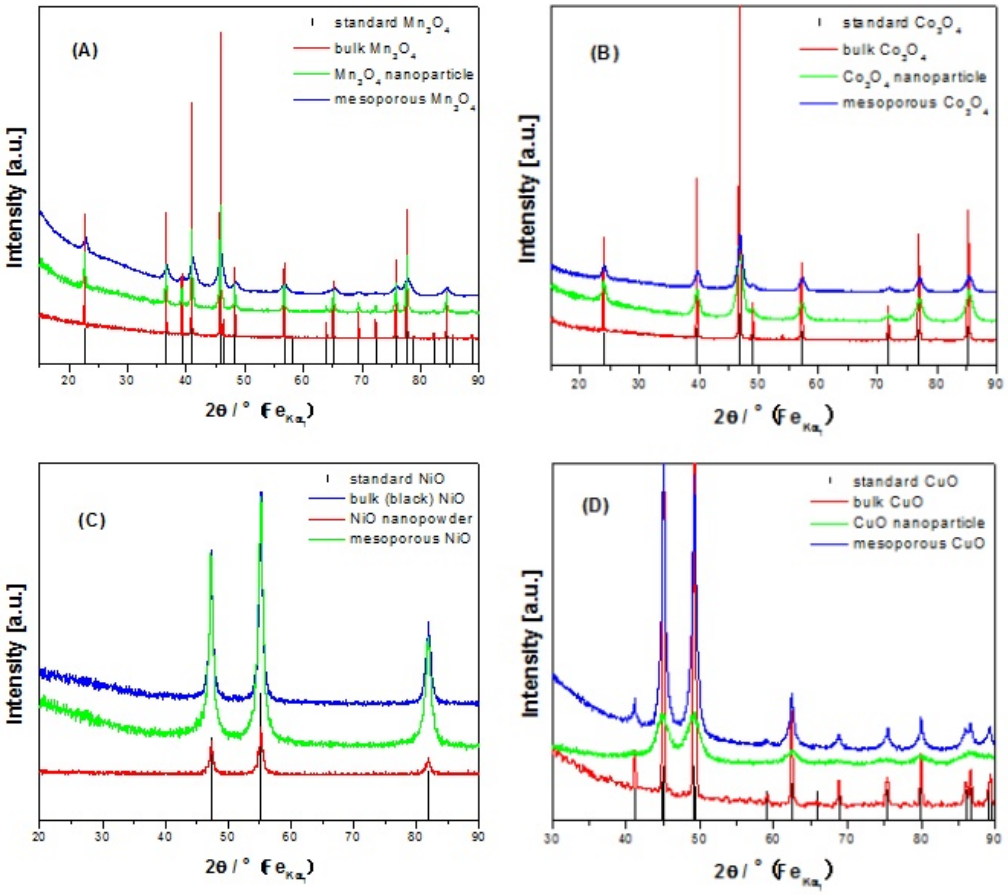

Figure 4.1: Powder XRD patterns for different catalysts including (A) Mn_3O_4, (B) Co_3O_4, (C) NiO, and (D) CuO in different morphologies.

The average discharge and charge potentials and the discharge capacities for the first cycle are presented in Table 4.2 with several representative load curves shown in Figure 4.3. The data demonstrate that the discharge potential varies very little with the catalysts type, surface area or morphology. In all cases studied here, it is in the region of 2.5 V versus Li^+/Li.

The trends in the first discharge capacity may be divided into two categories. For Mn_3O_4 and Co_3O_4 the catalyst surface area and morphology appear to have no significant influence on the discharge capacity, Table 4.2. This is despite the surface areas increasing over 130 fold on moving from the bulk to the mesoporous materials in the surface area of the electrode moving from domination by the carbon to the catalyst. It can be concluded that the

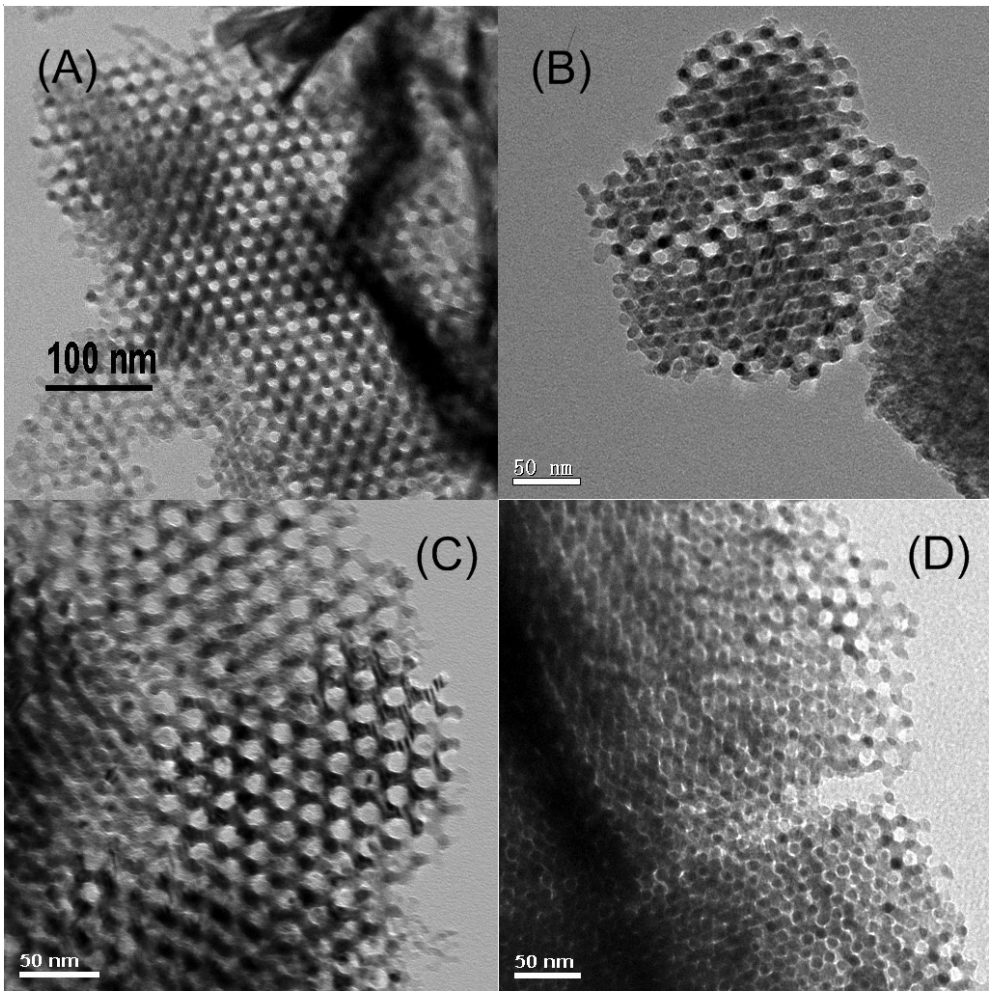

Figure 4.2: TEM images of different catalyst materials with mesoporous structure including (A) Mn_3O_4 , (B) Co_3O_4 , (C) NiO, and (D) CuO.

discharge capacity is insensitive to Mn_3O_4 and Co_3O_4 .

In contrast, the discharge capacities of NiO and CuO increase significantly on replacing the bulk catalyst with the nanoparticulate or mesoporous counterparts indicating that these catalysts have a significant influence on the discharge capacity. Comparing NiO and CuO, respectively, it appears that both surface area and morphology play a role in the discharge capacity. In both cases the nanoparticulate and mesoporous materials exhibited significantly higher surface areas than the bulk materials and, according to Table 4.2, dominate the surface areas of the electrode, as a result the

discharge capacities are substantially higher for these high surface area catalysts, Table 4.2. In the case of CuO, the nanoparticulate material has a significantly higher surface area than the mesoporous form yet the capacity is only marginally higher for the nanoparticulate form. Mesoporous NiO has a surface area of only slightly higher than nanoparticulate NiO yet the discharge capacity of the former is significantly greater than the latter. These results suggest that the mesoporosity does promote higher discharge capacities albeit a secondary factor when compared with total surface area.

Table 4.2: 1st discharge and charge potentials and 1st discharge capacities for different catalysts.

catalyst		1^{st} discharge potential (Volt vs. Li^+/Li)	1^{st} charge potential (Volt vs. Li^+/Li)	1^{st} discharge capacity ($mAhg^{-1}$)
Mn_3O_4	Bulk	2.52	4.37	1555
	Nanoparticulate	2.50	3.92	1277
	mesoporous	2.54	3.9	1665
Co_3O_4	Bulk	2.48	4.5	1396
	Nanoparticulate	2.54	3.79	1467
	mesoporous	2.52	3.86	1527
NiO	Bulk	2.52	3.86	1175
	Nanoparticulate	2.51	4.15	1363
	mesoporous	2.52	4.05	1716
CuO	Bulk	2.49	4.3	1158
	Nanoparticulate	2.51	3.85	1831
	mesoporous	2.52	3.99	1754

One of the problems encountered with the O_2 electrode is hysteresis between the charge and discharge potentials (the other factors and problems will be discussed in the following chapters). The charging voltage can be 1.5∼2 V higher than the discharge potential, as evident in the data presentating in Figure 4.3 and Table 4.2. As shown previously the presence of a catalyst is important in promoting reversibility of the electrode reaction [8,10]. Therefore, it is not surprising to observe that the catalyst influences

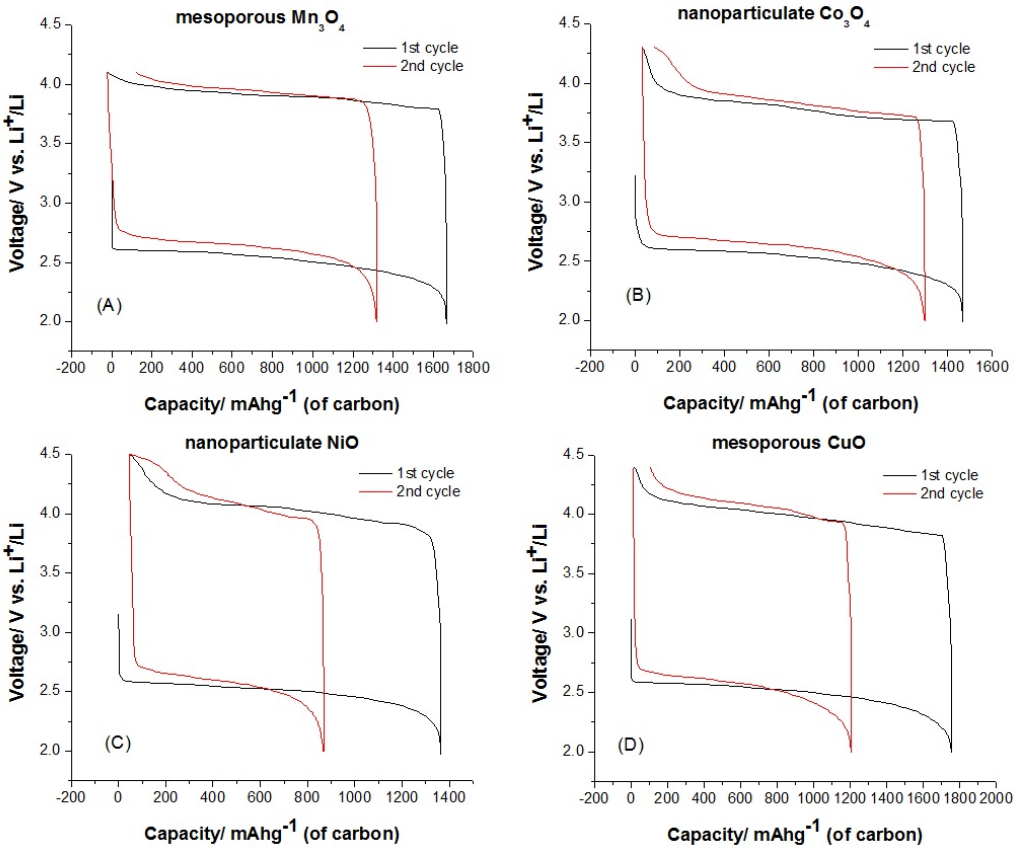

Figure 4.3: Variation of potential with state of charge for the porous electrode containing different catalysts including (A) mesoporous Mn_3O_4 , (B) nanoparticulate Co_3O_4 , (C) nanoparticulate NiO, and (D) mesoporous CuO, cycled at a rate of 70 mAg^{-1} .

the charging voltage, Table 4.2. Based on the materials reported here the charging voltage is lowered by increasing the surface area of the catalyst. Examination of the data for Mn_3O_4 and Co_3O_4 indicate a marked reduction in the charging potential on replacing the low surface area bulk material with the much higher surface area nanoparticulate or mesoporous morphologies, Table 4.2. The differences between the surface areas of the nanoparticulate and mesoporous materials are much smaller than the difference between the bulk material and either the nanoparticulate or the mesoporous materials, this is reflected in the rather similar charging voltages for nanoparticulate and mesoporous Mn_3O_4 and Co_3O_4 , Table 4.2. The bulk NiO material has a significantly higher surface area than either of the bulk manganese or cobalt

phases, and its charging potential is correspondingly lower. Considering the influence of morphology, the surface areas of the nanoparticulate and mesoporous NiO are similar yet a small decrease in the charging potential in the case of the mesoporous material maybe be discerned. However, differences in the morphology in the case of the manganese and cobalt phases do not appear to significantly influence the charging potential. In the case of CuO the nanoparticulate material has a lower charging potential than the mesoporous material, although this may be due to its higher surface area. Overall, we cannot conclude from these data that there is any systematic influence of morphology on the charging potential. The dominant factor controlling the charging potential for any given catalyst appears to be its surface area.

Given the significant difference in potential between charge and discharge, it is interesting to consider whether the oxidation states of the catalysts could change on charge or discharge, since this might influence their effect on the electrochemical performances. The cut-off potential on discharge is 2 V, this is sufficiently high to avoid reduction of the catalysts. Lithium intercalation into Mn_3O_4 occurs at approximately ∼1.5-1.8 V versus Li^+/Li, the intercalation into Co_3O_4 occurs at ∼1.2 V versus Li^+/Li and CuO is reduced to $Li_2O + Cu$ at ∼1.1-1.3 V. NiO undergoes reduction at even lower potentials, ∼0.7 V. It is confirmed by powder X-ray diffraction data that there is no significant change in the peak positions or the peak intensities in the patterns of all the catalysts studied at the end of discharge. This suggests the materials retain their structures on discharging. Considering possible redox couple switching at the charging potential, it is possible that oxidation of Mn^{2+} to Mn^{3+} and Co^{2+} to Co^{3+} in Mn_3O_4 and Co_3O_4 , respectively, could occur as the oxidation of Ni^{2+} to Ni^{3+} in NiO. It is reported from electrochemical studies on these phases that such oxidation can be anticipated [15–17]. It is less likely that Cu^{2+} will be oxidised to Cu^{3+} at the charging potentials. Powder X-ray diffraction data collected at the end of charge shows no evidence of significant change in the bulk catalysts. Therefore it suggests that the oxidation states of the catalysts are

invariant or at least if they do change this occurs as a transient intermediate state during the electrochemical process. For example, it is possible that oxidation of the catalyst associated with uptake of oxygen on the surface but from decomposition of the Li_2O_2 could occur with this oxygen then being evolved so that the overall state of the surface does not undergo a long term change.

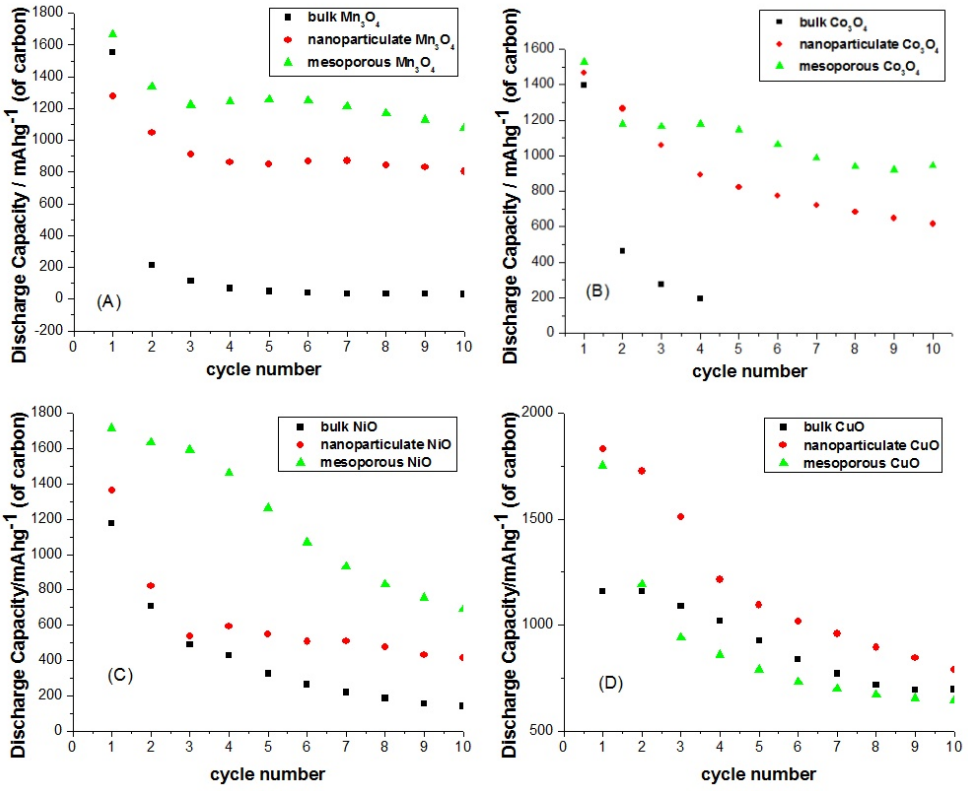

Figure 4.4: Variation of discharge capacities with cycle number for the porous electrode containing different catalysts, including (A) Mn_3O_4 , (B) Co_3O_4 , (C) NiO, and (D) CuO, with different morpologies, based on the mass of carbon.

Turning to the capacity fading on cycling, results for all four catalysts are presented in Figure 4.4. In most cases fading is significant, as noted previously if electrodes are taken to deep discharge.[8–10] However, it is apparent that the higher the surface area of the catalysts, the higher the capacity on cycling. Given that, the manganese and cobalt phases show very similar first discharge capacities, i.e. the formation of Li_2O_2 is insensitive

to the catalysts in these cases, the higher capacity on cycling must reflect the degree to which the catalysts promote the reversibility of the reaction. It is apparent that morphology can also play a role. The mesoporous materials appear to give better capacity retention on cycling than the nanoparticles or the bulk materials. Only CuO seems to be an exception to this rule because the CuO catalyst materials with bulk, nanoparticulate or mesoporous morphologies all show the similar capacity fading. Since the mesoporous morphologies are maintained throughout the cycling process for all materials and there is no evidence for changes in redox states or bulk structure on cycling, it is not at this point clear why the CuO appears exceptional in this regard.

4.4 Conclusions

Several first row transition metal oxides have been investigated as catalysts in the O_2 electrode of the Li/O_2 battery. Selection was based on past screening of a number of transition metal oxides materials. For each catalyst bulk, nanoparticulate and mesoporous morphologies were considered. The discharge capacity is unaffected by the presence of Mn_3O_4 and Co_3O_4 whereas increasing the surface area or, to a lesser extent, employing a mesoporous morphology, increases the discharge capacity in the case of NiO and CuO. For all catalysts studied increasing the surface area reduces the charging potential although the discharge potential remains invariant. Charging potentials can be reduced from around 4.5 V to 3.79 V versus Li^+/Li. Performance of cycling is certainly enhanced by an increase in the surface area and capacity retention is better for the mesoporous morphologies and simple nanoparticles in most cases. These results certainly raise important questions concerning the origin of the observed behaviour. More work need to to be done to understand the electrochemical mechanisms involved within the O_2 electrode.

References

[1] Bervas, M., Klein, L. C., and Amatucci, G. G. *J. Electrochem. Soc.* **153**, A159 (2006).

[2] Bervas, M., Mansour, A. N., Yoon, W. S., Al-Sharab, J. F., Badway, F., Cosandey, F., Klein, L. C., and Amatucci, G. G. *J. Electrochem. Soc.* **153**, A799 (2006).

[3] Bervas, M., Badway, F., Klein, L. C., and Amatucci, G. G. *Electrochem. Solid-State Lett.* **8**(4), A179 (2005).

[4] Abraham, K. M. and Jiang, Z. *J. Electrochem. Soc.* **143**, 1 (1996).

[5] Read, J. *J. Electrochem. Soc.* **149**, A1190 (2002).

[6] Read, J., Mutolo, K., Ervin, M., Behl, W., Wolfenstein, J., Drieger, A., and Foster, D. *J. Electrochem. Soc.* **150**, A1351 (2003).

[7] Kuboki, T., Okuyama, T., Ohsaki, T., and Takami, N. *J. Power Source* **146**, 766 (2005).

[8] Ogasawara, T., Débart, A., Holzapfel, M., Novak, P., and Bruce, P. G. *J. Am. Chem. Soc.* **128**, 1390 (2006).

[9] Débart, A., Bao, J. L., Armstrong, G., and Bruce, P. G. *J. Power Sources* **174**, 1177 (2007).

[10] Débart, A., Paterson, A. J., Bao, J. L., and Bruce, P. G. *Angew. Chem. Int. Ed.* **47**, 4521 (2008).

[11] Jiao, F., Hill, A. H., Harrison, A., Berko, A., Chadwick, A. V., and Bruce, P. G. *J.Am.Chem.Soc.* (2008).

[12] Shaju, K. M., Jiao, F., Débart, A., and Bruce, P. G. *Phys.Chem.Chem.Phys.* **9**, 1837 (2007).

[13] Jiao, F., Harrison, A., Hill, A. H., and Bruce, P. G. *Adv.Mater.* **19**, 4063 (2007).

[14] Ren, Y. and Bruce, P. G. *in preparation* .

[15] Messaoudi, B., Joiret, S., Keddam, M., and Takenouti, H. *Electrochim. Acta* **46**, 2487 (2001).

[16] Adhikary, K., Takahashi, M., and Kikkawa, S. *Mater. Res. Bull.* **33**(12), 1845 (1998).

[17] Wu, M. S., Yang, C. H., and Wang, M. J. *Electrochim. Acta* **54**, 155 (2008).

Chapter 5

Other Factors that Influence the Performance of rechargeable Li/O_2 battery

The most important factor influencing the O_2 electrode reaction is the catalyst. However there remain other fundamental and practical issues to be addressed, including optimization of electrode porosity, structure and composition, as well as avoidance of H_2O or CO_2 ingress when operated in air. $LiPF_6$ in propylene carbonate may not be the best electrolyte. New electrolytes like ionic liquids, which are not miscible with water, may offer an attractive alternative. Here some of these other factors which could influence the performance of the Li/O_2 battery are presented.

5.1 Effect of the Type of Carbon (Comparison of Different Carbons)

Several carbons with different surface areas, such as Super S, Super P, Vulcan and Ketjen Black, have been studied with the same catalyst (EMD). Ketjen Black, which has the highest surface area, gives a much higher initial capacity but poor capacity retention on cycling than the other carbons.

Table 5.1: Measured BET surface area of different carbons.

Different Carbon	Ketjen Black	Super P	Super S	Vulcan
Surface area (m^2g^{-1})	749	30.6	48.8	193

Figure 5.1 presents the specific capacity of different carbons with the same catalyst, EMD, binder and electrode composition. Table 5.1 shows the surface area of the different carbons studied. It was found that the surface area of the carbon is the most important factor determining the initial discharge capacity. The carbon with the higher surface area provides more available sites for Li ions to react with O_2 and form Li_2O_2 . However, the formation of a large amount of Li_2O_2 in the pores can result in them becoming blocked or cause expansion of the electrode resulting in a loss of contact between electrode particles during subsequent recharging. This might be the reason of the rapid decrease of discharge capacity during cycling for Ketjen Black and Vulcan, which have higher surface areas than the others.

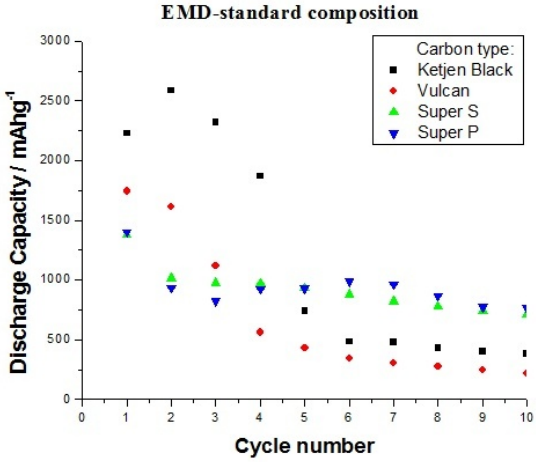

Figure 5.1: Variation of discharge capacity with cycle number for porous electrodes containing EMD catalyst and a range of dense carbon materials.

As discussed in Chapter 3 and 4, the application of nanomaterials as catalyst in the cathode could improve the cycling performance.[1,2] Figure 5.2 shows the variation of discharge capacity with cycle number on different carbons with the same α-MnO_2 nanowires catalyst, binder and electrode

composition. Interestingly, the performance is promising with electrodes prepared with Ketjen Black having higher capacity per gram of carbon and similar capacity retention on cycling compared to our previously published α-MnO_2 nanowires + Super P carbon results (shown in red).[1] Considering the similar surface areas of EMD and α-MnO_2 nanowires, in this case, the morphology of the nanomaterials acts the key role in improving the cycling performance. It confirms the performance improvement by using nanosized material as catalyst in the cathode and leaves us a hope to further improve the performance by using higher surface area carbon material. More details of the performance of Ketjen Black will be discussed later in this chapter.

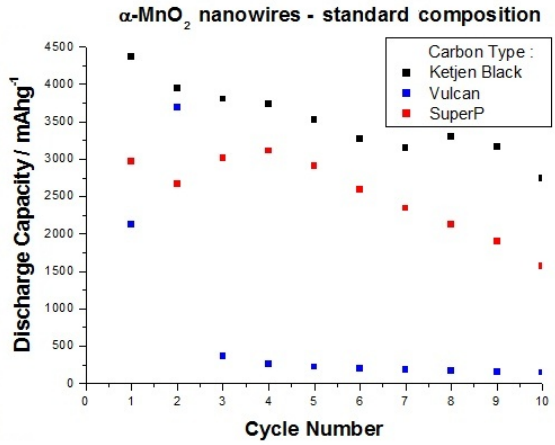

Figure 5.2: Variation of discharge capacity with cycle number for porous electrodes containing α-MnO_2 nanowires catalyst and a range of dense carbon materials.

Because the high surface area carbons exhibit more capacity fade despite a higher initial capacity, Super P with the lowest surface area also with the most stable performance has been chosen for the normal study.

5.2 Effect of the Type of Binder

Several kinds of binders, specifically polyvinylidene fluoride (PVDF), polytetrafluoroethylene (PTFE) and ethylene-propylene-diene monomer (EPDM), were studied in the O_2 electrode. PVDF and PTFE were used because

fluorinated polymers are known as a good O_2 transport medium, and EPDM because it provides a comparison with the fluorinated polymers. Moreover, EPDM as a more flexible polymer allows to explain how the changes in the mechanical properties affect performance.

Investigations using PTFE as binder were not particularly successful. Both EMD and α-MnO_2 nanowires as the catalyst showed poor electrochemical performance with low capacity and poor capacity retention on cycling. Also a relatively high amount of binder, > 15 % by mass (standard composition), was required in order to form free standing plasticised films suitable for electrode preparation. The second binder to be investigated was EPDM, trade name 'Vistalon'. Although this type of elastomer is commonly used in conventional lithium ion battery electrodes as a binder material, the electrochemical results when used in the Li/O_2 system are poor, see Figure 5.3. The electrode films had to be prepared using hexane to dissolve the polymer. PVDF (Kynar Flex 2801) was the best binder studied. So all electrochemical tests were performed with porous composite electrodes contained Kynar Flex 2801 as the standard polymeric binder material.

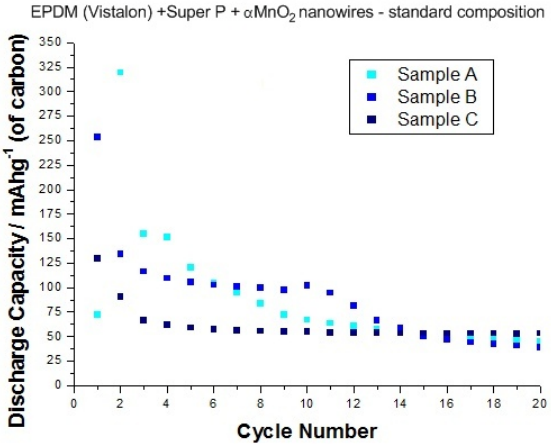

Figure 5.3: Variation of discharge capacity versus cycle number for three companion composite electrodes containing α-MnO_2 nanowires catalyst, Super P carbon and EPDM as polymeric binder in the standard composition mass ratios.

5.3 Effect of the Type of Electrolyte

Due to the high charging voltage (4 $\sim$ 4.5 V), carbonate solvents and fluorinated salts have been chosen as the solvent and salt for the electrolyte in the Li/O_2 battery. In this thesis, 1 M $LiPF_6$ in PC was used as the electrolyte for most of the studies. Propylene carbonate was used because it is stable to high potentials ($\sim$ 5 V), forms a stabilizing SEI layer on Li metal, is a good solvent with high relative dielectric constant (64.4) and most importantly has a high boiling point (241.7 °C) and low volatility reducing the evaporation of the electrode gas interface. Certain problems caused by this system will be discussed in an other chapters.

Alternative electrolytes which have even lower volatility or higher stability have also been investigated. Several salts ($LiPF_6$, $LiAsF_6$ and $LiSbF_6$) from the same family have been studied in different solvents (PC, ionic liquid (methylpropylpiperidinium bis(fluorosulfonyl)imide (MPPI-FSI) with low volatility), and sulfolane (with high charging voltage)) by cyclic voltammetry (CV). To carry out the CVs, the same swagelok cell as used for the Li/O_2 battery was employed but with the composite electrode replaced by an aluminum grid (see Figure 2.5, Chapter 2). The experiments were carried out in the voltage range of 2 $\sim$ 5.1 V at the scan rate of 0.116 mVs^{-1} under O_2 . In the case of sulfolane (m.p. 20-26 °C), the experiments were carried out at 35 °C . Because of the relatively low solubility of the salts in IL and sulfolane, the electrolytes based on these solvents had a maximum concentration of 0.25 M.

Figure 5.4 shows the cyclic voltammograms (CVs) of the electrolytes studied. In the first negative sweep the peak around 2.5 V (vs. Li^+/Li) which is assigned to the reduction of oxygen appeared in all cases and especially distinct in the cases of PC and sulfolane. In the second negative sweep, this peak shifted to higher potential which is in good accordance with their galvanostatic cycling. The peaks in the positive sweep associated with the oxidation of the superoxide or peroxide anion (around 3.5 V) and probably the oxidation of the Al grid and decomposition of the solvent species ($>$ 4 V).

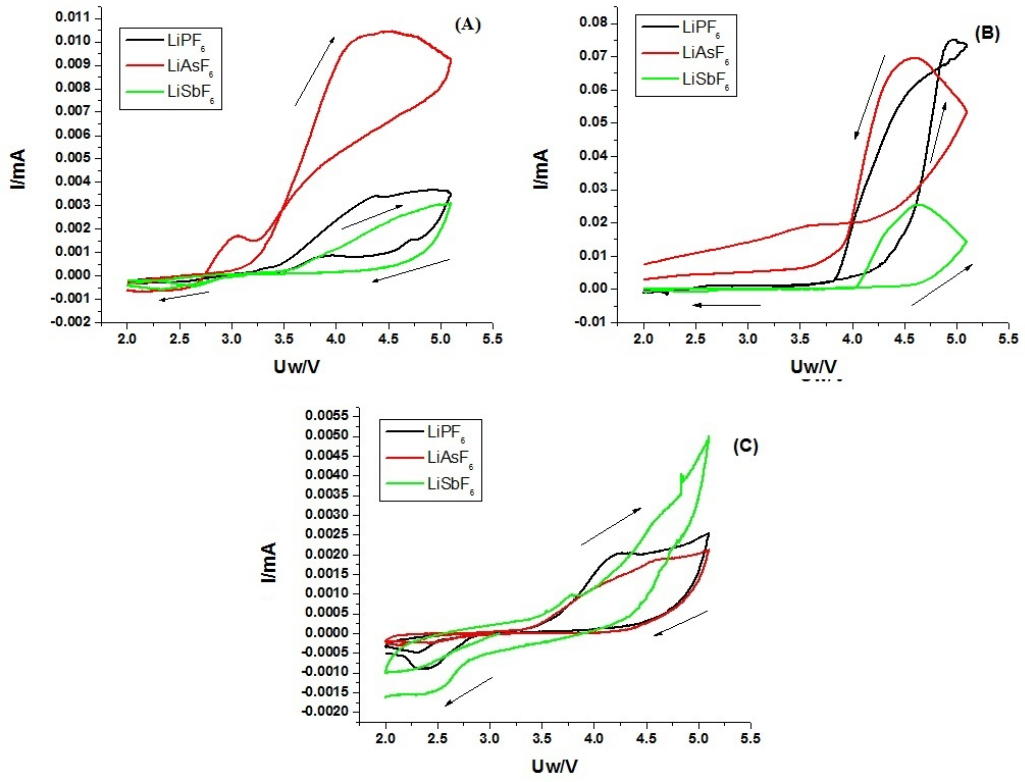

Figure 5.4: Cyclic voltammograms of various salts dissolved in different solutions including: (A) PC; (B) IL (MPPI-FSI); and (C) sulfolane over a voltage range of 2 to 5.1 V at a scan rate of 0.116 mV/s.

The current intensity represents the activity of the reaction. Table 5.2 lists the values of the current in the positive sweep when the potential reaches 4 and 4.5 V. The currents observed with the electrolytes investigated displayed the following trend in decreasing stability (higher current) with respect to salt type: $LiSbF_6 > LiPF_6 > LiAsF_6$ in PC; $LiSbF_6 > LiPF_6 > LiAsF_6$ in IL; $LiAsF_6 > LiPF_6 > LiSbF_6$ in sulfolane. Table 5.3 lists the promising electrolytes studied.

Modified cyclic voltammetry experiments were performed on the promising electrolytes. The same cell and the same conditions were used as in the previous experiments. The voltage was swept from OCV to the negative direction and back to 4.75 V and 5 V, respectively. They were then kept constant to study the evolution of current with time at the particular

Table 5.2: Current values at 4 V and 4.5 V.

Solvents	Salts	Positive current value at 4 V (μA)	Positive current value at 4.5 V (μA)
PC	$LiPF_6$	2.4	3.4
	$LiAsF_6$	8.9	10.4
	$LiSbF_6$	1.2	2.3
Ionic liquid	$LiPF_6$	3.9	17
	$LiAsF_6$	20	26.5
	$LiSbF_6$	0.5	1.0
sulfolane	$LiPF_6$	1.5	2.0
	$LiAsF_6$	1.2	1.8
	$LiSbF_6$	1.2	2.6

Table 5.3: Promising Electrolytes.

Electrolyte	Voltage at 2 μA in 1st sweep (V)	Highest current value (μA)
1 M $LiSbF_6$ in PC	4.35	3.1
0.25 M $LiPF_6$ in sulfolane	4.25	2.5
0.25 M $LiSbF_6$ in sulfolane	4.6	2.3
0.25 M $LiAsF_6$ in sulfolane	5	2.1

potentials. Figure 5.5 shows the variation of current intensity with time. The area represents the stability of the electrolyte in this system at the given voltage. The electrolytes with sulfolane are more stable than the ones with PC.

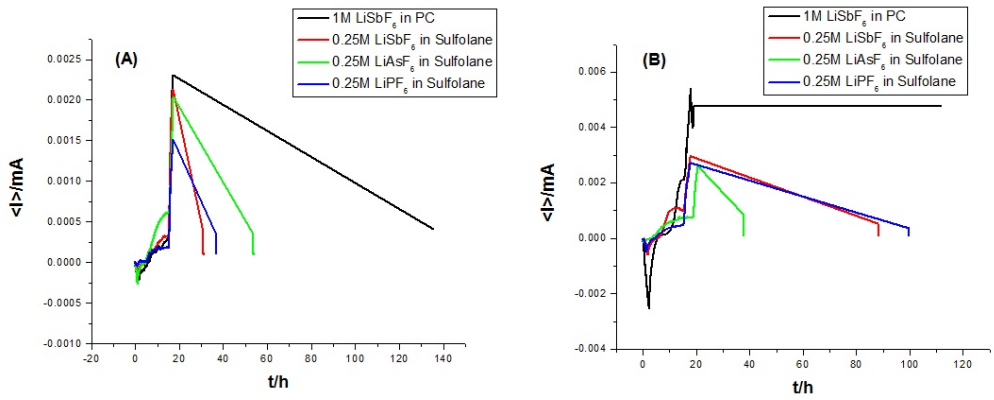

Figure 5.5: Current-time curves after cyclic voltammetry from OCV – 2 V – 4.75 V (A) and 5 V (B) of various promising electrolytes, and holding the potentials thereafter at a scan rate of 0.116 mVs^{-1}.

The cycling performance was studied in the sulfolane electrolytes at 35 °C . EMD and the best catalyst so far, α-MnO_2 nanowires, were used to study the cycling. For EMD, higher charge voltage cut-off is required in all sulfolane electrolytes than in the 1 M $LiPF_6$ in PC, and reasonable cycling only appeared in the electrolyte with $LiAsF_6$ salt, see Figure 5.6. For the α-MnO_2 nanowires catalyst, a higher charge voltage was also required for the electrolyte with $LiSbF_6$ salt, however the cycling performances are presented in Figure 5.7. Although none of the investigated electrolytes showed better performance than 1 M $LiPF_6$in PC in terms of capacity and capacity retention on cycling, the high oxidation stability of sulfolane and IL makes their further study of interest.

In summary, $LiAsF_6$ in sulfolane seems to be the most promising electrolyte of the electrolytes studied. More work needs to be done to address the problems of this system such as finding the proper working temperature.

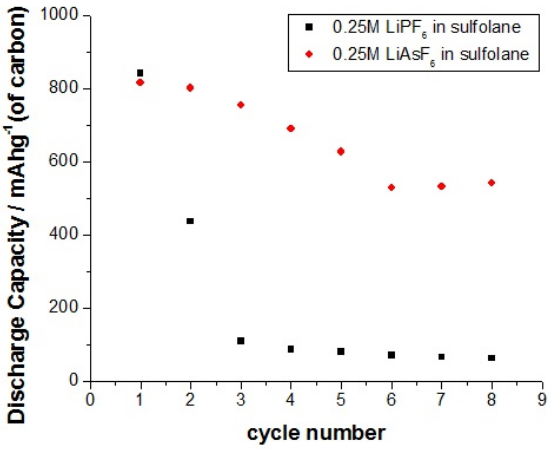

Figure 5.6: Variation of discharge capacity with cycle number for porous electrodes containing EMD catalyst 0.25 M $LiPF_6$ in sulfolane and 0.25 M $LiAsF_6$ in sulfolane, respectively, as the electrolyte.

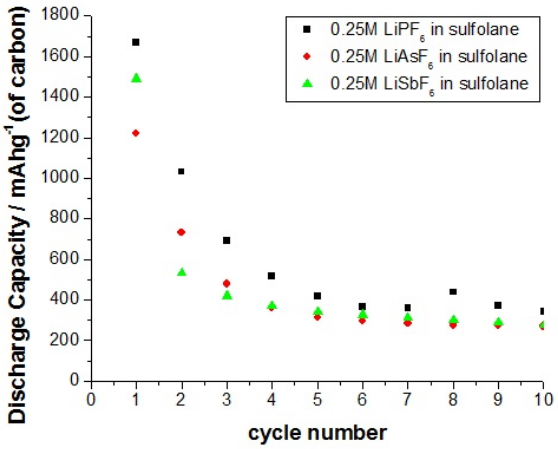

Figure 5.7: Variation of discharge capacity with cycle number for porous electrodes containing α-MnO_2 nanowires catalyst in various electrolytes including: 0.25 M $LiPF_6$ in sulfolane, 0.25 M $LiAsF_6$ in sulfolane and 0.25 M $LiSbF_6$ in sulfolane.

5.4 Calculating the Total Capacity of the Electrode

As mentioned in Chapter 3, a convention of normalising the capacity of the electrodes by mass of carbon has been employed for most of the studies in this thesis. However a more scientific calculating method is required to compare the specific capacity of an O_2 electrode and the total mass of the electrode may be used.

Porous gas electrodes are not new; they are ubiquitous in fuel cells, and aqueous batteries containing air cathodes, e.g. Zn/ air and Fe/ air, have been known for sometime. The convention of normalising the capacity of air electrodes by the mass of carbon has been used for some years, a convention that has been adhered to in this work. Reasons for the convention are that carbon is the dominant component of the porous electrode and the electrode mass increases as discharge proceeds, due to the accumulation of Li_2O_2 in the electrode. However, the simplicity of this convention somewhat obscures a direct comparison of the specific capacity of an O_2 electrode with that of an intercalation cathode. The total mass of the cathode at the end of discharge may be used to calculate the specific capacity (carbon + binder + catalyst + Li_2O_2). However, ultimately it is the contribution to the capacity of the whole battery that matters and including Li_2O_2 overestimates the mass gained during discharge, since only the mass of O_2 is added to the cell; the Li, which comes from the anode, would be counted twice (The mass of Li is not included in calculating the specific capacity of a V_2O_5 electrode, for example). Even allowing for this correction, the use of total cathode mass plus O_2 gained is only strictly relevant at the deepest discharge.

The O_2 electrode that gives the best performance so far, i.e. using α-MnO_2 nanowires as catalyst, was selected to demonstrate the performance taking account of all the electrode mass. Figure 5.8 shows the specific capacity for the α-MnO_2 nanowires based on total electrode mass at the beginning (carbon + binder + catalyst) and end (carbon + binder + catalyst

+ O_2) of discharge. Converting the initial capacity for the α-MnO_2 nanowires electrode 3000 $mAhg^{-1}$ (based on carbon alone) into the specific capacities based on the total masses gives 730 $mAhg^{-1}$(carbon + binder + catalyst) and 505 $mAhg^{-1}$ (carbon + binder + catalyst + O_2). For the restricted capacity cycling shown in Chapter 3[1], the specific capacity 2400 $mAhg^{-1}$ (carbon) would be 540 $mAhg^{-1}$(carbon + binder + catalyst) and 408 $mAhg^{-1}$(carbon + binder + catalyst + O_2). Since in the case of intercalation electrodes only the mass of active material is usually employed to calculate specific capacities, comparison requires addition of the mass of carbon and binder to normalise the charge passed. For a typical mass ratio in a composite cathode containing an intercalation compound, 85 : 10 : 5 (active : carbon : binder), the specific capacities for $LiCoO_2$, $LiCo_{1/3}Mn_{1/3}Ni_{1/3}O_2$, $LiMn_2O_4$and $LiFePO_4$, based on the total mass would be 111 $mAhg^{-1}$, 170 $mAhg^{-1}$, 102 $mAhg^{-1}$and 132 $mAhg^{-1}$ respectively. Clearly the capacities of the O_2 cathode far exceed these values.

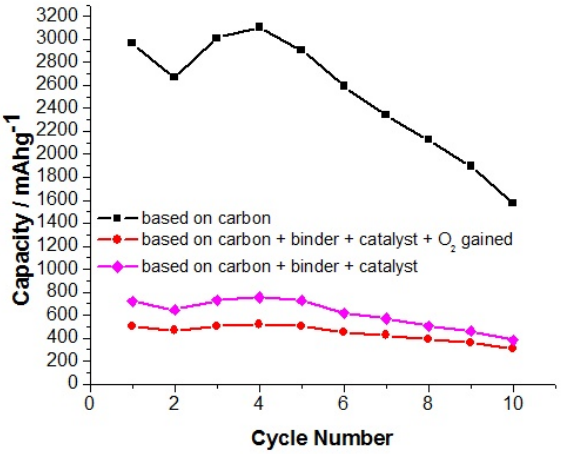

Figure 5.8: Variation of discharge capacity with cycle number for porous electrodes containing α-MnO_2 nanowires as the catalyst based on carbon, total electrode mass at the beginning (carbon + binder + catalyst) and end (carbon + binder + catalyst + O_2) of discharge.

In order to maximise the specific capacity of the O_2 electrode, it is important to reduce the mass. The heaviest component is the catalyst. Since the activity depends on surface area, the smaller the particle the higher

the surface to flow into and hence the lower the mass loading for a given surface area. Therefore, if the dimensions of the α-MnO_2 nanowires were to be reduced to a diameter and length of 10 nm and 200 nm respectively, the loading (mass of catalyst in the electrode) could be reduced by 72 % while maintaining the same surface area, leading to specific capacities of 1076 $mAhg^{-1}$(carbon + binder + catalyst) and 655 $mAhg^{-1}$(carbon + binder + catalyst + O_2).

An estimate of the maximum capacity that may be expected from an O_2 electrode can be made. If it is assumed a carbon cathode with a porosity of 75 % (such porosity should still ensure electron percolation through the carbon matrix) and based on Li_2O_2 formation but considering the mass gain to be only O_2 , a value of 1220 $mAhg^{-1}$ is obtained. This of course does not allow for the mass of binder or catalyst and therefore in practice values will be lower.

5.5 Investigation of Fabrication Methods - Composition Ratios

Having identified an optimum catalyst the next stage, based on the discussion above in Section 5.4, must be to minimise the proportion of catalyst and binder. The effect of the relative proportions of carbon, binder and catalyst on the electrochemical performance has been investigated. A range of carbon materials in conjunction with KynarFlex and α-MnO_2 nanowires as catalyst have been studied.

For most of the work reported in this thesis, the mass ratios of PC : carbon : catalyst : binder were fixed to 55 : 11 : 19 : 15, i.e. 0.57 : 1 carbon to catalyst. Because the catalyst is the heaviest component, specifically effort was devoted to investigating the effect of lowering the proportion of catalyst since the lowest catalyst proportion if combined with very small catalyst particle could provide the optimum performance. Table 5.4 lists the different porous electrode compositions investigated with Super P carbon. Some of the

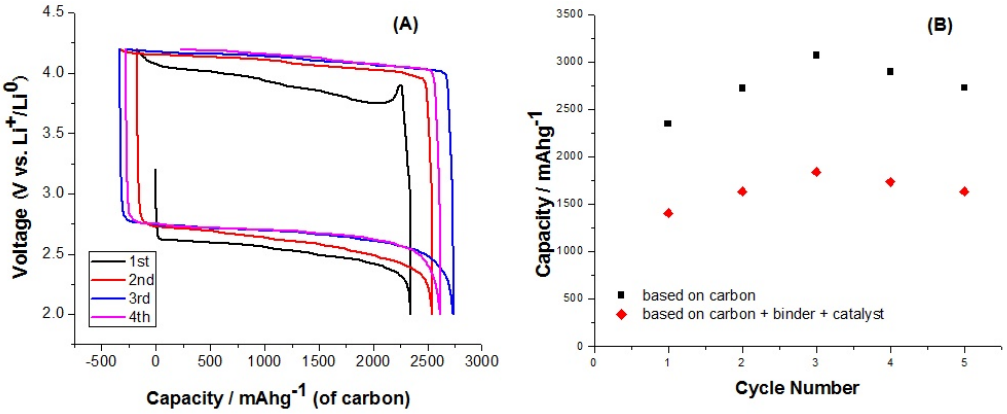

Figure 5.9: (A) Variation of voltage on discharge then charge for the porous electrode containing PC : Super P : α-MnO_2 nanowires : Kynar at the mass ratio of 2 : 1.2 : 0.3 : 0.5. (B) Variation of discharge capacity with cycle number for porous electrodes containing α-MnO_2 nanowires as the catalyst based on carbon and total electrode mass (carbon + catalyst + binder).

attempts failed to cast successfully. Some successful castings show inferior electrochemical performance in terms of lower than normal capacity and poor capacity retention on cycling. Only ratio 5, 6, 9, 13 and 14 show reasonably good performance. The result from ratio 14 is expected to have the highest specific capacity based on total mass of electrode because of the highest proportion of carbon to catalyst studied. Figure 5.9 shows the electrochemical performance of the composition with the mass ratios of 2 : 1.2 : 0.3 : 0.5 PC : Super P : α-MnO_2 nanowires : Kynar. The variation of voltage on discharge and charge, Figure 5.9A, and the variation of discharge capacity with cycle number, per gram of carbon, Figure 5.9B, are very similar to the voltages and capacity retentions from the ratio normally used (55 : 11 : 19 : 15). However, the capacity based on total electrode mass is significantly higher (1400 $mAhg^{-1}$ based on total mass, in the first cycle) than the normal composite electrode (730 $mAhg^{-1}$ based on total mass, in the first cycle), demonstrating the improved performance by changing the composition. This is the best specific capacity for Super P carbon based on total electrode mass obtained so far.

For carbons with higher surface areas than Super P, e.g. Vulcan and

Table 5.4: Attempts on various mass ratios of PC : carbon : catalyst : binder on Super P carbon.

Sample No.	PC: Super P: catalyst: Kynar	Notes
Ratio 1	2 : 1 : 0.75 : 0.25	unable to cast successfully
Ratio 2	2 : 1 : 0.25 : 0.75	
Ratio 3	2 : 1 : 0.65 : 0.35	
Ratio 4	2 : 0.8 : 0.65 : 0.65	
Ratio 5	2 : 0.7 : 0.65 : 0.65	Pre-grind dry powders prior to dispersion in acetone, mechanically stirred for 2 to 3 hrs
Ratio 6	2 : 0.8 : 0.55 : 0.55	
Ratio 7	2 : 0.66 : 0.66 : 0.66	
Ratio 8	2 : 0.8 : 0.5 : 0.7	
Ratio 9	2 : 1 : 0.5 : 0.5	
Ratio 10	2 : 1 : 0.4 : 0.6	
Ratio 11	2 : 1 : 0.3 : 0.7	
Ratio 12	2 : 1 : 0.45 : 0.7	
Ratio 13	2 : 1.1 : 0.4 : 0.5	
Ratio 14	2 : 1.2 : 0.3 : 0.5	
Ratio 15	2 : 1.3 : 0.2 : 0.5	

Ketjen Black, it is more difficult to cast the electrode at high ratios of carbon to catalyst. The best electrochemical performances from these alternative carbons were obtained when the composite electrode was fabricated using the following mass ratios: 50 % PC, 25 % carbon, 12.5 % α-MnO_2 nanowires, 12.5 % Kynar. The results of which are shown in Figure 5.10. The performance of the Ketjen Black electrodes is the best at this ratio when normalised against total electrode mass (carbon+binder+catalyst).

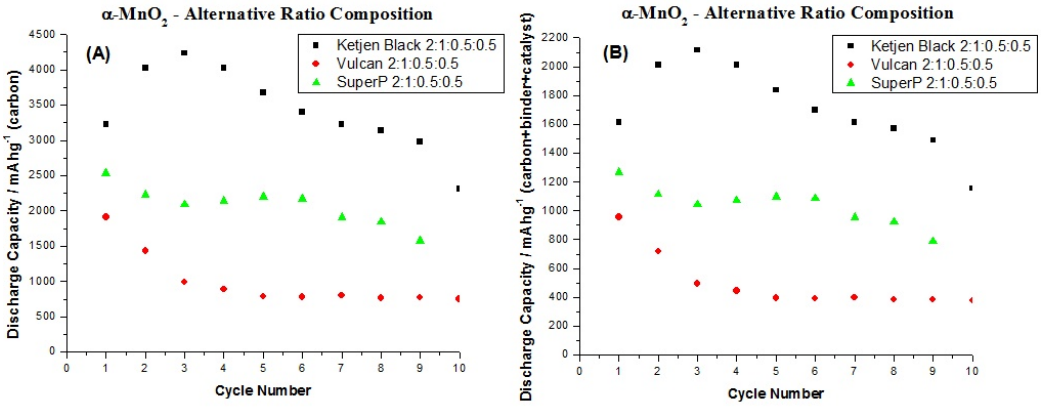

Figure 5.10: (A) Variation of discharge capacity, per gram of carbon, with cycle number for porous electrodes containing PC : Carbon : α-MnO_2 nanowires : Kynar at the mass ratio of 2 : 1 : 0.5 : 0.5 for the various carbon types and (B) normalised against total electrode mass (carbon + catalyst + binder).

5.6 Investigation of Manganese Oxide Loaded Carbons

It is known that in the porous electrodes (e.g. polymer electrolyte fuel cell), initially loading the catalyst on the carbon can improve the activity per unit mass of the catalyst.[3–5] To further improve the efficiency of the catalyst, investigation of loading the catalyst onto the carbon was undertaken. Two issues have to be noted: controlling the ratio of catalyst to carbon; and how to make the catalyst loading on the carbon homogeneous. Loadings that maintained the mass ratio used as a standard in the thesis (55 % PC, 11 %

Carbon, 19 % Catlayst, 15 % Binder) did not show significant improvement in performance. However it did prove the possibility to establish carbon loaded catalyst with better performance than non-loaded electrodes.

Investigations were undertaken to optimise the Li/O_2 system by minimising the amount of catalyst and binder required while maintaining high specific capacity when considering the total electrode mass (carbon + catalyst + binder) and not just the mass of carbon, and with good capacity retention on cycling.

MnO_x catalysts were selected because they were proved to be the best combined with low cost and toxicity. Manganese loaded carbon materials were prepared by adding a manganese nitrate solution to a mixture of carbon in H_2O .[4,5] This is stirred to ensure homogeneity before driving off water at 80 °C overnight. The resulting powder is then fired under air for 1 hour. A range of temperatures was investigated in order to determine the influence of temperature on the crystal structure and composition of the deposited MnO_x material. Also, a range of catalyst loadings were investigated, 4 : 1, 6 : 1, 8 : 1 and 12 : 1 carbon to manganese oxide mass ratios. Materials to be loaded include Super P, Ketjen Black, Vulcan and an activated Super P (pretreated with nitric acid). The porous electrodes were fabricated using the following mass ratios: 50 % PC, 40 % carbon and loaded catalyst, 10 % Kynar and 50 % PC, 35 % carbon and loaded catalyst, 15 % Kynar, for the carbons with low surface area (Super P and activated Super P) and high surface area (Ketjen Black and Vulcan), respectively.

The best performance obtained to date is from Ketjen Black loaded with MnO_2 and with a C to MnO_2 ratio of 8 : 1 obtained by firing at 250 °C . More details are discussed below.

Powder X-ray diffraction patterns of the materials loaded onto Super P are very poor due to high background from amorphous carbon and very broad peaks due to small, poorly crystalline, particles of MnO_x (see Figure 5.11). Powder diffraction patterns obtained from loaded materials using Vulcan and Ketjen Black show even less well defined diffraction peaks but follow a similar

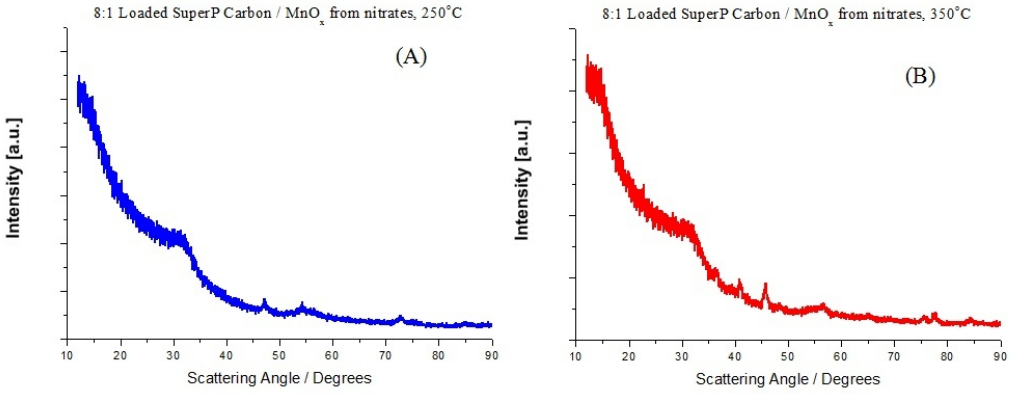

Figure 5.11: (A) Powder X-ray diffraction pattern obtained from manganese loaded Super P carbon heated at 250 °C. Pattern matches closely to that of chemically deposited manganese dioxide (CMD) and appears to be predominantly the γ-MnO_2 phase; (B) Powder X-ray diffraction pattern obtained from Manganese loaded Super P carbon heated at 350 °C. Pattern still shows some peaks that can be associated with MnO_2 materials but also shows some reflections that may be attributed to more oxygen deficient species Mn_2O_3.

trend. Materials fired at around 250 °C form γ-MnO_2 loaded carbons and at 350 °C form Mn_2O_3 loaded materials.

The morphology and particle size were further studied by transmission electron microscopy (see Figure 5.12). The results from the TEM show that the material synthesised at lower temperature has a smaller MnO_x particle size of around 5 to 10 nm. The material synthesised at higher temperature is composed of much larger MnO_x particles of up to 100 nm decorated onto the supporting carbon. These results correlate with the electrochemistry. The best electrochemical performance is obtained from material synthesised at the lower temperature (250 °C), having a smaller, more uniform distribution of catalyst material, higher effective surface area and MnO_2 composition. Figure 5.13 shows the electrochemical performance of the Ketjen Black carbon loaded with MnO_2 by use of a 8 : 1 C to MnO_x mass ratio and fired at 250 °C. The performance is superior to that of any materials studied either based on mass of carbon or based on the total electrode mass.

These results demonstrate the potential benefits of loaded carbons.

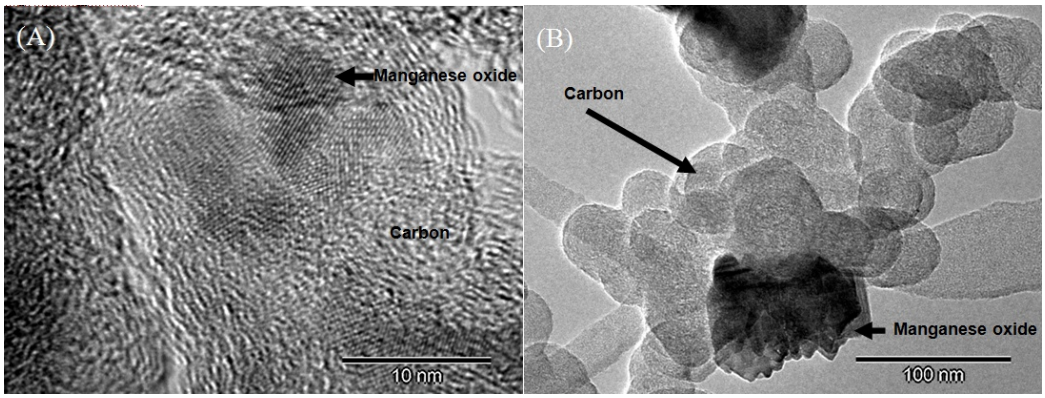

Figure 5.12: (A) TEM images of MnO_x loaded Ketjen Black carbon, 8 : 1 C to MnO_x heated at 250 °C ;(B) TEM images of MnO_x loaded Super P carbon, 8 : 1 C to Mn heated at 350 °C .

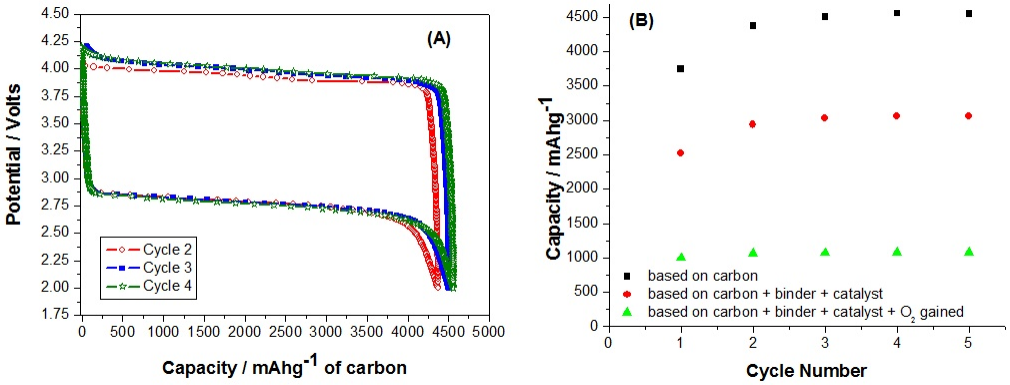

Figure 5.13: (A) Variation of potential with state of charge for a porous electrode containing intimately mixed carbon and catalyst; (B) Variation of discharge capacity with cycle number for porous electrodes, containing carbon loaded MnO_x catalyst, based on carbon, total electrode mass at the beginning (carbon + binder + catalyst) and end (carbon + binder + catalyst + O_2) of discharge.

Further work on this topic is clearly desirable and worthy indeed. Higher surface area carbon material, for example Ketjen Black EC600 with a surface area of $\sim$ 1100 m^2g^{-1} , twice that of normal Ketjen Black 300J and the use of limited capacity cycling to improve cyclability and capacity retention. Effectively reducing the operational potential window by limiting the amount of charge taken and depth of discharge.

References

[1] Débart, A., Paterson, A. J., Bao, J. L., and Bruce, P. G. *Angew. Chem. Int. Ed.* **47**, 4521 (2008).

[2] Débart, A., Bao, J. L., Armstrong, G., and Bruce, P. G. *J. Power Sources* **174**, 1177 (2007).

[3] Wang, J. T. and Savinell, R. F. *Electrochim. Acta* **37**(15), 2737 (1992).

[4] Hang, B. T., Watanabe, T., Eashira, M., Watanabe, I., Okada, S., and Yamaki, J. *Electrochem. Solid-State Lett.* **8**, A476 (2005).

[5] Hang, B. T., Watanabe, T., Eashira, M., Okada, S., Yamaki, J., Hata, S., Yoon, S.-H., and Mochida, I. *J. Power Sources* **150**, 261 (2005).

Chapter 6

Problem of Capacity Fading during Cycling

The rechargeability of the Li/O_2 battery incorporating 1M $LiPF_6$ in propylene carbonate (PC) as the electrolyte has been demonstrated in previous work.[1] Although high capacity has been achieved[2], capacity fading is a feature of all the results.[1,3–5] To investigate the fading problem, a number of experiments have been carried out. A white compound has been found in the cells after cycling. It is probably related to the capacity fading during cycling. It is important to identify the compound and any possible side reactions happened in the system during cycling.

6.1 Identification of the Compound Formed on Cycling

White material has been found on both the anode and cathode sides of the cell after cycling for all the catalysts studied in this work and for all types of carbon. The studied cathode consisting of Super P with α-MnO_2 nanowires was used to investigate this further. The one from anode side was scratched off the Li metal surface in an Ar filled glove box. The quantity of material at the cathode was insufficient to achieve collection and characterization.

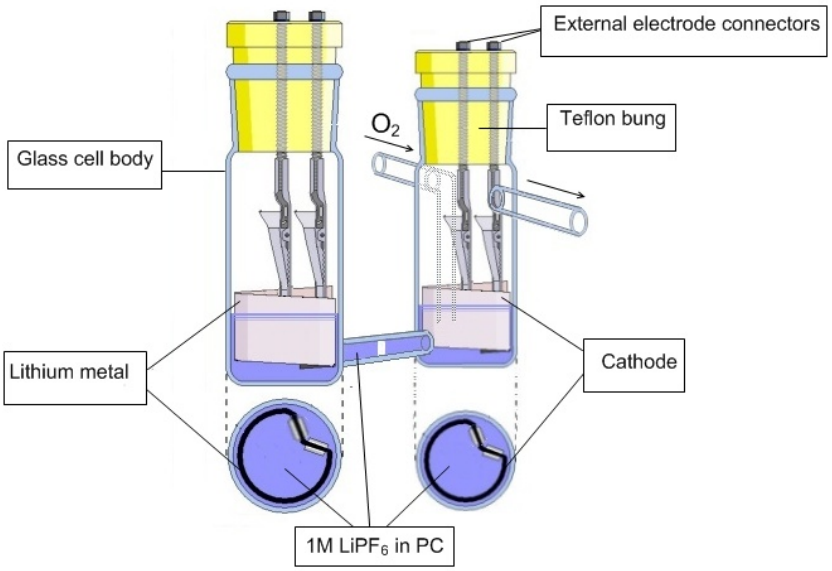

Figure 6.1: Schematic representation of an H-type cell.

To obtain enough material from the cathode for characterization, an H-type cell was employed. As shown in Figure 6.1, the H-cell contains two compartments separating the anode and cathode. The two compartments are connected by the junction which allows the passing of Li ion. The $O_2$was bubbling into the cathode compartment continuously during the whole cycling. After several cycles, the white material in the cathode compartment was obtained by centrifuging the solution from that section of the cell. The material from anode (swagelok cell) and cathode (H-type cell) were analysed by several techniques including XRD, NMR and FT-IR. Experimental details are presented in Chapter 2.

A PXRD pattern of the white material from the cathode is shown in Figure 6.2. Although there are some sharp and intensive peaks in the patterns, it is difficult to assign them to any known phase or mixture of phases we expect, e.g. $LiPF_6$, Li_2CO_3 , Li_2O_2 , possibly of the Li_2O , Li alkylcarbonates, the most of those based on the results of Aurbarch et al. for cathodes up to 4.5 V[6]. However in the cases where PXRD patterns are known, they did not fit the obtained reflections. It is likely to have $LiPF_6$ in the sample. The assignment of all the bands from the infrared spectra for

this white material is reported in Table 6.1. It has proved the presence of PC and $LiPF_6$. ^1H NMR and ^{13}C NMR proved the presence of PC structure. ^{19}F NMR and ^{31}P NMR proved the presence of F^- , PF_6^- and PF_2O^- .

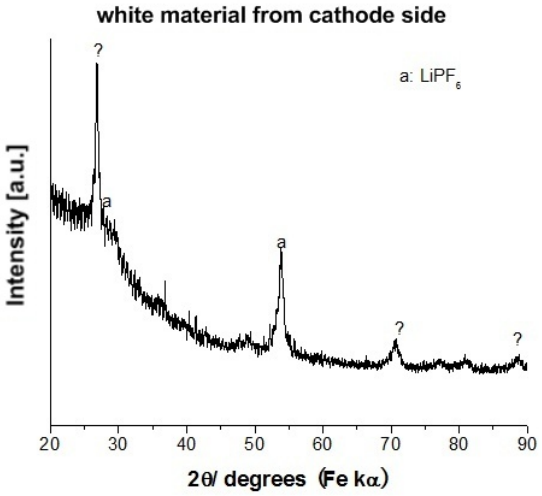

Figure 6.2: XRD patterns of the white material at the cathode in an H-type cell.

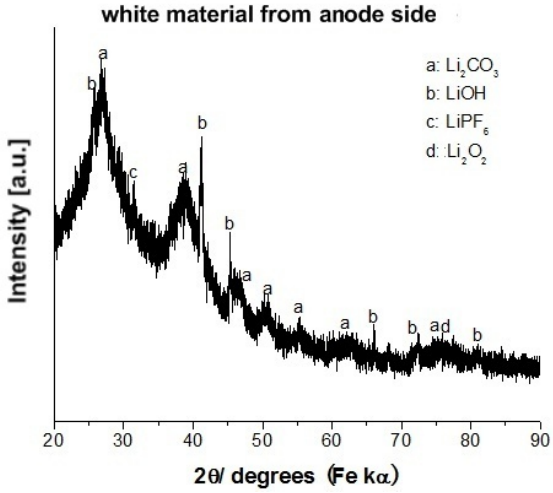

Figure 6.3: XRD patterns of the white material from the anode side.

The PXRD patterns of the white material from the anode are shown in Figure 6.3. Different from the cathode side, most of the peaks can be assigned. Li_2CO_3 and LiOH were confirmed in the sample, and $LiPF_6$ is likely to appear.

Table 6.1: Band assignments of the white material at the cathode (Super P/ α-MnO_2 nanowires) in an H-type cell.

Assignment			
ν observed (cm^{-1})	ν assigned (cm^{-1})	Bands	Compounds
3440	3439/ 3434	Absorbed -OH	
2993	2988		PC
2900-2800	2900-2800		PC
2362	2360	Absorbed CO_2	
1783	1700-1800	C=O stretch	PC
1635	1638		$LiPF_6$
1559	1555	C-C stretch (in ring)	PC
1484	1484	C-C stretch (in ring)	PC
1456	1453	C-C stretch (in ring)	PC
1406	1411		$LiPF_6$
1391	1390	C-H rock	PC
1359	1354	C-H rock	PC
1308	1300-1200	C=O	PC
1262	1270		$LiPF_6$
1205	1300-1200		PC
1161	1160	O-C-O	PC
1123	1120		PC
1075	1075	C-O	PC
$\sim$ 1050	1052		PC
957	953		PC
$\sim$ 915	918		PC
847	848	P-F	$LiPF_6$
$\sim$ 780	776		PC
722	711	Ring bending	PC
559	563	P-F	$LiPF_6$
504	$\sim$ 510		PC
486	492		PC
439	440		PC
414	414		PC

Table 6.2: Band assignments of the white material at the anode (Li).

Assignment			
ν observed (cm^{-1})	ν assigned (cm^{-1})	Bands	Compounds
3676	3676	OH	LiOH
3418	3415	Absorbed -OH	
2973	3000-2800	C-H	RCO_3Li
2936	3000-2800	C-H	RCO_3Li
2852	3000-2800	C-H	RCO_3Li
2362	2360	Absorbed CO_2	
1800	1700-1800	C=O stretch	PC
$\sim$ 1650	1650	C=O, asym	RCO_3Li
1630		vibration of C=O	RCO_3Li
1507	1500-1420	CO_3^{2-} stretching modes $\nu 3$	Li_2CO_3
1441	1500-1420	CO_3^{2-} stretching modes $\nu 1$	Li_2CO_3
1323	1320	C=O, sym	RCO_3Li
1132	1120		PC
1088	1150-1050	C-O	RCO_3Li
$\sim$ 1050	1052		PC
868	870	CO_3^{2-} out of plane deformation $\nu 4$	Li_2CO_3
$\sim$ 850	850	OCO^{2-}	RCO_3Li
738	735		Li_2CO_3 (CO_2 asym)
668			LiOH
500	496		PC
428	434		PC

The assignment of all the bands from the infrared spectra for this material is reported in Table 6.2. The characteristic bands of LiOH, PC, RCO_3Li and Li_2CO_3 are all present. ^{1}H NMR and ^{13}C NMR showed that PC and a structure of the product from the decomposition of PC (opened ring) are present. ^{19}F NMR and ^{31}P NMR gave no signal probably due to the low sensitivity.

6.2 Characterization of the Cathodes After Different Stages of Cycling

From the previous section, white material from cathode side in an H-cell has been collected and analysed. Only $LiPF_6$ and PC were identified by XRD, FT-IR, ^{1}H NMR and ^{13}C NMR in the white material collected from the cathode. It is difficult to conclude that there is no decomposition of PC happened on cathode side. Further experiments were carried out on stored and cycled cathodes from the Li/O_2 cells after treating the electrodes in different ways. The cathode consisting of Super P with α-MnO_2 nanowires was used to investigate this study. Table 6.3 lists the experiments and results from FT-IR and NMR. Based on the results in Table 6.3, a number of reaction mechanisms could be proposed. ^{1}H NMR and ^{13}C NMR confirmed that the ring opened material, i.e. the decomposition products of PC, occurs on the cathodes in all cases.

In experiments No.1-2, two cells were made as usual and rested for 4 weeks in the 30 °C oven without cycling under Ar and O_2 , respectively. The presence of trace polymerised propylene carbonate (PPC) confirmed by FTIR and ring opened material of PC confirmed by ^{1}H NMR and ^{13}C NMR suggests the decomposition of PC even in the cell without applying any current. It indicates the spontaneous reaction happening between the cathode and electrolyte which also has been studied by Ostrovskii et. al.[6] Two unknown peaks might be assigned to CO_2 . It is not clear how the CO_2 appeared on the cathodes, however it might bring out the effect of HF which will be discussed

in the next section. The contaminant brought HF on the cathodes is believed to be water. The presence of $Li_xPO_yF_z$ and LiF in the material from the cell under Ar also indicates the reduction of $LiPF_6$ which might not happen in the case of O_2 .

Experiments No.3-6 studied on the cathodes after half discharge, fully discharge, half charge and fully charge. Li_2CO_3 and trace polymerised PC were identified by FT-IR on the cathode after half discharge, the increasing amount of Li_2CO_3 till the fully discharge was also confirmed by FT-IR according to the increasing peak intensity. On the cathode after half charge, the amount of Li_2CO_3 decreased from the fully discharge and completely disappeared after the fully charge. The possible explanation involved the experimental details. Although the pellet of the mixture of cycled material and KBr powder was prepared in an Ar filled glove box, it has to be exposed to air for a couple of minutes to let the transmitted light through during the test. As discussed in Chapter 4, the major product after discharge is Li_2O_2which can easily react with $CO_2$to form Li_2CO_3. It could not be proved until a gas tight cell is applied. However, if it is the case, there will be one more evidence to prove the reversibility of the formation and decomposition of Li_2O_2 . The presence of trace polymerised PC identified by FTIR and the ring opened material of PC identified by ^{1}H NMR confirms the decomposition of PC happening on the cathode along with the cycling. In experiment No.7, the decomposition products polymerised PC and Li_2CO_3 were identified on the cathode after 8 cycles at the end of charge. Meanwhile, it is interesting to find that most of these decomposition products can be removed by washing with water in experiment No.8.

6.3 Speculating on the Reason of Fading

The white material were formed on both cathode (Super P/α-MnO_2 nanowires) and anode (Li) in the cell. It must involve the reaction of the electrolyte containing solvent and Li salt, which is PC and $LiPF_6$ in this case.

Table 6.3: Experiments and results on stored and cycled cathodes containing α-MnO_2 nanowires as catalyst.

No.	Material	Status	Treatment after cycling	FT-IR results	NMR results
1	α-MnO_2 nanowires+SP	Storing for 4 weeks under Ar	No washing	cast + polymerised PC + $Li_xPO_yF_z$ + LiF + CO_2	PC + ring opened material
2	α-MnO_2 nanowires+SP	Storing for 4 weeks under O_2	No washing	cast + polymerised PC + CO_2 (large amount)	PC + ring opened material
3	α-MnO_2 nanowires+SP	After 1st half discharge	Washed with DMC	Cast + polymerised PC + Li_2CO_3	PC + ring opened material
4	α-MnO_2 nanowires+SP	After 1st discharge	Washed with DMC	Cast + polymerised PC + Li_2CO_3	PC + ring opened material
5	α-MnO_2 nanowires+SP	After 1st half charge	Washed with DMC	Cast + polymerised PC + Li_2CO_3	PC + ring opened material
6	α-MnO_2 nanowires+SP	After 1st charge	Washed with DMC	Cast + polymerised PC	PC + ring opened material
7	α-MnO_2 nanowires+SP	After 8 cycles	Washed with DMC	Cast + polymerised PC + Li_2CO_3	PC + ring opened material
8	α-MnO_2 nanowires+SP	After 8 cycles	Washed with DMC and H_2O	Cast + trace polymerised PC	

Propylene carbonate (PC) has been chosen as the electrolyte solvent for Li and Li-ion batteries because of the low melting point (-49.2 °C), high boiling point (241.7 °C), low viscosity (2.53 mPa · s) and high relative dielectric constant (64.4) for a number of years. It also attracted a lot of attention on the problem it has brought. A few groups discussed the reactions on the cathode side while more others talked about the reactions on anode side which is much more complicated.

$LiPF_6$ is one of the most important and most commonly used salts in Li-ion batteries. It is non-toxic, non-explosive, and highly soluble in nonaqueous solvents, thus forming highly conductive electrolyte solutions. In addition, it is stable with both cathode and anode materials at a wide temperature range. However, $LiPF_6$ salt decomposes to LiF and PF_5 , which is an equilibrium reaction.[7] PF_5 could easily hydrolyse to form HF and PF_3O . Hence, $LiPF_6$ solutions always contain HF. HF reacts with both electrodes and basic surface species to form surface LiF as a major solid product. The possible surface reactions of $LiPF_6$ was proposed by Aurbach.[6]

6.3.1 Cathode

Studies on the reaction of PC between cathode and electrolyte has been doing by a number of groups. It would be useful to review some of the works. The reactions of PC at typical cathodes for Li-ion batteries, $LiNiO_2$, $LiCoO_2$ and $LiMn_2O_4$, have been studied by several groups.[6,8–10] The solid electrolyte interface (SEI) is believed to occur on all such cathodes when PC is present.[9,11] For example, an SEI film is found to form upon contact with $LiMn_2O_4$ and to grow during cycling.[10] It is proposed that nucleophilic attack by the lithiated oxides on the PC to form $ROCO_2Li$ species on the surface of the cathodes.[6] A likely reaction mechanism has been proposed by Aurbach.[6] Thomas et al. proposed the nucleophilic reaction by fluoro anions which comes from the reduction of $LiPF_6$ leading to the ring open. And a polymerization reaction could follow the ring opening to form the polycarbonate.[8] Zhang et al. claimed that depending on the electrode

material, PC can be electrochemically oxidised at potentials as low as 2.1 V vs. Li^+/Li, and the rate of oxidation increases substantially above 3.5 V.[10] The oxidation potential of pure PC is higher than that of PC containing electrolyte salts. In $LiClO_4$ / PC and $LiAsF_6$ / PC system, on heat-treated MnO_2 electrodes, bulk oxidation of the electrolyte takes place above 4.0 V vs. Li^+/Li. CO_2 evolution was observed at low potentials (3.15 and 3.4 V vs. Li^+/Li) depending on the state of charge of the electrodes. No CO_2 was observed in the reverse scan.[12]

Since O_2 was not included in the above cases, reactions on cathodes in a Li/O_2 cell could be different. From the results in the previous sections, it can be proposed that the decomposition of PC happens spontaneously on the cathode in the cell no matter it's under Ar or O_2 during storing even different mechanisms might applied. Under electrochemical conditions, i.e. galvanostatic cycling, the decompositon of PC between cathode and electrolyte also happens along with the whole process. Yet it is not clear what is the nucleophile in this nucleophilic reaction, it is likely related to the intermediate product, superoxide ion, which was identified by the fundamental experiments by Peng et al.[13] Superoxide ion is believed to be superonucleophile and can be an origin of destructive processes initiating by the splitting off of various C-O and C-H bonds. Superoxide ion was produced during discharge, then attacked the ring structure of PC to form the decomposition products, Li_2CO_3 and RCO_3Li .

Efforts also have been made to understand the problem $LiPF_6$ salt might bring. On cathode side, Li_xMO_y active mass might react with trace HF to form the films comprising LiF, which is highly resistive to Li-ion transport. In $LiPF_6$ solutions, the electrodes' impedance is higher due to precipitation of these films. A considerable amount of HF contamination could sufficiently react with carbonate species, solubilise them, and replace them with surface LiF.[14] In Li-ion batteries with different Li salts, $LiMO_2$ cathodes always contain LiF on their surfaces in solutions of $LiPF_6$, $LiBF_4$ and $LiAsF_6$ because of the unavoidably present trace HF. The surface resistance is considerably higher in $LiPF_6$ than in any other salt solution due to the relatively high

concentration of HF in $LiPF_6$ solutions, which means a formation of highly resistive LiF surface films.[6] In the voltammetry study with different systems, a peak around 1.8 V measured with the $LiPF_6$ solution should be attributed to the reduction of the anion (PF_6^-). In $LiPF_6$ / PC solutions, the salt is reduced around 1.8-2 V (vs. Li^+/Li).[15]

By using the H type glass cells, certain amount of white material was obtained from the cathode side. The presence of F^- , PF_6^- and PF_2O^- was shown by ^{19}F NMR and ^{31}P NMR. According to this result, the possible reaction of the degradation of $LiPF_6$ on the cathode in the Li/O_2 battery could be proposed as below. It confirms the influence of trace water in the Li/O_2 battery.

(1) $LiPF_6 \rightarrow LiF + PF_5$;

(2) $PF_5 + H_2O \rightarrow PF_3O + 2HF$;

(3) $PF_3O + 2Li^+ + 2e^- \rightarrow LiPF_2O \downarrow + LiF \downarrow$.

6.3.2 Anode

Considering the white material at the anode, reactions and the interface between PC solvent and Li metal in the Li-ion batteries have been studied for a number of years. The inner part of the SEI layer that forms on Li, contains mainly species of low oxidation states including inorganic Li salts, such as Li_2O , Li_3N , LiX (X=F, Cl, etc.). The outer part,close to the solution, contains species of higher oxidation states and particularly organic Li salts, such as $ROCO_2Li$, ROLi, LiOH, Li_xMF_y (M=As, B, P, etc.), RCOOLi etc.[6,16–18] Surface films on Li in Li-ion batteries are believed to form due to the inevitable reduction of solvent molecules, salt anions, and reactive contaminants at the low potential. They precipitate as a result of a very delicate balance among several competing surface reactions of the various solution components.[6] It is believed that the reaction of solid lithium with PC involves only an one-electron transfer step followed by radical termination reactions.[6,16] The alkyl carbonate solvents are readily reduced at potentials

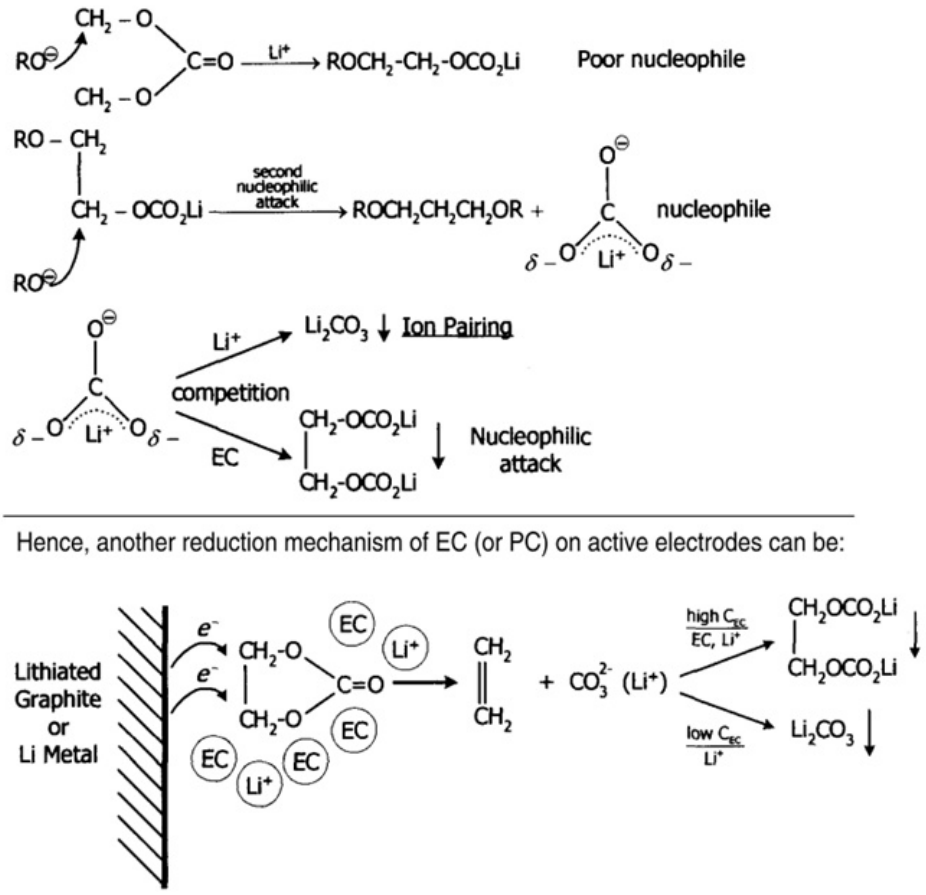

Figure 6.4: EC (PC) reduction mechanisms (nucleophilic paths).[6]

below 1.5 V (vs. Li^+/Li) in the presence of Li-ion.[19,20] The reduction mechanisms of EC (PC) have been proposed by Aurbach, see Figure 6.4.[6] It should be noted that EC is more reactive than PC in electro reduction processes.[21] Aurbach et al. reported the FTIR results in the surface films on lithium in PC solution. The principal components are lithium alkyl carbonates, RCO_3Li, with a number of different R groups possible, including polymeric species.[16] In the potential window 1-0.3 V (vs. Li^+/Li), PC molecules are reduced to $ROCO_2Li$.[15] The freshly deposited lithium covers the active surface area of the Li electrode leading to a loss of the cycleable lithium and consumption of electrolyte because of the highly reactive nature of metallic lithium.[12]

From the anode in a Li/O_2cell, PC, polymerised PC, RCO_3Li, $Li_2CO_3$and

LiOH were identified by XRD, FT-IR or NMR. The decomposition of PC on Li metal was confirmed and the reaction mechanism could be similar as discussed above.

From the published work on Li-ion batteries, on Li side, $LiPF_6$ will first react with lithium leading to the LiF formation on the inner interface, then followed by EC (PC) to form other inorganic and organic even polymer phases as the SEI grow thicker.[22] From the study of different Li salts, it is found that the salt anion determines the formation of the interface, the morphology and Li cycling efficiency. $LiAsF_6$ turned out to be a promising Li salt for Li-ion batteries because of the less reactivity to lithium than $LiPF_6$.[17] This is in accord with the results in Chapter 5. No evidence of the degradation of $LiPF_6$ were found by current techniques on the anode in the Li/O_2 battery, it might suggest that $LiPF_6$ is more stable between the Li metal and electrolyte in the Li/O_2 cell because of the high cycling voltage.

6.3.3 Attempt to Recover the Cycleability

Considering the reaction of the electrolyte on both cathode and anode in the Li/O_2 cell, a number of experiments were carried out trying to recover the cycleability and figure out the key factor causing the capacity fading. Some standard Li/O_2 cells were made up and galvanostatic cycled for several cycles until the capacity dropped. Each cell was then treated by different ways and recycled under the same conditions. Table 6.4 lists the details of each experiment and the results of recycling.

Only one of the experiments, experiment No. 8 succeeded in recovering the capacities for several cycles. In this experiment, the cathode after pre-cycling was washed with distilled water for 3 times and dried in the vacuum oven at 80 °Cfor 6 days. Then a new cell was made using this washed cathode. The initial capacity was slightly lower than the previous one, however this capacity was maintained for more than 10 cycles. It suggests that both the reaction between cathode and electrolyte and the reaction between anode and electrolyte affected the electrochemical performance. Replacing cathode

Table 6.4: Attempt to recover the cycleability

No.	Experimental Detals	Results
1	Rest for 54 hrs	No recovery
2	Refill the O_2 for 30 minutes	No recovery
3	Use new electrolyte (change the separators and put new electrolytes)	No recovery
4	Use new Li metal	No recovery
5	Use new Li metal and new electrolyte	No recovery
6	Use new cathode	No recovery
7	Make a new cell with the old cathode washed with DMC	No recovery
8	Make a new cell with the old cathode washed with distilled water	Recovered capacities for more than 10 cycles

or anode did not recover the cycling at all. It also revealed that most of the decomposed products can be washed out by the distilled water.

6.4 Dehydration of the Catalyst to Improve the Cycleability

Consider that the O_2 electrode relies on a catalytic reduction and that the surfaces of most oxides prepared in here contain H_2O to a certain extent (Figure 6.7). It is interesting to examine the influence of dehydrating the surfaces on the electrode behavior.

Dehydration treatment has been applied on different as-prepared catalyst materials, including Co_3O_4 (mesoporous), NiO (mesoporous) and CuO (bulk, nanosized and mesoporous). The bulk CuO was purchased from Aldrich (99+ %), the nanoparticulate CuO and mesoporous catalysts were prepared using the methods discussed in Chapter 2. The CuO nanorods

and nanowires were prepared using the methods from the previous work.[23] The as-prepared catalyst materials were heated under various atmosphere at the rate of 2 °C /min to 250 °C and kept at 250 °C for 2 h. The dehydrated materials heated under air were made to the slurry and casted under air right after the dehydration. The materials dehydrated under other atmosphere were transfered into an Ar filled glove box and made to a slurry then casted in the glove box without exposing to air. The dehydrated materials were characterised using a variety of techniques. Powder X-ray diffraction was carried out using a stoe STADI/P powder diffractometer, the morphologies were characterised by transmission electron microscopy using a JEOL JEM-2011. Surface area measurements and porosity were determined by aqueous N_2 absorption- desorption using the BET method and a Hiden IGA porosimeter. Each dehydrated material was used as the catalyst of the cathode in a Li/O_2 cell for galvanostatic cycling.

Figure 6.5 presents the XRD patterns of the dehydrated materials obtained from various atmosphere. The powder patterns of the dehydrated mesoporous Co_3O_4 and mesoporous NiO are consistent with the ones of the mesoporous Co_3O_4 and mesoporous NiO, respectively (Figure 6.5A and B). Cu_2O was obtained when dehydrate the CuO nanoparticles under N_2 while all the other CuO materials remained the same phase after dehydration treatment, see Figure 6.5C. It is confirmed by TEM that most of the morphology has been maintained after dehydration for all the cases, see Figure 6.6. And it's for sure that all the dehydration treatments are accompanied by sacrificing of the surface area. The TG-MS measurements on mesoporous CuO show the similar results under various atmosphere and H_2O was found to be the main product after heating, see Figure 6.7. Some of the details will be discussed below.

Figure 6.8 compares the performances of the electrodes containing the dehydrated and nondehydrated mesoporous materials. The distinct improvement in electrochemical performance in terms of higher reversible capacity and better capacity retention was observed. By dehydration, even with sacrificing part of the surface area, better capacity retention can be

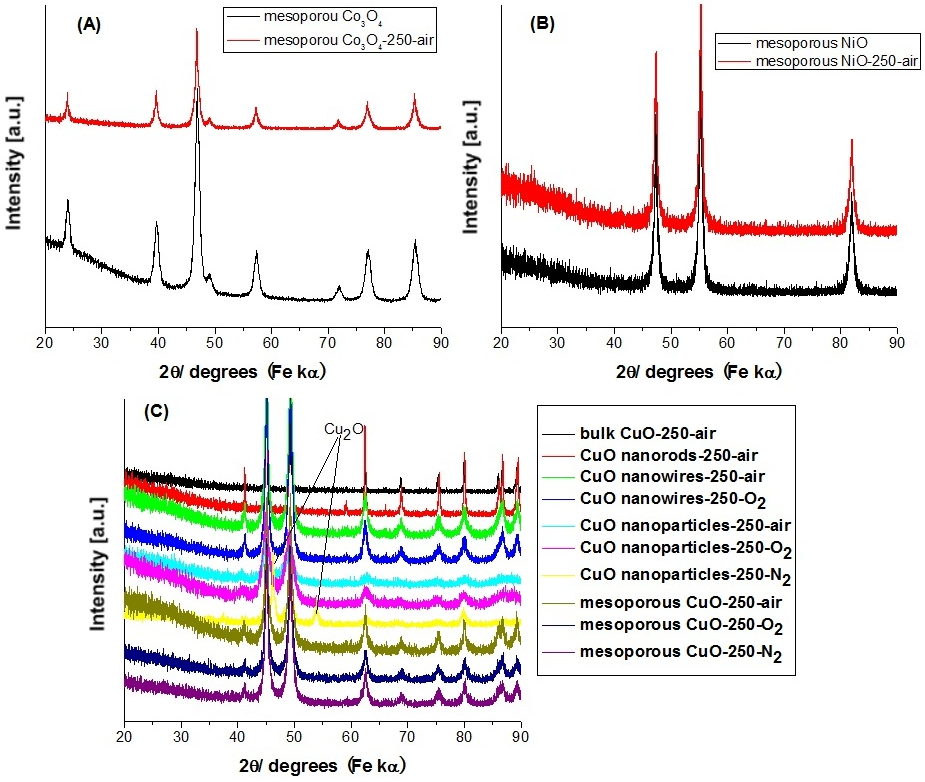

Figure 6.5: XRD patterns of different dehydrated catalyst materials under various atmosphere including: (A) Co_3O_4 , (B) NiO and (C) CuO.

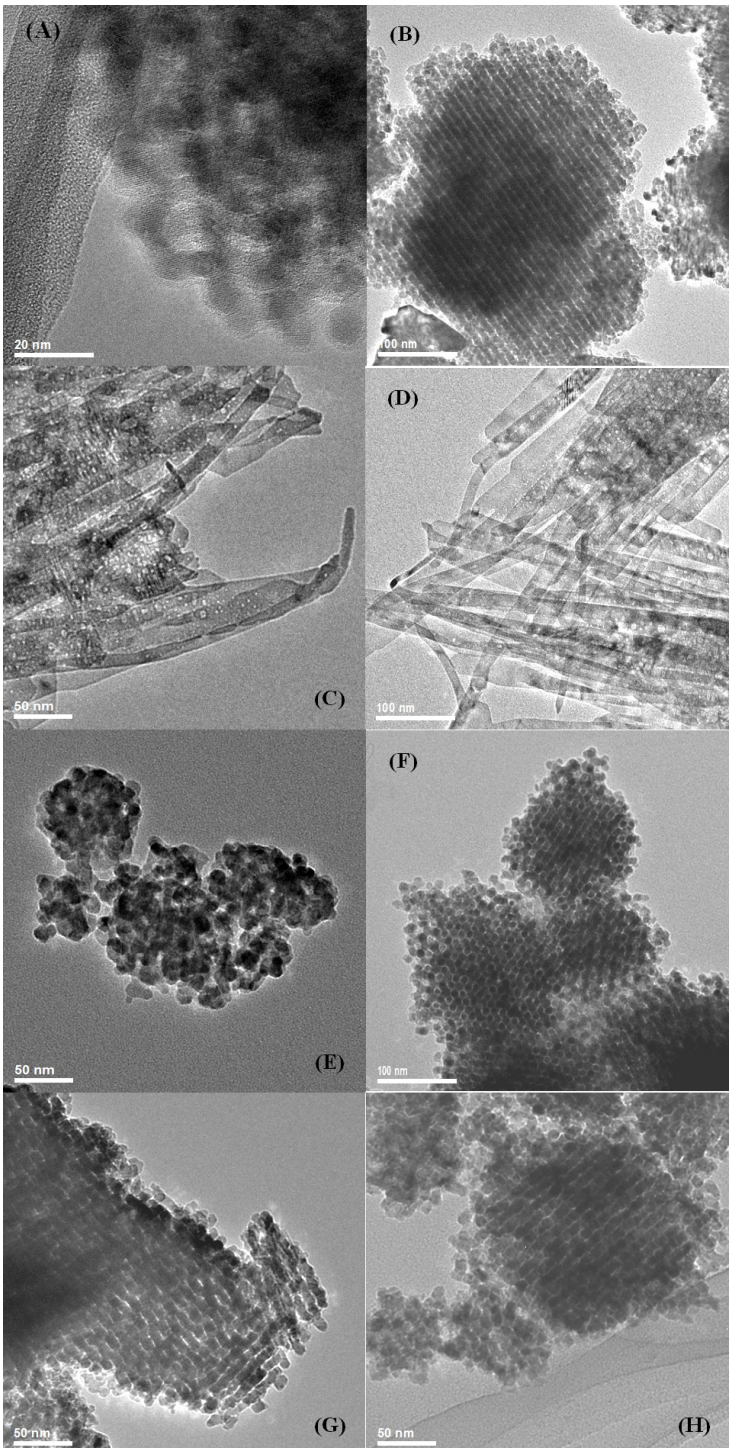

Figure 6.6: TEM images of different dehydrated catalyst materials under various atmosphere: (A) mesoporous Co_3O_4 -250-air; (B) mesoporous NiO-250-air; (C) CuO nanowires-250-air; (D) CuO nanowires-250-O_2 ; (E) CuO nanoparticles-250-air; (F) mesoporous CuO-250-air; (G) mesoporous CuO-250-O_2 ; and (H) mesoporous CuO-250-N_2 .

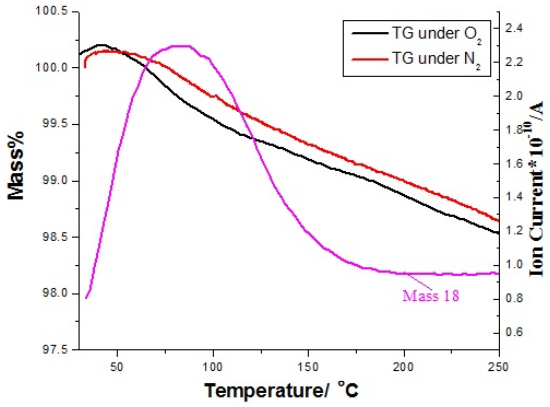

Figure 6.7: TG-MS of mesoporous CuO heated under different atmosphere including N_2 and O_2 , 5.0K/min from 30 °C to 250 °C .

obtained. It could be related to the high surface area. The as-prepared mesoporous Co_3O_4 and mesoporous NiO have the surface areas of 130.5 m^2g^{-1} and 93 m^2g^{-1} , respectively, before dehydrating. It might be because the H_2O absorbed on the surface or in the pores has been removed by dehydration. It could be one of the evidences of the H_2O influence on the battery cycling performance, see previous sections.

Figure 6.9 presents the electrochemical performances of bulk CuO and CuO nanorods, respectively. The materials before dehydrating have the surface areas of 0.023 m^2g^{-1} and 0.6 m^2g^{-1} , respectively. Obviously, the dehydration didn't improve any of the performances, the aggregation and loss of the surface area led to the inferior performance to that of the nondehydrated materials on bulk materials with low surface area. It may suggest, by the comparison above, that only the performance of the materials with high surface area can be improved by the dehydration treatment.

If the removing of H_2O is the only reason for the performance improvement, the performance should be further improved by dehydrating under the atmosphere with lower moisture. Dehydration treatments have been applied on CuO nanoparticles and mesoporous CuO under different atmosphere including air, O_2 and N_2 . The electrochemical performances are shown in Figure 6.10. And it's surprising to find the results were unexpected. In the

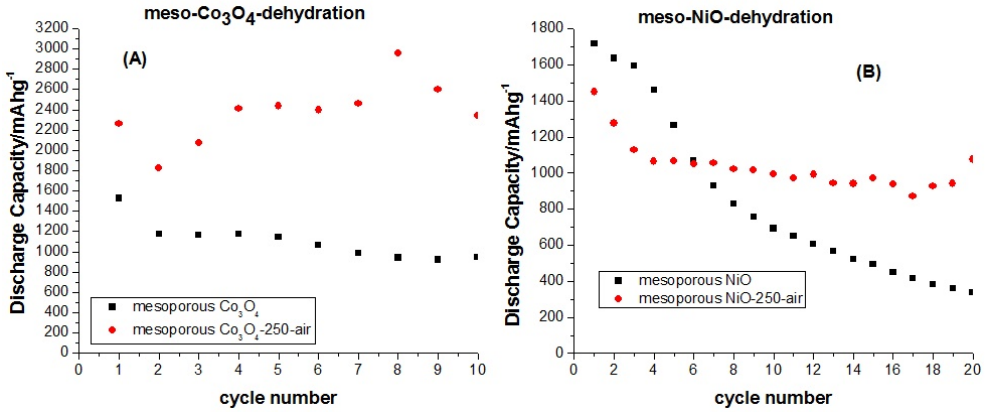

Figure 6.8: Variation of discharge capacity with cycle number for porous electrodes before and after dehydration under air containing different catalysts including: (A) mesoporous Co_3O_4 and (B) mesoporous NiO.

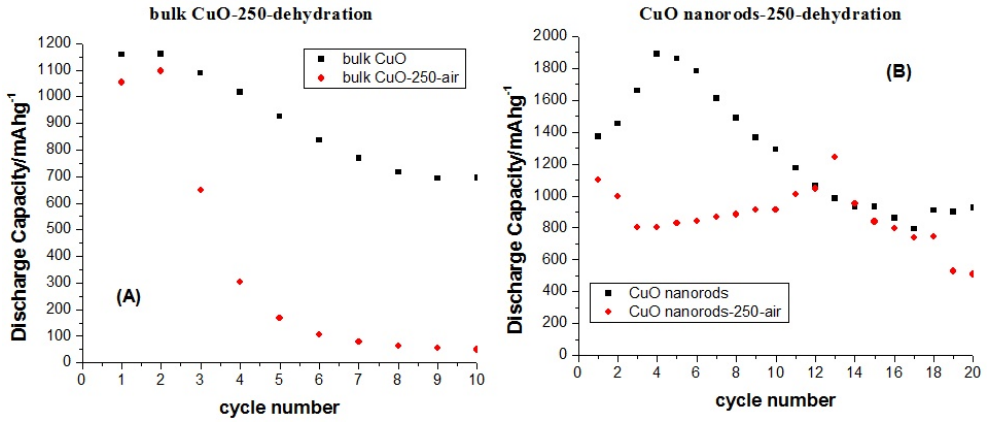

Figure 6.9: Variation of discharge capacity with cycle number for porous electrodes before and after dehydration under air containing different catalysts including: (A) bulk CuO and (B) CuO nanorods.

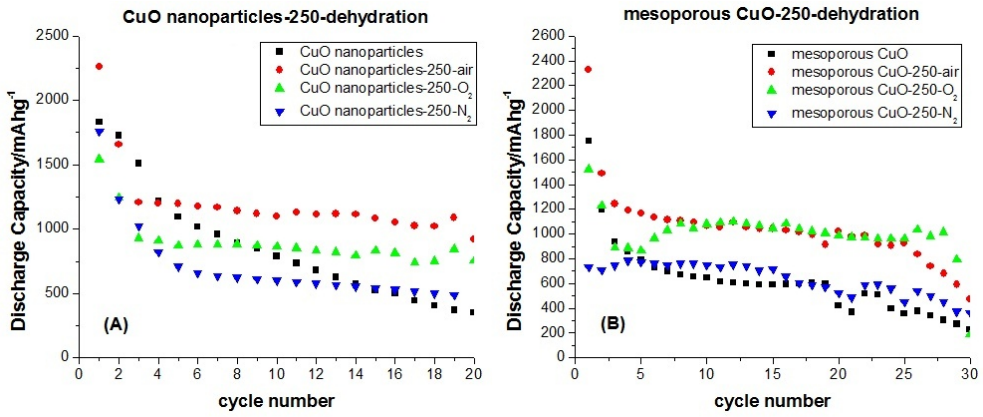

Figure 6.10: Variation of discharge capacity with cycle number for porous electrodes before and after dehydration under various atmosphere containing different catalysts including: (A) CuO nanoparticles and (B) mesoporous CuO.

case of CuO nanoparticles, Figure 6.10A, the electrochemical performances of the dehydrated materials show the following trend from best to worst obtained from different atmosphere: air $>$ O_2 $>$ N_2 . All the cases show better capacity retention than the nondehydrated material although only the materials obtained from air and O_2 improved the performances. The appearance of Cu_2O could be one of reasons for the inferior performance. It attracted the attention on the surface reactions of the material, not just the removing of H_2O .

A possible explanation is discussed below. Material with high surface area has more structure defects on the surface and in the pores, it can absorb much H_2O than the material with low surface area. Dehydration treatment under air and O_2 can remove the H_2O from the surface and pores, the defects then could be occupied by O_2 molecules. The O_2 on the surface of the oxide catalyst may participate in the electrode reaction which could improve the performance by avoiding the fading problem and increasing the reversible capacity. This might explain the superior performance of the materials from air and O_2 to that of the materials from N_2 . The surface of the material dehydrated under air might also absorb trace CO_2 molecules which could form Li_2CO_3 on the surface of the electrode before the formation of LiF during cycling so that protect the electrode. This might be the reason of the

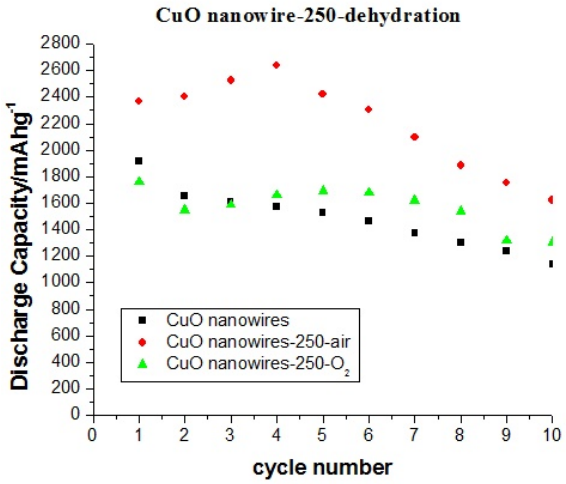

Figure 6.11: Variation of discharge capacity with cycle number for porous electrodes before and after dehydration under various atmosphere containing CuO nanowires as catalyst.

superior performance of the material from air to that of the material from O_2 . Similar trend was also shown in the performance of CuO nanowires, see Figure 6.11.

In the case of the mesoporous CuO, see Figure 6.10B, the electrochemical performances show the following trend from best to worst obtained from different atmosphere: air $\approx O_2 > N_2$. It might be because of the special structure of the mesoporous materials. For the mesoporous materials, most surface area is in the mesopores which might be difficult to be occupied by CO_2 molecules, therefore the materials dehydrated under air and O_2 show similar performances. It should be noted that after dehydration the mesoporous material actually got more capacity increasing than the nanoparticulate material did. This could be explained by the different surface area loss. For example, after dehydration treatment under air, the surface area of mesoporous CuO decreased from 63.8 m^2g^{-1} to 44.4 m^2g^{-1} , while the surface area of nanoparticulate CuO decreased from 103.4 m^2g^{-1} to 38.8 m^2g^{-1} . Meanwhile, it is found that before and after dehydration treatment, the mesoporous CuO show the similar good capacity retention, which suggests the mesoporous CuO could be a good catalyst material for the Li/O_2 battery.

6.5 Conclusion

In summary, there are some processes which are known to lead to the capacity fading in Li-ion batteries: lithium deposition (overcharge conditions); electrolyte decomposition; active material dissolution; phase changes in the insertion electrode materials; and passive film formation over the electrode and current collector surfaces. In the case of non-aqueous Li/O_2 battery, evidence of the capacity fading problem has been revealed by different means. Polymerised PC, Li_2CO_3 , F^- , PF_6^- and PF_2O^- were found on the cathode while LiOH, PC, RCO_3Li and Li_2CO_3 were found on the anode. It suggests the decomposition of PC on both cathode and anode although the mechanism are likely different. Also the degradation of $LiPF_6$ was confirmed on cathode. These could be the key of the capacity fading. More work need to be done to address the mechanism. Considering that the mesoporous materials have high surface area which can absorb much water on the surface and in the pores, the dehydration treatment has been applied on some of the mesoporous materials. The materials after dehydration as the catalyst of the O_2 electrode in a non-aqueous Li/O_2 cell do show better capacity retention and higher reversible capacity. TG-MS results confirm that H_2O is the main product during heating. It suggests that the water absorbed on the material does affect the performance of the cell. Again more work need to be done to address the mechanism.

References

[1] Ogasawara, T., Débart, A., Holzapfel, M., Novak, P., and Bruce, P. G. *J. Am. Chem. Soc.* **128**, 1390 (2006).

[2] Débart, A., Paterson, A. J., Bao, J. L., and Bruce, P. G. *Angew. Chem. Int. Ed.* **47**, 4521 (2008).

[3] Abraham, K. M. and Jiang, Z. *J. Electrochem. Soc.* **143**, 1 (1996).

[4] Read, J. *J. Electrochem. Soc.* **149**, A1190 (2002).

[5] Débart, A., Bao, J. L., Armstrong, G., and Bruce, P. G. *J. Power Sources* **174**, 1177 (2007).

[6] Schalkwijk, W. A. V. and Scrosati, B. *Advances in Lithium-ion Batteries*. Kluwer Academic, (2002).

[7] Sloop, S. E., Pugh, J. K., Wang, S., Kerr, J. B., and Kinoshita, K. *Electrochem. Solid-State Lett.* **4**, A42 (2001).

[8] Eriksson, T., Andersson, A. M., Bishop, A. G., Gejke, C., Gustafsson, T., and Thomas, J. O. *J. Electrochem. Soc.* **149**, A69 (2002).

[9] Wursig, A., Buqa, H., Holzapfel, M., Krumeich, F., and Novak, P. *Electrochem. Solid-State Lett.* **8**, A34 (2005).

[10] Zhang, S. S., Xu, K., and Jow, T. R. *J. Electrochem. Soc.* **149**, A1521 (2002).

[11] Sloop, S. E., Kerr, J. B., and Kinoshita, K. *J. Power Sources* **119-121**, 330 (2003).

[12] Arora, P., White, R. E., and Doyle, M. *J. Electrochem. Soc.* **145**, 3647 (1998).

[13] Peng, Z. Q. and Bruce, P. G. *paper's in preparation* .

[14] Aurbach, D., Gamolsky, K., Markovsky, B., Salitra, G., Gofer, Y., Heider, U., Oesten, R., and Schmidt, M. *J. Electrochem. Soc.* **147**, 1322 (2000).

[15] Aurbach, D., Levi, M. D., Levi, E., and Schechter, A. *J. Phys. Chem. B* **101**, 2195 (1997).

[16] Aurbach, D., Daroux, M. L., Faguy, P. W., and Yeager, E. *J. Electrochem. Soc.* **134**, 1611 (1987).

[17] Aurbach, D., Markovsky, B., Weissman, I., Levi, E., and Ein-Eli, Y. *Electrochim. Acta* **45**, 67 (1999).

[18] Aurbach, D. *J. Power Sources* **89**, 206 (2000).

[19] Aurbach, D., Daroux, M. L., Faguy, P., and Yeager, E. *J. Electroanal. Chem.* **297**, 225 (1991).

[20] Aurbach, D., Moshkovich, M., and Gofer, Y. *J. Electrochem. Soc.* **148**, E155 (2001).

[21] Aurbach, D., Gofer, Y., Ben-Zion, M., and Aped, P. *J. Electroanal. Chem.* **339**, 451 (1992).

[22] Yazami, R. *Electrochim. Acta* **45**, 87 (1999).

[23] Gao, X. P., Bao, J. L., Pan, G. L., Zhu, H. Y., Huang, P. X., Wu, F., and Song, D. Y. *J. Phys. Chem. B* **108**, 5547 (2004).

Chapter 7

Electrochemical properties of mesoporous α-Fe_2O_3

7.1 Introduction

The electrochemical reduction of MO_x 3d-metal oxides (M = Mn, Co, Fe, Ni, Cu) in lithium cells have been studied for a number of years. Tarascon and co-workers reinvestigated the reactivity of lithium with transition metal oxides and found that the process could be reversible. The electrochemical reaction of Li with CoO, CuO, NiO, Co_3O_4 and MnO was shown to lead to composite materials consisting of nanometer-scale metallic clusters dispersed in an amorphous Li_2O matrix. The reversibility has been attributed to the nanocomposite nature of these electrodes, which have been termed conversion reactions, although there is irreversibility in the first cycle.[1]

Iron oxides represent a particularly important class of materials in a wide range of applications.[2–9] They combine such functionality with low cost and low toxicity. Work on the reactivity of macroscale versus nanoscale haematite (α-Fe_2O_3) particles with lithium suggested that the nanoscale may radically change the chemical/ electrochemical reaction. Large particles in the micrometric range (0.5 μm, 2 m^2g^{-1}) undergo an irreversible transformation of the close-packed anionic array from hexagonal (α-Fe_2O_3)

to disordered cubic stacking ($Li_2Fe_2O_3$) as soon as a very small amount of lithium (x_c = 0.03 Li/Fe_2O_3) is inserted in the corundum structure. However, when the particle size is reduced to about 20 nm (60 m^2g^{-1}), Fe_2O_3 nanoparticles can reversibly and topotactically react with up to 1 Li per formula unit without phase transformation.[2,10,11]

Jiao et al. reported the preparation and interesting properties of mesoporous iron oxides with ordered and disordered walls prepared using KIT-6 silica as a hard template.[12] In the present work, the electrochemical properties of mesoporous α-Fe_2O_3 with ordered walls, mesoporous α-Fe_2O_3 with disordered walls, and Fe_2O_3 nanoparticles were studied. Both the surface area and degree of crystallinity affect the electrochemical properties of the materials. Although the more crystallised samples show better performance, the mesoporous morphology does not lead to high rate capability or good capacity retention on cycling.

7.2 Experimental

Nanoparticulate α-Fe_2O_3 (∼25 nm) was synthesised using a procedure reported by Tarascon et al. (see 2.1.3).[2,10] Mesoporous α-Fe_2O_3 with ordered and disordered walls were synthesised using a procedure reported by Jiao et al. (see 2.1.2).[12]

Electrochemical cells were constructed by mixing the active material, Kynar 2801 (a co-polymer based on polyvinylidene fluoride), and Super S carbon (MMM) in the weight ratio of 80 : 10 : 10. The mixture was cast onto copper (or aluminum) foil from acetone using a Doctor-Blade technique. After solvent evaporation at room temperature and heating at 80 °C under vacuum for 8 hours, the foil was cut into 13 mm diameter disks. The electrodes were assembled into Swagelok cells with a Li anode and LP 30 electrolyte (Merck; 1M $LiPF_6$ in 1 : 1 v/v ethylene carbonate : dimethyl carbonate). The typical mass of active material in each cell was ∼11 mg. The cells were constructed and handled in an Ar-filled MBraun glove box.

Electrochemical measurements were carried out using a MACCOR 4200 system.

7.3 Results and Discussion

The XRD patterns of the as-prepared samples are shown in Figure 7.1. All peaks in the patterns of the three samples are consistent with the JCPDS (33-664) data of the α-iron oxide. Peaks of disordered mesoporous Fe_2O_3 are weak and broad compared with those from the other two samples. It indicates the walls of disordered sample are not amorphous but contain small crystallites. And peaks of the ordered mesoporous sample are broader than those for the nanoparticles, suggesting that the former consists of much finer domains.

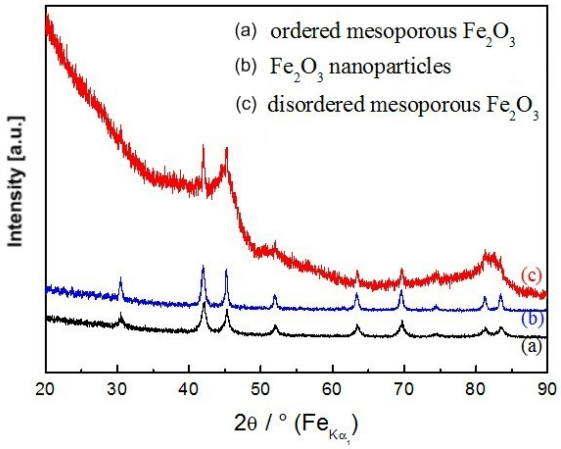

Figure 7.1: XRD patterns of mesoporous α-Fe_2O_3 with ordered walls, Fe_2O_3 nanoparticles and mesoporous α-Fe_2O_3 with disordered walls.

Transmission electron micrographs (TEM) of the three samples are shown in Figure 7.2. The first two images show that the α-Fe_2O_3 particles with ordered or disordered walls exhibit an ordered mesoporous structure. α-Fe_2O_3 nanoparticles show the similar lozenge-shape and particle size to the ones in Tarascon's publication.[2,10]

The materials were examined by nitrogen adsorption-desorption measurements and the BET values of the surface areas were decided. The values were

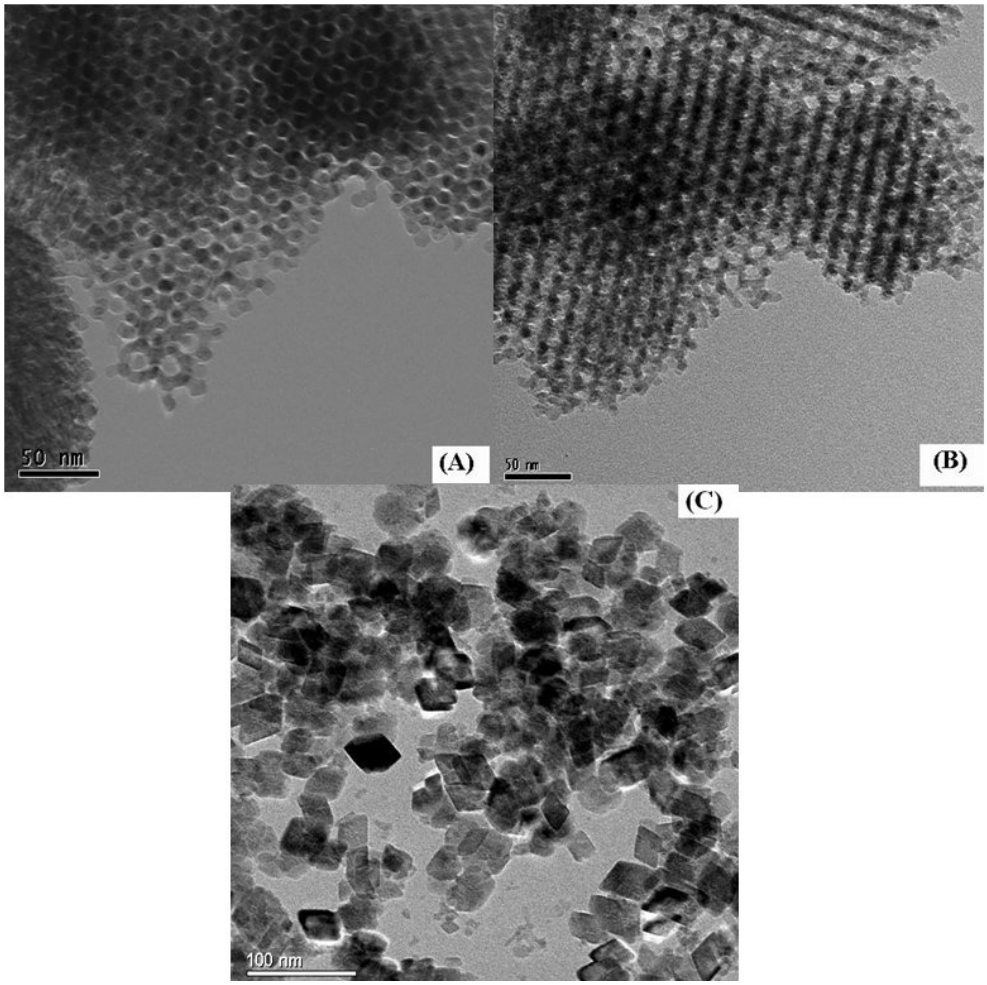

Figure 7.2: TEM images of: (A) mesoporous α-Fe_2O_3 with ordered walls; (B) mesoporous α-Fe_2O_3 with disordered walls; (C) α-Fe_2O_3 nanoparticles.

139 and 210 m^2g^{-1} for the mesoporous α-Fe_2O_3 with ordered and disordered walls, respectively. For α-Fe_2O_3 nanoparticles the BET surface area was 72 m^2g^{-1} .

Evidently, the surface areas of the mesostructured α-Fe_2O_3 are significantly larger than that of the nanoparticles.

To investigate the electrochemical properties of the samples with different structures, all three samples were used as the active materials in cathodes in Li-ion cells. Figure 7.3 shows the electrochemical performance of these samples cycled between 0.01 and 3 V at a discharge and charge rate of

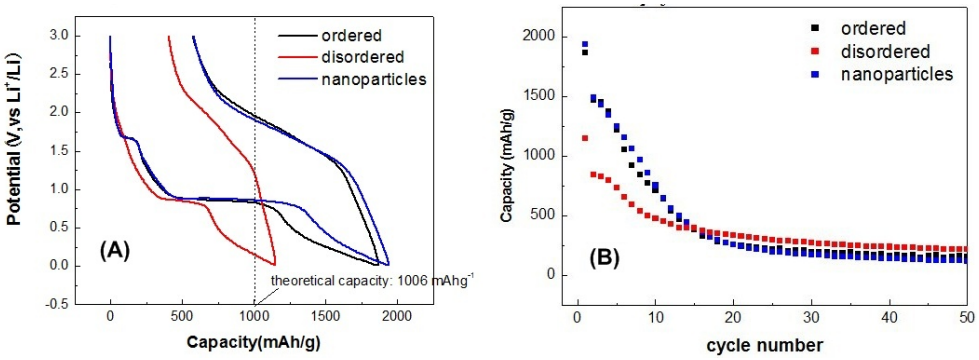

Figure 7.3: (A) Variation of potential with state-of-charge for the first discharge then charge for a composite electrode composed of different Fe_2O_3 with Super S carbon and Kynar, weight ratios 80 : 10 : 10, at a rate of 100 mAg^{-1} . (B) Variation of discharge capacity with cycle number at 100 mAg^{-1} between 0.01-3 V.

100 mAg^{-1} .

They all gave a large first discharge capacity, which exceeded the theoretical capacity basing on a complete reduction of Fe^{3+} to Fe^0 (1006 $mAhg^{-1}$). Tarascon and co-workers claim that the excess capacity can be regarded as originating from the low-voltage decomposition of the electrolyte and subsequent formation of an organic layer deposited on the surface of the particles that occurs below 0.8 V.[2,10] The plateau at ∼0.8 V is accorded to the conversion reaction $6Li+Fe_2O_3 \rightarrow 2Fe+3Li_2O$. There is good evidence for this process in their recent papers.[13,14] However, an alternative mechanism indicating extra charge storage at the interface between the nanoparticles in composite has been proposed by Maier et al.[15] Both mechanisms may quote here. There is good evidence for a polymer layer in the TEM images, see Figure 7.4, and this is expected to form below 0.8 V. Selected area electron diffraction (SAED) of the nanoparticulate and mesoporous Fe_2O_3 with ordered walls exhibits single-crystalline diffraction patterns, whereas the SAED pattern of the disordered Fe_2O_3 shows several diffraction rings. It is likely that the walls of the disordered Fe_2O_3 are composed of α-Fe_2O_3 nanocrystallites. The similar capacity of ordered mesoporous and nanoparticulate α-Fe_2O_3 may correlate with both being single crystal while the disordered mesoporous α-Fe_2O_3 has a different structure. However, why

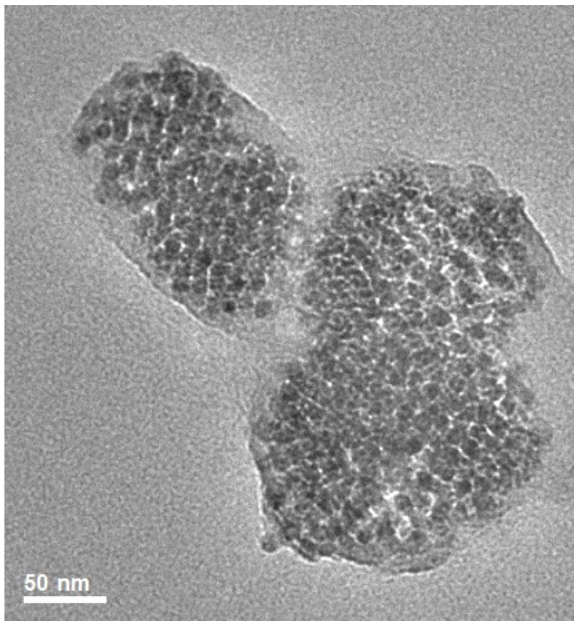

Figure 7.4: The TEM for ordered mesoporous Fe_2O_3 after 1st cycle between 0.01-3 V.

they showed distinctly different capacity for the conversion reaction and extra capacity is not clear. All samples exhibited a large capacity loss towards the 20^{th} cycle. This suggests that the crystalline structure of the electrode materials changes on cycling.[2,10,16]

Figure 7.5 shows the PXRD patterns of the samples discharged to 0.01 V. All three samples show similar results. Besides the unreacted α-Fe_2O_3 , peaks belonging to Fe metal and Li_2O were observed in the patterns for all three samples. The results confirm the reduction of Fe^{3+} to Fe^0 .

The main difference between the three samples arises before the plateau around 0.8 V (Figure 7.3). The plateau at 1.7 V is evident for the ordered mesoporous α-Fe_2O_3 and α-Fe_2O_3 nanoparticles but not for the disordered mesoporous sample. The high voltage region has been examined by discharging to a cut-off voltage of 1.55 V. The variation of voltage with state-of-charge (Li content) is shown in Figure 7.6. The plateaus for the ordered mesoporous and nanoparticulate α-Fe_2O_3 are confirmed as is the sloping discharge for the disordered mesoporous sample.

Galvanostatic intermittent titration technique (GITT) experiments were

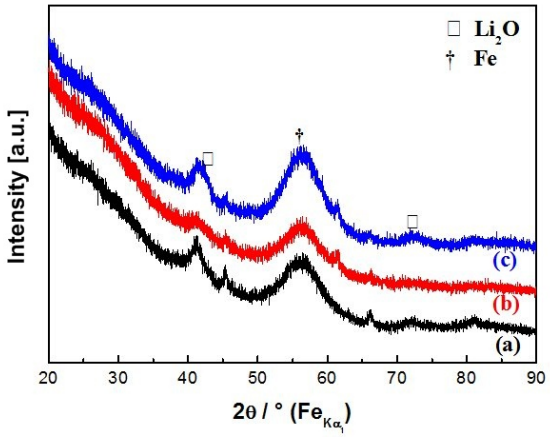

Figure 7.5: XRD patterns of the samples after 1st discharge to 0.01 V: (a) mesoporous α-Fe_2O_3 with ordered walls; (b) mesoporous α-Fe_2O_3 with disordered walls; (c) Fe_2O_3 nanoparticles.

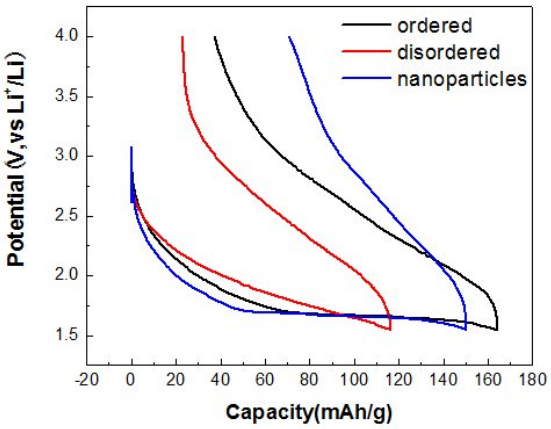

Figure 7.6: Variation of potential with state-of-charge (Li content) for the first discharge then charge for a composite electrode composed of different Fe_2O_3 with Super S carbon and Kynar, weight ratios 80 : 10 : 10, at a rate of 100 mAg^{-1} between 1.55 and 4 V.

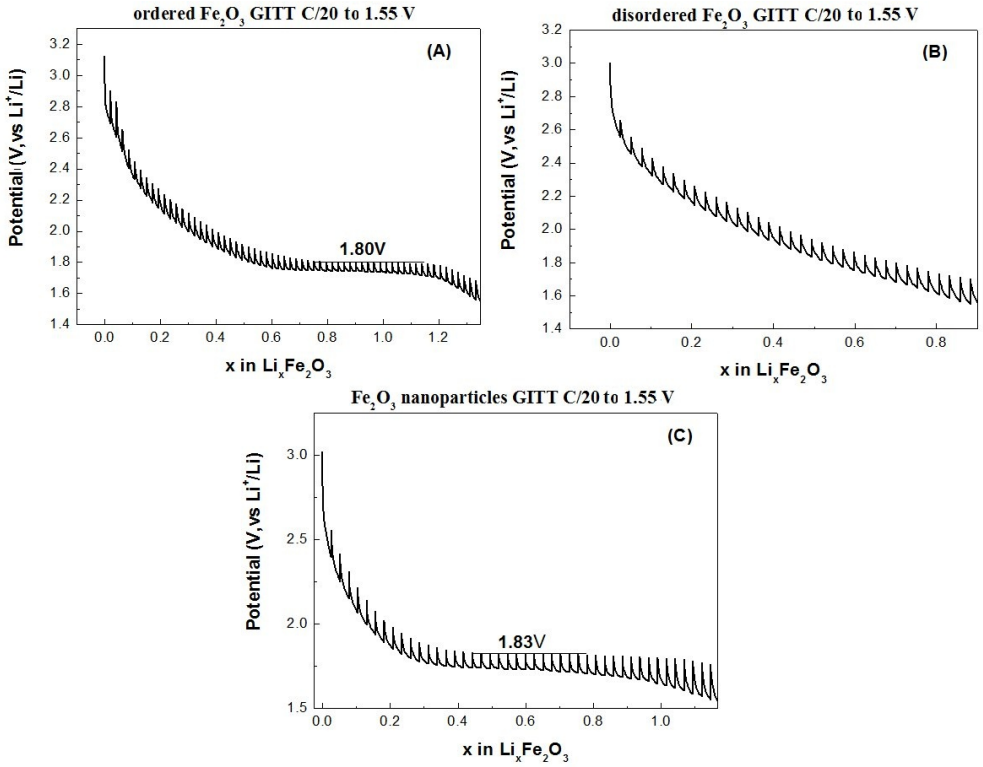

Figure 7.7: Voltage-composition curves in GITT mode for: (A) mesoporous α-Fe_2O_3 with ordered walls; (B) mesoporous α-Fe_2O_3 with disordered walls; (C) Fe_2O_3 nanoparticles, at the rate of C/20 with the ending voltage of 1.55 V.

performed to determine the quasi-equilibrium open-circuit potential, the results are shown in Figure 7.7. These data are consistent with the load curves in Figure 7.6. According to Tarascon [2,10], in the monophasic process, lithium ions are inserted into the structure without any phase transformation. In contrast, the well-known transformation of the close-packed anionic array from hexagonal (hcp) to cubic (ccp) stacking happens in the biphasic process.[17] This is confirmed by the XRD patterns in Figure 7.8. After discharge, there is no evidence of a phase transformation occurring in the case of the disordered α-Fe_2O_3 , while a cubic Li-Fe-O phase was found in the patterns of the other two samples.[17] It is known from numerous work e.g. $LiFePO_4$ that as crystallite size decreases two phase reactions can become single phase. The two phase process then is relieving total strain in solid solution. As crystallite size decreases strain decreases and single phase reactions are growing. This probably explains why the nanodomain (disordered) α-Fe_2O_3 is monophasic, whereas the ordered mesoporous and nanoparticulate α-Fe_2O_3 are biphasic. From Figure 7.8B, it is found that after several cycles, the intensity of the peaks belonging to $Li_2Fe_2O_3$increased, which means the proportion of $Li_2Fe_2O_3$ increases as well.

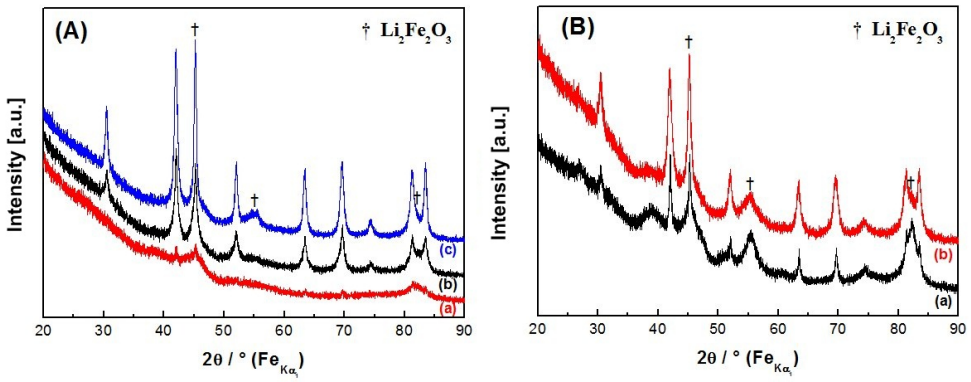

Figure 7.8: (A)XRD patterns of the samples after 1st discharge to 1.55 V and (B) after 50th cycle. Part (A) includes: (a) mesoporous α-Fe_2O_3 with disordered walls; (b) mesoporous α-Fe_2O_3 with ordered walls; and (c) Fe_2O_3 nanoparticles, part (B) includes: (a) mesoporous α-Fe_2O_3 with ordered walls and (b) Fe_2O_3 nanoparticles.

In Figure 7.7, the x values indicate the number of inserted lithiums per formula unit. The x value (x in $Li_xFe_2O_3$) for the nanoparticulate

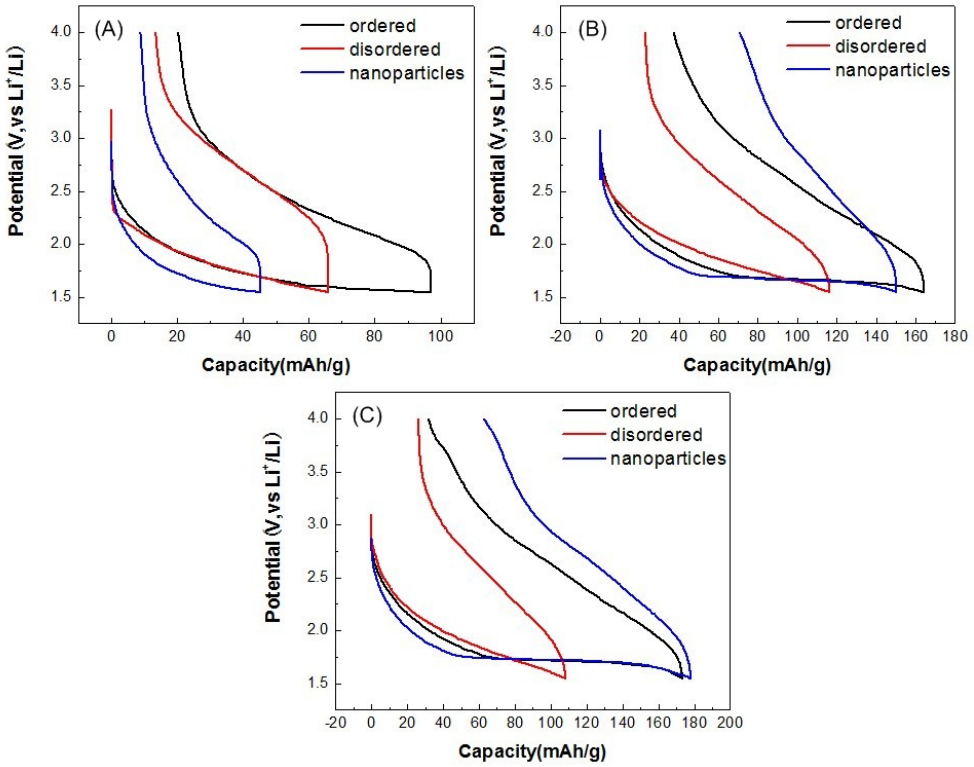

Figure 7.9: Variation of potential with state-of-charge (Li content) for the first discharge then charge for a composite electrode composed of different Fe_2O_3 with Super S carbon and Kynar, weight ratios 80 : 10 : 10, at different rate of (A) 1000 mAg^{-1} ; (B) 100 mAg^{-1} and (C) 33.5 mAg^{-1} .

Fe_2O_3 in this work is half of what was reported by Tarascon et al. [2,10]. The large difference in the cycling rate between these two experiments may be the reason for this difference. Therefore, it is interesting to investigate the rate capability of the three samples corresponding to the intermediate down to 1.55 V. Figure 7.9 presents the load curves at three different current densities: (A) 1000 mAg^{-1} ; (B) 100 mAg^{-1} and (C) 33.5 mAg^{-1} . For all three materials the capacity increased as the rate decreased. In the case of 1000 mAg^{-1} , the plateau at high voltage (1.75 V) observed at lower rates was not observed. This suggests that at high rate the insertion proceeds as a solid solution, perhaps because the kinetics of nucleation and growth of the second phase is too slow to occur at the high rate leading to a metastable structure. The nanoparticles exhibit the greatest loss in

capacity with increasing rate, indicating the inferior rate capability for the nanoparticulate sample as compared to the mesoporous phases.

The mesoporous material is composed of micrometer-sized particles containing ordered arrays of 4 nm diameter pores separated by 7 nm thick walls.[12] The electrolyte can flood the pores, ensuring a high area of contact between electrolyte and electrode. It facilitates lithium transport to the walls, within which the conversion reaction occurs. The width of the wall of the mesoporous samples is 7 nm compared with a particle size of 20 nm for the nanoparticles. It is proposed that the short diffusion distances in the walls and higher surface area of the mesoporous samples are the origin of the better rate capability of the mesopores.

Both the mesoporous α-Fe_2O_3 with ordered and disordered walls have retained the ordered porous structure on cycling, Figure 7.10. Though the poor capacity retention on cycling, even at low rates (33.5 mAg^{-1}), is evident in Figure 7.11 for all three cases.

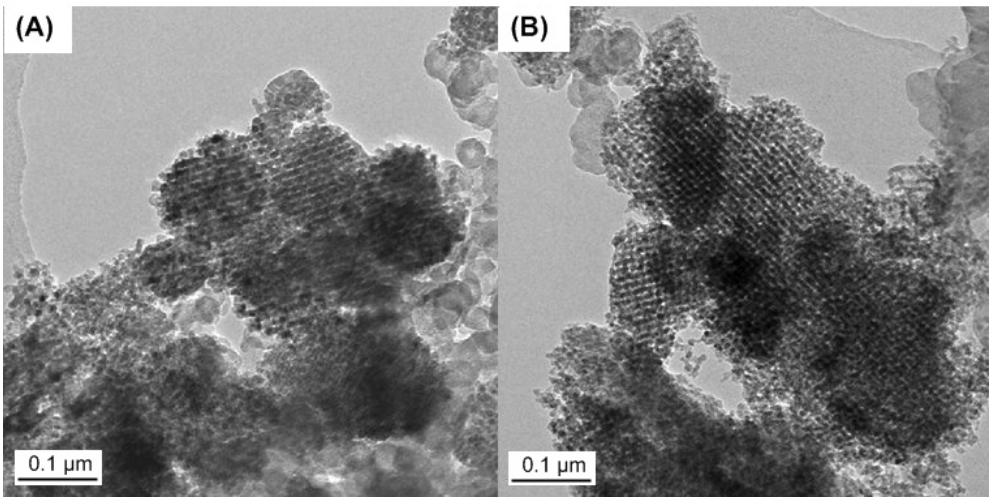

Figure 7.10: TEM images of the samples after 1st cycle between 1.55 and 4 V: (A) mesoporous α-Fe_2O_3 with ordered walls and (B) mesoporous α-Fe_2O_3 with disordered walls.

Tarascon claims that α-Fe_2O_3 in nanosize has much better electrochemical property than the bulk one (μm size) due to the smaller particle size.[2,10] The mesoporous α-Fe_2O_3 , which is composed of micrometer-sized particles

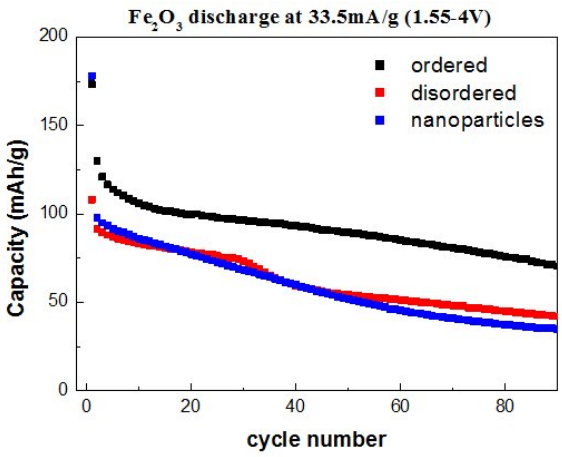

Figure 7.11: Variation of discharge capacity with cycle number at 33.5 mAg^{-1} between 1.55 and 4 V, different Fe_2O_3 electrode. Rates per gram of active material.

containing nanometer-sized mesoporous walls shows similar electrochemical properties as the nanoparticulate α-Fe_2O_3 . This indicates that the diffusion distance affects the electrochemical property more than the surface area.

7.4 Conclusions

The electrochemical properties of mesoporous α-Fe_2O_3 with ordered walls, mesoporous α-Fe_2O_3 with disordered walls, and Fe_2O_3 nanoparticles were studied. Mesoporous α-Fe_2O_3 with ordered walls and nanoparticulate α-Fe_2O_3 showed similar electrochemical properties. After Li insertion, a phase transformation from hcp to ccp happened, while there was no such reaction found in the reaction process for mesoporous α-Fe_2O_3 with disordered walls. The number of inserted lithium ions is determined by the specific surface area of the sample. Among all three samples, the nanoparticulate one presents the worst rate capability even though they all show poor rate capability and poor capacity retention on cycling. Therefore, it is believed that both surface area and particle size can affect the electrochemical property of the materials.

References

[1] Poizot, P., Laruelle, S., Grugeon, S., Dupont, L., and Tarascon, J. M. *Nature* **407**, 496 (2000).

[2] Larcher, D., Masquelier, C., Bonnin, D., Chabre, Y., Masson, V., Leriche, J. B., and Tarascon, J. M. *J. Electrochem. Soc.* **150**, A133 (2003).

[3] Xu, J. J. and Jain, G. *Electrochem. Solid State Lett.* **6**, A190 (2003).

[4] Tartaj, P., Gonzalez-Carreno, T., and Serna, C. J. *Adv. Mater.* **16**, 529 (2004).

[5] Cheon, J. W., Kang, N. J., Lee, S. M., Lee, J. H., Yoon, J. H., and Oh, S. J. *J. Am. Chem. Soc.* **126**, 1950 (2004).

[6] Jin, B., Ohkoshi, S., and Hashimoto, K. *Adv. Mater.* **16**, 48 (2004).

[7] Sun, S. H., Zeng, H., Robinson, D. B., Raoux, S., Rice, P. M., Wang, S. X., and Li, G. X. *J. Am. Chem. Soc.* **126**, 273 (2004).

[8] Guo, Q. J., Teng, X. W., Rahman, S., and Yang, H. *J. Am. Chem. Soc.* **125**, 630 (2003).

[9] Bourlinos, A. B., Bakandritsos, A., Georgakilas, V., and Petridis, D. *Chem. Mater.* **14**, 3226 (2002).

[10] Larcher, D., Bonnin, D., Cortes, R., Rivals, I., Personnaz, L., and Tarascon, J. M. *J. Electrochem. Soc.* **150**, A1643 (2003).

[11] Arico, A. S., Bruce, P., Scrosati, B., Tarascon, J. M., and Schalkwijk, W. V. *Nat. Mater.* **4**, 366 (2005).

[12] Jiao, F., Harrison, A., Jumas, J.-C., Chadwick, A. V., Kockelmann, W., and Bruce, P. G. *J. Am. Chem. Soc.* **128**, 5468 (2006).

[13] Dedryvere, R., Laruelle, S., Grugeon, S., Gireaud, L., Tarascon, J. M., and Gonbeau, D. *J. Electrochem. Soc.* **152**(4), A689 (2005).

[14] Laruelle, S., Grugeon, S., Poizot, P., Dolle, M., Dupont, L., and Tarascon, J. M. *J. Electrochem. Soc.* **149**(5), A627 (2002).

[15] Maier, J. *Nat. Mater.* **4**, 805 (2005).

[16] Morimoto, H., Tobishima, S., and Iizuka, Y. *J. Power Sources* **146**, 315 (2005).

[17] Thackeray, M. M., David, W. I. F., and Goodenough, J. B. *Mater. Res. Bull.* **17**, 785 (1982).

Chapter 8

Factors Influencing the Rate of Fe_2O_3 Conversion Reaction

8.1 Introduction

Conversion reactions, such as the reaction $2Li + CoO \leftrightarrow Li_2O + Co$, involve the formation of a nanocomposite in which nanoparticles of the transition metal (in this case Co) are embedded in a matrix of Li_2O . On extraction of lithium, the $Li_2O$is decomposed, and Co oxidised. These conversion reactions are receiving attention because of their ability to store significantly more charge (lithium) than graphite, used presently as the anode in rechargeable lithium batteries (1000 $mAhg^{-1}$compared with 370 $mAhg^{-1}$for graphite).[1–7] However, such conversion electrode reactions suffer from a number of problems, such as higher potentials and hence a lower cell voltage unless coupled with a higher voltage electrode, hysteresis between charge and discharge potentials, irreversible capacity loss on the first cycle and, perhaps of greatest importance, poor rate and poor capacity retention on cycling (charge stored decreases with increasing rate and cycle number).[7,8]

Limitations in the rate of conversion reactions can arise from several factors, poor Li^+ or e^- transport to the particles or through the particles to the reaction sites, as well as slow nucleation and growth of the new phases

formed. Poor capacity retention may arise from a reduction in the efficiency of one or more of these processes on cycling. The usual approach to increasing the rate of an electrode reaction is to form nanoparticles. However, in the case of conversion reactions, previous studies have demonstrated that this leads to a drastic fade in the capacity on cycling.[5,8] In an attempt to address the key problem of rate, Taberna et al. improved both the Li^+ and e^- transport processes by growing a thin ($\sim$ 100 nm) Fe_3O_4 film on a nanostructured current collector composed of Cu nano-pillars.[9] Every particle of Fe_3O_4 is in simultaneous contact with a source of e^- (current collector) and Li^+ (electrolyte).[9] Although this nano-architecture increases the rate of the Fe_3O_4 conversion reaction, fabricating such electrodes may be difficult in some cases and higher rates may be obtained at the expense of the charge stored per unit area, because of the low mass per unit area (0.26 $mAh \cdot (cm)^{-2}$ at 2.9 $mAh \cdot (cm)^{-2}$).

Achieving a high capacity per unit area at a high current per unit area (current density) and with high capacity retention on cycling, remains a challenge for conversion reactions but is essential for their use in batteries. The goal of this work is to better understand which factors limit the rate and capacity retention of conversion reactions and thus improve the capacity and its retention at high rates. Here the bulk, nanoparticulate, and mesoporous Fe_2O_3 were employed to examine the different factors that influence the rate of conversion electrodes, i.e., Li^+ and e^- transport to and within the particles, as well as the rate of the two-phase reaction, demonstrating that for this conversion reaction electron transport to and within the particles is paramount.[10]

8.2 Experimental

Bulk α-Fe_2O_3 powder ($\sim$ 5 μm, $>$ 99 %) was purchased from Sigma-Aldrich. Nanoparticulate α-Fe_2O_3 ($\sim$ 25 nm) was synthesised using a procedure reported previously (see 2.1.3).[11,12] Mesoporous α-Fe_2O_3 with ordered wall was synthesised using a procedure reported previously (see 2.1.2).[13]

Electrochemical cells were constructed by mixing the active material, Kynar 2801 (a co-polymer based on polyvinylidene fluoride), and Super S carbon (MMM) in various weight ratios. The mixture was cast onto glass from acetone using a Doctor-Blade technique. After solvent evaporation at room temperature and heating at 80 °C under vacuum for 8 hours, the foil was cut into 13 mm diameter disks. The electrodes were assembled into Swagelok cells with a Li electrode and LP 30 electrolyte (Merck; 1M $LiPF_6$ in 1 : 1 v/v ethylene carbonate : dimethyl carbonate). The typical mass of active material on each cell was $\sim$ 11 mg. The cells were constructed and handled in an Ar-filled MBraun glovebox. Electrochemical measurements were carried out using a MACCOR 4200 system.

8.3 Results and Discussion

Cells containing electrodes composed of α-Fe_2O_3 particles with an average diameter of 5 μm, combined with Super S carbon and Kynar as the binder, in the weight ratios 80 : 10 : 10 were constructed as described in the Experimental section and cycled galvanostatically. The variation of voltage with state of charge (lithium content) is shown in Figure 8.1A and is similar to that reported previously for the conversion reaction of micron sized α-Fe_2O_3 particles.[5,11] The first discharge capacity of 1080 $mAhg^{-1}$ is slightly higher than the theoretical value of 1006 $mAhg^{-1}$ ($6Li + Fe_2O_3 \rightarrow 2Fe + 3Li_2O$). Such excess capacity has been associated previously with a polymeric layer that forms on the electrode surface and/ or, in the important work of Maier, with charge storage due to space charge effects.[5,11,14?] The poor rate capability and poor capacity retention on cycling a composite electrode with μm α-Fe_2O_3 and 10 wt % carbon, even at low rates (100 $mAhg^{-1}$), is evident in Figure 8.1B.

In order to explore the role of electron transport to the α-Fe_2O_3 particles in controlling the rate of the electrode reaction and the capacity retention on cycling, the same α-Fe_2O_3 particles of micron dimensions were mixed with the same Super S and Kynar but in three different weight ratios; the mass of

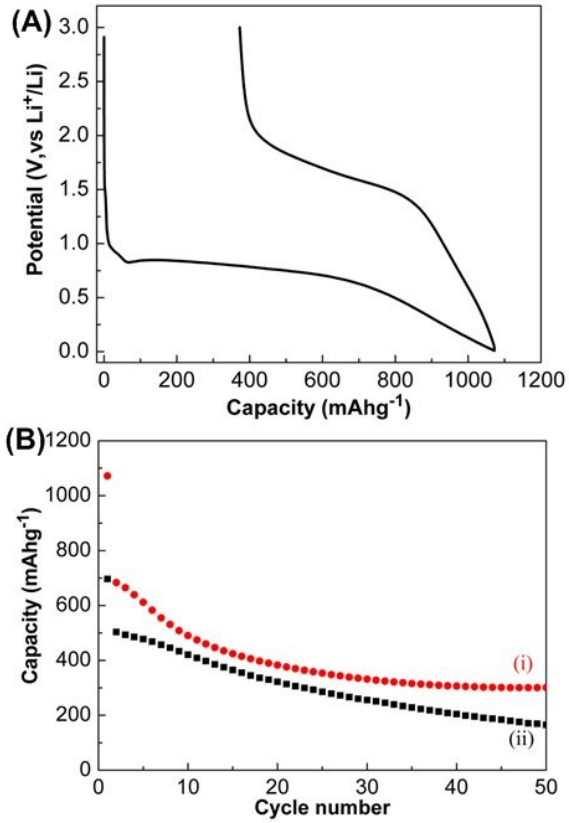

Figure 8.1: (A) Variation of potential with state-of-charge (Li content) for the first discharge then charge for a composite electrode composed of micron-sized α-Fe_2O_3 with super S carbon and Kynar, weight ratios 80 : 10 : 10, at a rate of 100 mAg^{-1}. (B) Variation of discharge capacity with cycle number at (i) 100 mAg^{-1} and (ii) 1000 mAg^{-1} , same electrode as in (A). Rates per gram of active material.

α-Fe_2O_3 per unit electrode area was maintained constant throughout this and all other experiments at 8 $mg \cdot cm^{-2}$. The resulting variation of capacity with cycle number is shown in Figure 8.2. Increasing the proportion of carbon around the electroactive particles improves the rate capability (increased capacity) and the capacity retention on cycling. There is little or no benefit from increasing the carbon content above $\sim$ 30 wt %, probably because the percolation limit has already been exceeded.

To explore the role of Li^+ transport to the α-Fe_2O_3 surface and within the α-Fe_2O_3 particles (i.e. mass transport), the electrochemical behaviour of mesoporous α-Fe_2O_3 was investigated. This material is composed of micron

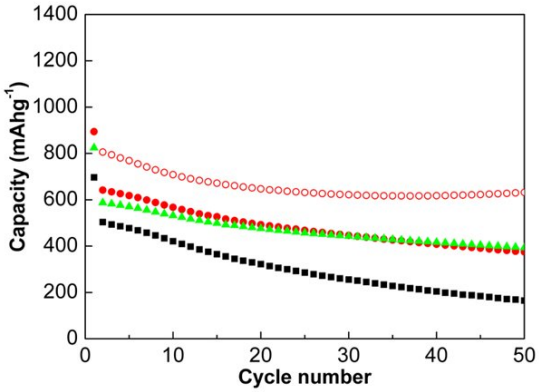

Figure 8.2: Variation of discharge capacity with cycle number for micron-sized α-Fe_2O_3 particles combined with Super S carbon and Kynar in the 3 different weight ratios (black 80 : 10 : 10, red 60 : 30 : 10, green 50 : 40 : 10) at a rate of 1000 mAg^{-1}, between 0.01-3.00 V vs Li^+/Li. Red open symbols show the cycleability of nano-Fe_2O_3 composite (60 : 30 : 10) at a rate of 100 mAg^{-1} . Rates per gram of active material.

sized particles containing ordered arrays of 4 nm diameter pores separated by 7 nm thick walls, the latter composed of highly crystalline α-Fe_2O_3 , Figure 8.3A and 8.3B.[13] The electrolyte can flood the pores, ensuring a high area of contact between electrolyte and electrode (surface area $\sim 130\ m^2g^{-1}$) and hence facile lithium transport to the walls of the α-Fe_2O_3 material, within which the conversion reaction occurs. Because the walls are of nanometre dimensions, lithium transport within them should be more facile than for the dense micron-sized particles, discussed above. In addition, the nanometer walls should reduce the strain associated with the conversion reaction. The ability of mesoporous materials to accommodate the strain of solid/ solid transformations has been demonstrated by converting mesoporous α-Fe_2O_3 (corundum structure, hexagonal close-packed (hcp) O^{2-} stacking) to the spinel Fe_3O_4 (cubic close-packed (ccp) O^{2-} stacking) without destroying the mesostructure.[15]

The results for mesoporous α-Fe_2O_3 / Super S/ Kynar electrodes, with weight ratios 80 : 10 : 10 are shown in Figure 8.3C. The initial capacities are higher than for the micron-sized particles, and higher than the theoretical capacity for α-Fe_2O_3 . This effect has been noted previously for high surface area conversion reactions and associated with polymer surface layer formation

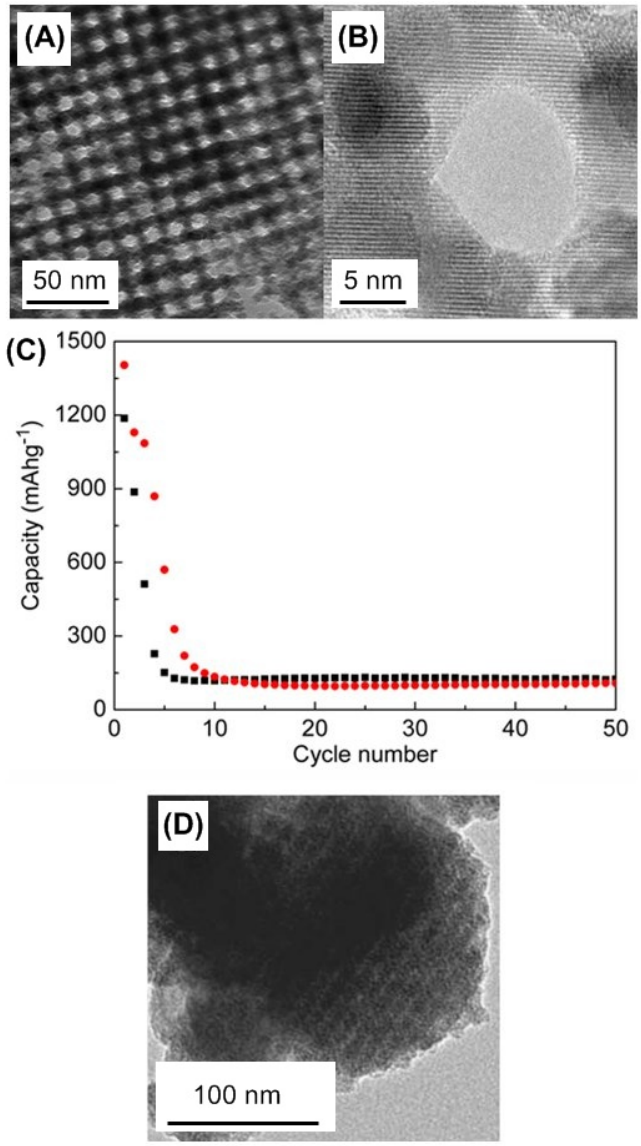

Figure 8.3: (A) TEM and (B) HRTEM images of mesoporous α-Fe_2O_3 with a highly ordered pore structure and highly crystalline walls. (C) Variation of discharge capacity with cycle number at low (red, 100 mAg^{-1}) and high (black, 1000 mAg^{-1}) rates for mesoporous α-Fe_2O_3 (micron sized particles containing 4 nm diameter pores and 7 nm thick walls). The electrode was a composite of mesoporous Fe_2O_3 , Super S and binder in the weight ratios 80 : 10 : 10. Voltage range: 0.01-3.00 V vs Li^+/Li. Rates per gram of active material. (D) TEM image of mesoporous α-Fe_2O_3 after 20 cycles.

and/ or charge storage via surface charge-transfer mechanisms.[11] The large reduction in capacity on increasing the rate, for any given cycle number during the first few cycles, clearly demonstrates the poor rate capability of the mesoporous material. Although the mesostructure was maintained after cycling, Figure 8.3D, the capacity retention on cycling is very poor. We may conclude that promoting facile Li^+ transport to the electrode surface and within the electrode, as well as aiding the two-phase conversion reaction due to the nanometer dimensions of the walls, does not, in itself, lead to high rate capability or good capacity retention. Although the walls are only several nanometers thick, the mesoporous particles are of micrometer dimension, hence the e^- transport is not enhanced, suggesting this is a critical factor controlling rate.

To investigate the role of e^- transport within the particles, nanoparticles of α-Fe_2O_3 were synthesised (see Section 2.1.3). The average particle size was 25 nm, Figure 8.4A and 8.4B. The variation of capacity with cycle number for a composite electrode containing nano-Fe_2O_3 , super S and Kynar in the weight ratios 60 : 30 : 10 is shown in Figure 8.5A. Carbon (30 wt %) was chosen to ensure good e^- transport to the particles. The initial capacity is higher than the bulk because of the higher surface area. The capacity retention on cycling is excellent, Figure 8.5A; indeed the capacity increases slightly, something that has also been noted previously for conversion reactions.[9] The rate capability is also excellent, Figure 8.5B, with capacities of 700 $mAhg^{-1}$ being delivered at a rate of 3000 mAg^{-1}. Even correcting for the additional 20 wt % carbon (typically 10 wt % carbon is used in composite electrodes) a capacity of 560 $mAhg^{-1}$ is obtained at this rate.

Comparing nano, mesoporous and micron α-Fe_2O_3 , the first two enhance Li^+ transport to (high surface area) and within the particles/ walls, as well as easing the strain of the conversion reaction, however mesoporous α-Fe_2O_3 does not enhance e^- transport (μm particle size) demonstrating the importance of e^- transport within the particles in achieving high rates. Note that Balaya et al. have shown that for conversion reactions involving metal

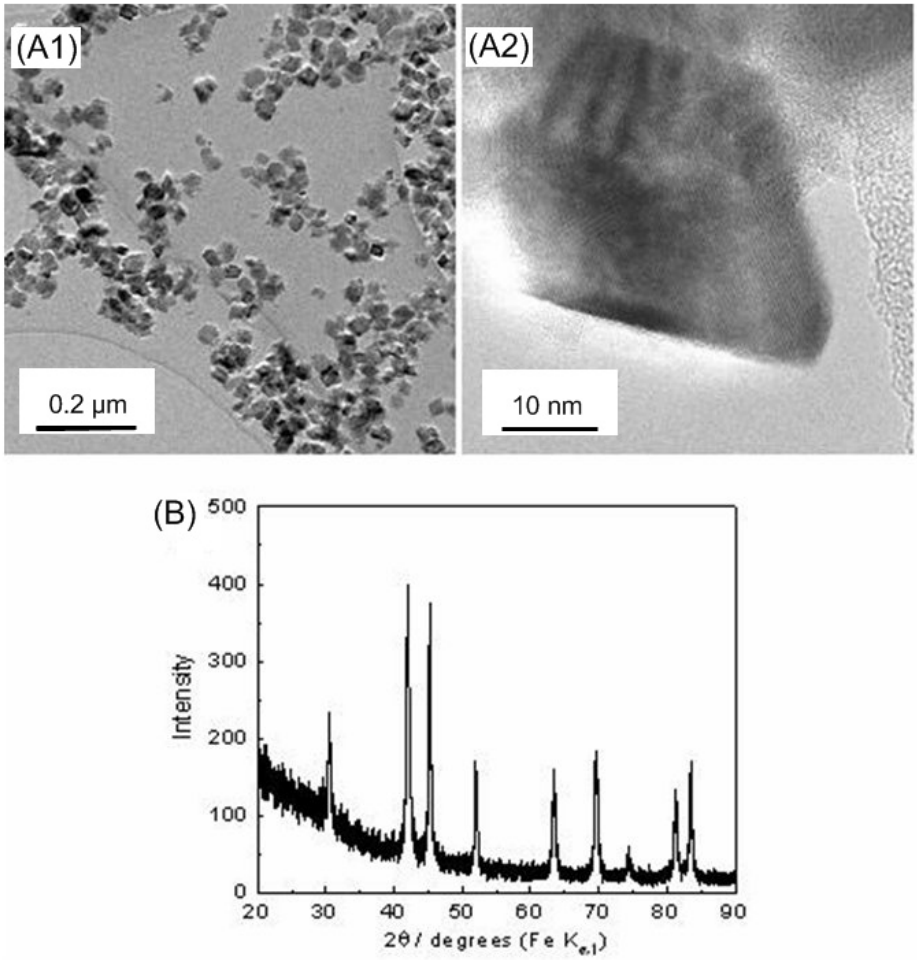

Figure 8.4: (A)TEM images of nano-Fe_2O_3 particles. (B)PXRD pattern for nanoparticulate Fe_2O_3 .

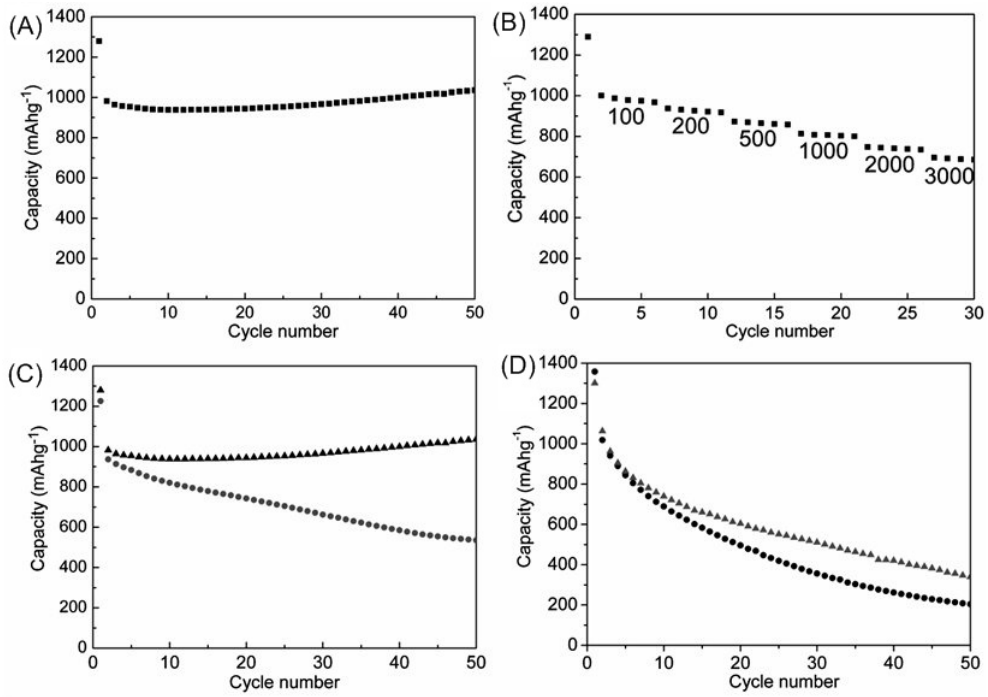

Figure 8.5: (A) Variation of discharge capacity with cycle number at 100 mAg^{-1} for composite electrodes formed between nano-Fe_2O_3 , Super S carbon and Kynar in the weight ratios 60 : 30 : 10. (B) Composite electrode formed between nano-Fe_2O_3 , super S carbon and Kynar in the weight ratios 60 : 30 : 10 cycled at 100, 200, 500, 1000, 2000, and 3000 mAg^{-1} . (C) Influence of changing the carbon content on the capacity (triangle 30 wt % carbon, circle 20 wt % carbon) and its retention on cycling for nanoparticulate α-Fe_2O_3 electrodes. Rate: 100 mAg^{-1} . (D) Influence of changing the binder content on the capacity retention on cycling nanoparticulate Fe_2O_3 electrodes. Rate: 100 mAg^{-1} ; nano-Fe_2O_3 , super S carbon and Kynar in the weight ratios 60 : 10 : 30 (triangle) and 70 : 10 : 20 (circle). All cells were cycled between 0.01-3.00 V vs Li^+/Li. Rates per gram of active material.

oxides that are good electronic conductors (specifically RuO_2) the irreversible capacity on the first cycle can be reduced significantly. [2,7] Fe_2O_3 is a poor e^- conductor.

Some previous reports of nanoparticulate conversion electrodes demonstrated poor performance,[5,8] reinforcing the fact that it is essential to combine nanoparticles with sufficient carbon to ensure high performance. Carbon loaded α-Fe_2O_3 nanoparticles have been shown to improve the performance.[16] Figure 8.5C indicates that carbon contents below 30 % are insufficient to obtain good rates. It has been suggested previously that carbon in composite electrodes may act as a mechanical buffer as well as a conducting medium. The data in Figure 8.5D show that increasing the proportion of binder does not result in the same improvement as increasing the carbon content, demonstrating that the primary role of carbon is to improve electron transport within the composite electrode.

8.4 Conclusions

In conclusion, factors influencing the rate and capacity retention of conversion electrodes have been investigated using α-Fe_2O_3 . Although it is difficult to separate entirely the different contributions, the results show that electron transport to and within the particles are the main factors limiting the rate. A simple electrode, consisting of a composite of α-Fe_2O_3 (rust) nanoparticles ($\sim$ 25 nm), Super S carbon and Kynar (60 : 30 : 10), is capable of delivering a capacity of 1000 $mAhg^{-1}$ at a rate of 100 mAg^{-1} and with no overall fade after some 50 cycles. Even at high rates, 3000 mAg^{-1} , a capacity of 700 $mAhg^{-1}$ is obtained. Taking account of the excess carbon (20 %), the capacity is still 560 $mAhg^{-1}$ (4.8 $mAh \cdot (cm)^{-2}$). Because our electrodes are composites and not films, the mass of active material per unit electrode area is higher, resulting in higher capacities per unit area at high rates. Capacities of 6 $mAh \cdot (cm)^{-2}$ at current density of 26 $mA \cdot (cm)^{-2}$ are obtained. The composite α-Fe_2O_3 electrode is very easy to fabricate and, like other iron oxide electrodes, is cheap and of low toxicity.

8.5 Future Work

Future efforts need to be devoted to coating the α-Fe_2O_3 nanoparticles with carbon or other e^- conductors in order to preserve the electron transport while reducing the amount of carbon and hence electrode volume (increasing volumetric energy density). Depending on the application, film based nanostructured electrodes (reference 9) or nanocomposites may be employed to deliver conversion electrode reactions supporting high rate capability.

References

[1] Poizot, P., Laruelle, S., Grugeon, S., Dupont, L., and Tarascon, J. M. *Nature* **407**, 496 (2000).

[2] Balaya, P., Li, H., Kienle, L., and Maier, J. *Adv. Funct. Mater* **13**, 621 (2003).

[3] Souza, D. C. S., Pralong, V., Jacobson, A. J., and Nazar, L. F. **296**, 2012 (2002).

[4] Pereira, N., Klein, L. C., and Amatucci, G. G. *J. Electrochem. Soc* **149**, A262 (2002).

[5] Hosono, E., Fujihara, S., Honma, I., Ichihara, M., and Zhou, H. S. *J. Electrochem. Soc* **153**, A1273 (2006).

[6] Arico, A. S., Bruce, P., Scrosati, B., Tarascon, J. M., and Schalkwijk, W. V. *Nat. Mater* **4**, 366 (2005).

[7] Maier, J. *Nat. Mater* **4**, 805 (2005).

[8] Larcher, D., Sudant, G., Leriche, J. B., Chabre, Y., and Tarascon, J. M. *J. Electrochem. Soc* **149**, A234 (2002).

[9] Taberna, L., Mitra, S., Poizot, P., Simon, P., and Tarascon, J. M. *Nat. Mater* **5**, 56 (2006).

[10] Jiao, F., Bao, J. L., and Bruce, P. G. *Electrochem. Solid-State Lett* **10**, A264 (2007).

[11] Larcher, D., Bonnin, D., Cortes, R., Rivals, I., Personnaz, L., and Tarascon, J. M. *J. Electrochem. Soc* **150**, A1634 (2003).

[12] Larcher, D., Masquelier, C., Bonnin, D., Chabre, Y., Masson, V., and Leriche, J. B. *J. Electrochem. Soc* **150**, A133 (2003).

[13] Jiao, F., Jumas, J. C., Womes, M., Chadwick, A. V., Harrison, A., and Bruce, P. G. *J. Am. Chem. Soc* **4**, 336 (2005).

[14] Maier, J. *Faraday Discuss* **134**, 51 (2007).

[15] Jiao, F., Jumas, J. C., Womes, M., Chadwick, A. V., Harrison, A., and Bruce, P. G. *Nat. Mater* **4**, 336 (2005).

[16] Hang, B. T., Watanabe, I., Doi, T., Okada, S., and Yamaki, J. I. *J. Power Sources* **1281**, 161 (2006).

Chapter 9

Summary and Future Work

9.1 Summary

A new rechargeable Li/O_2 battery system was studied by replacing the intercalation electrode with a porous electrode and allowing lithium to react directly with O_2 from the air. The porous cathode is comprised of carbon, catalyst and binder. The effect of every component was investigated.

The catalyst is found to be the most important component in Li/O_2battery. EMD, Fe_3O_4 , CuO, $CoFe_2O_4$, NiO, Co_3O_4 , α-MnO_2 , β-MnO_2 , γ-MnO_2 , λ-MnO_2 , Mn_2O_3 and Mn_3O_4 show their potential to be used as the catalyst of the O_2electrode in a non-aqueous Li/O_2cell. α-MnO_2 nanowires were found to be the best candidate. The reversible capacities of 3000 $mAhg^{-1}$(normalised by the mass of carbon) or 505 $mAhg^{-1}$ (based on the total mass of cathode + O_2) were obtained. It suggests that the nature of the catalyst is a key factor controlling the performance of the O_2 electrode. CuO, NiO, Co_3O_4 and Mn_3O_4 each with three different morphologies, bulk, nanoparticulate and mesoporous were studied. Charging potentials can be reduced from around 4.5 V to 3.79 V versus Li^+/Li by increasing the surface area. Performance of cycling is enhanced by an increase in the surface area and capacity retention is better for the mesoporous morphologies and simple nanoparticles in most cases.

Some of other factors, such as type of carbon, type of binder, type of electrolyte, the construction of cathode and the modification of the catalyst were also investigated. Carbon with higher surface area apparently could give more initial capacity, by utilising the nanosized catalyst it also showed good capacity retention. By attempting to minimise the proportion of catalyst and binder, more specific capacity based on total electrode mass was obtained. Combined with loading the catalyst onto the carbon, 2500 $mAhg^{-1}$ based on the total mass of cathode can be obtained. Capacity fading during cycling is the main problem in all the cases. Besides the formation of Li_2O_2 filling the pores of the cathode, the solvent for the electrolyte, PC, was found decomposed on both anode and cathode, which is believed to be one of most important reasons causing the capacity fading.

The electrochemical properties of mesoporous α-Fe_2O_3 with ordered walls, mesoporous α-Fe_2O_3 with disordered walls, and Fe_2O_3 nanoparticles were studied. Mesoporous α-Fe_2O_3 with ordered walls and nanoparticulate α-Fe_2O_3 showed similar electrochemical properties. After Li insertion, a phase transformation from hcp to ccp happened, while there was no such reaction found in the reaction process for mesoporous α-Fe_2O_3 with disordered walls. The number of inserted lithium ions is determined by the specific surface area of the sample. Among all three samples, the nanoparticulate one presents the worst rate capability even though they all show poor rate capability and poor capacity retention on cycling.

Factors influencing the rate and capacity retention of conversion electrodes have been investigated using α-Fe_2O_3 . The results show that electron transport to and within the particles are the main factors limiting the rate. A simple electrode, consisting of a composite of α-Fe_2O_3 (rust) nanoparticles ($\sim$ 25 nm), Super S carbon and Kynar (60 : 30 : 10), is capable of delivering a capacity of 1000 $mAhg^{-1}$ at a rate of 100 mAg^{-1} and with no overall fade after some 50 cycles. Even at high rates, 3000 mAg^{-1}, a capacity of 700 $mAhg^{-1}$ is obtained.

9.2 Future Work

To better understand how the new Li/O_2 battery system works, more fundamental experiments should be done to address the electrochemical reactions happening in the system during cycling. More effort is also needed to further improve the performance of the Li/O_2 battery, such as optimising the porosity, structure and composition of the electrode, reducing the hysteresis between the charge and discharge potentials, increasing the efficiency on cycling and seeking for the new electrolyte to avoid the decomposition. It is also desired to develop a method to avoid the H_2O or CO_2 ingress to achieve operation in air eventually.

Publication List

[1] "α-MnO_2 nanowires: a catalyst for the O_2 electrode in rechargeable lithium batteries,"
A. Débart, A. J. Paterson, J. L. Bao, and P. G. Bruce, *Angew. Chem. Int. Ed.*, vol. 47, p. 4521, 2008.

[2] "Factors influencing the rate of the Fe_2O_3 conversion reaction,"
F. Jiao, J. L. Bao, and P. G. Bruce, *Electrochem. Solid-State Lett*, vol. 10, p. A264, 2007.

[3] "An O_2 cathode for rechargeable lithium batteries: the effect of a catalyst,"
A. Débart, J. L. Bao, G. Armstrong, and P. G. Bruce, *J. Power Sources*, vol. 174, p. 1177, 2007.

[4] "Effect of catalyst on the performance of rechargeable lithium/ air batteries,"
A. Débart, J. L. Bao, G. Armstrong, and P. G. Bruce, in *ECS Transactions–Cancun, "Lithium Ion Batteries: Materials and Devices"*, vol. 3, 2007.